Review of the Influence of the Interaction Between In-Plane and Out-of-Plane Behaviors on the Seismic Response of Non-Framed Unreinforced Masonry Walls

Ghezelbash, Amirhossein; Rots, Jan G.; Messali, Francesco

DOI
10.3390/buildings15162874

Publication date
2025

Document Version
Final published version

Published in
Buildings

Citation (APA)
Ghezelbash, A., Rots, J. G., & Messali, F. (2025). Review of the Influence of the Interaction Between In-Plane and Out-of-Plane Behaviors on the Seismic Response of Non-Framed Unreinforced Masonry Walls. *Buildings*, *15*(16), Article 2874. https://doi.org/10.3390/buildings15162874

buildings

MDPI

Review

Review of the Influence of the Interaction Between In-Plane and Out-of-Plane Behaviors on the Seismic Response of Non-Framed Unreinforced Masonry Walls

Amirhossein Ghezelbash *, Jan G. Rots and Francesco Messali

Faculty of Civil Engineering and Geosciences, Delft University of Technology, 2628 CN Delft, The Netherlands; j.g.rots@tudelft.nl (J.G.R.); f.messali@tudelft.nl (F.M.)
* Correspondence: a.ghezelbash@tudelft.nl

Abstract

This study reviews existing research on the effects of the interaction between in-plane (IP) and out-of-plane (OOP) behaviors on the seismic response of non-framed unreinforced masonry (URM) structures. During earthquakes, masonry buildings exhibit complex behaviors. First, walls may experience simultaneous IP and OOP actions, or pre-existing IP and OOP damage, deformation, or loads that can alter their unidirectional IP or OOP seismic response. Second, the IP and OOP action of one wall can affect the behavior of its intersecting walls. However, the effects of these behaviors, referred to as "direct IP-OOP interactions" and "Flange effects", respectively, are often disregarded in design and assessment provisions. To address this gap, this study explores findings from experimental and numerical research conducted at the wall level currently available in the literature, identifying the nature of these interaction effects and the key parameters that affect their extent. The available body of work includes only a few experimental studies on interaction effects, whereas numerical investigations are more extensive. However, most numerical studies focus on how OOP pre-damage/deformation influences the IP behaviors (OOP/IP interactions) and the role of flanges in IP response (F/IP interactions), leaving significant gaps in understanding the effects of IP pre-damage/deformation on the OOP response (IP/OOP interactions) and the OOP response in the presence of flanges (F/OOP interactions). Among the parameters studied, boundary conditions, wall height-to-length aspect ratio, and vertical overburden are found to have the most significant influence on interaction effects because of their relevance for the IP and OOP failure mechanisms. Other parameters, such as the restriction of top uplift, the presence of openings, or changes in slenderness ratio, are not comprehensively studied, and the available data are insufficient for definitive conclusions. Methodologies available in the literature for extrapolating the findings observed at the wall level to building-level analyses are reviewed. The current predictive equations primarily address the effects of OOP pre-load and Flange effects on IP response. Furthermore, only a few macro-element models are proposed for cost-effective, large-scale building simulations. To bridge these gaps, future research must expand experimental investigations, develop more comprehensive design and assessment equations, and refine numerical modeling techniques for building-level applications.

Keywords: unreinforced masonry; interaction; in-plane; out-of-plane; flange effect; earthquake loading; non-framed walls

Academic Editor: Changjiang Liu

Received: 14 July 2025
Revised: 6 August 2025
Accepted: 11 August 2025
Published: 14 August 2025

Citation: Ghezelbash, A.; Rots, J.G.; Messali, F. Review of the Influence of the Interaction Between In-Plane and Out-of-Plane Behaviors on the Seismic Response of Non-Framed Unreinforced Masonry Walls. *Buildings* **2025**, *15*, 2874. https://doi.org/10.3390/buildings15162874

1. Introduction

Unreinforced masonry (URM) structures are widely used worldwide due to their ease of construction, affordability, sound and thermal insulation, and low maintenance requirements [1]. Despite their satisfactory performance under gravity load, URM buildings are notably vulnerable to lateral forces, such as those induced by earthquakes [2–6]. For instance, the recent earthquake on 6 February 2023 in Kahramanmaraş (Türkiye) [7,8] caused severe damage to URM structures, rendering approximately 31% of the building stock unusable due to widespread failures at wall corners, separation from perpendicular walls, and excessive cracking. Despite such vulnerability to earthquakes, URM structures remain prevalent even in highly seismic regions [9], underscoring the need for a comprehensive understanding of their seismic response to develop reliable design and assessment methodologies.

Given the complexities involved in studying the seismic response of entire buildings experimentally or numerically [10], many investigations focus on individual wall-scale behaviors, often under simplified loading and geometric assumptions [11,12]. A key challenge in predicting the seismic performance of non-framed URM structures (i.e., of walls that are not supported or restrained by a surrounding structural frame, such as reinforced concrete or steel beams and columns) arises from the interaction between in-plane (IP) and out-of-plane (OOP) responses in different walls [13]. In this realm, experimental and numerical studies remain limited. Although real earthquakes subject walls to a combination of IP and OOP deformation [14], most research isolates these effects, investigating either exclusive IP [15–21] or exclusive OOP [11,22–37] loading. Furthermore, while intersecting walls influence the IP and OOP performance of each other [38,39], studies typically analyze isolated non-flanged walls, disregarding their interaction with adjacent structural components [40]. These simplifications create a critical knowledge gap in understanding how such interactions impact both wall-level and overall building responses, limiting the accuracy of design and predictive models [41–45]. Notably, although well-established classifications and predictive equations for damage in URM walls under IP and OOP loading exist, examples of which can be found in [46–48], they do not fully consider the complexity of real-world seismic responses such as failure due to weak connections with perpendicular walls and cracking caused by the combined IP and OOP actions.

The effects of combined IP and OOP actions, as well as the presence of flanges on the response of URM walls, have gained relevance as the poor performance of URM buildings during recent earthquake events [49–51] has raised significant concerns regarding their safety. It is also highly relevant for regions such as the Groningen province in the Netherlands, wherein induced earthquakes occur frequently (several dozens per year [52]) from different local epicenters, causing light structural damage. The accumulation of such damage from previous seismic events has raised concerns about its impact on structural performance. Specifically, typical Dutch URM buildings are regular non-framed constructions made with slender walls. Since these buildings have not been designed to withstand seismic events, the OOP performance of their walls under different levels of pre-existing IP damage has become a topic of investigation in recent years.

To highlight current knowledge gaps and identify promising directions for future research, this paper presents a comprehensive review of studies on the interaction between IP and OOP behaviors and their influence on the seismic response of non-framed URM walls. In addition to synthesizing existing research, this paper proposes a consistent terminology for IP and OOP interaction effects, addressing the lack of standardization and enabling clearer comparison and communication across studies. The manuscript is structured as follows. Section 2 defines the wall-level IP and OOP interaction mechanisms considered within the scope of the study, followed by a review of all relevant publications

in Section 3. The outcomes of all experimental and numerical studies examining interaction effects at the wall level are analyzed and cross-compared in Section 4, along with an analysis of how different wall properties influence these behaviors. Section 5 reviews current design and assessment guidelines and discusses studies that extend wall-level findings to full-building analyses. Section 6 outlines the identified knowledge gaps requiring further investigation. Finally, an overview of the conclusions drawn based on the current available knowledge, with recommendations for future research, is presented in Section 7.

2. Definition of "In-Plane and Out-of-Plane Interaction Effects" in Non-Framed URM Walls

Due to the scarcity of studies on the interaction between IP and OOP responses in non-framed URM walls, a consistent classification of such interactions and their different scenarios is currently missing in the literature. Hence, this study proposes a consistent definition of different types of interaction effects, introducing terminologies that capture the range of possible interaction scenarios, aiming to systematically categorize the existing body of research and set a benchmark for future work. Accordingly, two forms of IP and OOP interaction are considered. The first, termed "direct interaction", occurs at the level of individual walls, where existing IP load, deformation, or damage alters the OOP response of the wall, and existing OOP load, deformation, or damage alters its IP response [53]. The influence of IP response on OOP behavior is referred to as "IP/OOP interaction", while the reverse effect is termed "OOP/IP interaction". Collectively, these are designated as "direct IP-OOP interaction effects". The second, "indirect interaction", occurs at the structural level due to the presence of intersecting perpendicular walls, commonly referred to as "flanges" or "return elements". These flanges modify the IP and OOP behavior of the primary (or the main) wall [54], known as the "flanged wall". This influence is termed "Flange effects" to distinguish it from direct IP-OOP interactions. The effect of flanges on the IP and OOP behavior of the main panel is denoted as "F/IP interaction" and "F/OOP interaction", respectively.

As shown in Figure 1, direct IP-OOP interactions are investigated under four loading scenarios: sequential (SQ), successive (SC), combined (CB), and simultaneous (SM). SQ loading involves first applying and unloading the wall in either IP or OOP lateral direction to pre-damage the wall, before loading it in the orthogonal direction. SC loading also applies IP and OOP loads separately but alternates between them in multiple loading steps to capture cumulative damage effects. CB loading introduces a pre-load or pre-deformation in one direction, which is then held constant while a new load is applied in the perpendicular direction. Pre-load may result in deformations that change during subsequent loading, while pre-deformation alters the forces required to maintain them, leading to different structural responses compared to pre-loading. SM loading applies both IP and OOP loads concurrently, with varying intensity ratios, closely replicating real-world seismic conditions of structures experiencing multi-directional loading. Different loading sequences in each loading scenario are further distinguished, as illustrated in Figure 1. For SQ and CB loading scenarios, sequences that start in IP loading followed by OOP loading are labeled as "IP, OOP", while those beginning with OOP followed by IP loading are labeled as "OOP, IP". Similarly, for SC scenarios, "IP, OOP, IP" indicates sequences that start with IP loading, and "OOP, IP, OOP" denotes those that begin with OOP loading. Finally, simultaneous IP and OOP loading in the SM scenario is labeled as "IP + OOP".

Flange effects occur due to the interaction between intersecting walls, redistributing forces between the main wall and its flanges. This redistribution affects both IP and OOP responses, occurring under pure IP or OOP loading as well as all direct IP-OOP interaction loading scenarios mentioned above. Consequently, Flange effects not only

modify the unidirectional response of the primary wall and flanges [41] but also influence their behavior under direct IP-OOP interactions. Hence, some studies explore the latter in a combined interaction scenario referred to in this study as "F/IP-OOP interaction."

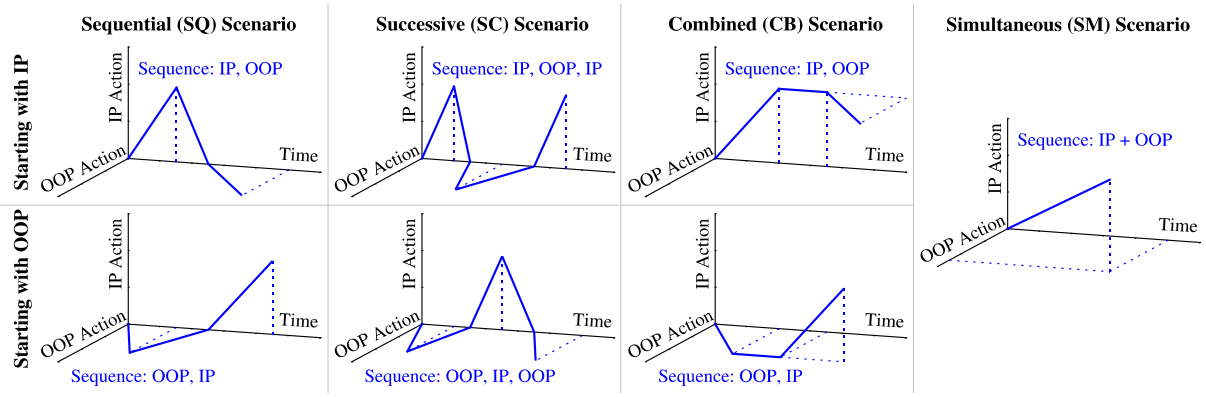

Figure 1. Examples of different loading sequences used in the study of direct IP-OOP interaction effects. For the meaning of abbreviations, please refer to the Nomenclature section.

3. Available Research on Interaction Effects in Non-Framed URM Walls

As of 2025, the number of research articles, conference contributions, and theses addressing direct IP-OOP interactions and Flange effects in non-framed URM walls remains limited. Figure 2 illustrates the growing, yet relatively recent interest in these interaction effects, with related publications emerging primarily over the past two decades. Specifically, direct IP-OOP interactions are examined in 25 studies [54–76], Flange effects in 21 [70,76–93], and F/IP-OOP interactions in only three [70,76,87]. These works are categorized by their methodology of studying interaction effects, with experimental studies conducted in 18 publications [54,56,68,71–75,77–86] and numerical simulations forming the basis of 27 publications [41,55–70,76,82,87–94]. Tables 1 and 2 detail the wall specimens studied experimentally and numerically for interaction effects, respectively. The tables include information on the type of interaction studied, mechanical and geometrical properties of the walls, loading assumptions, and boundary conditions. The number of specimens studied for each interaction type is also shown in Figure 2B. Some works, especially numerical ones [55–58,64,69,71,76,90,93], include additional specimens beyond those listed in the tables; however, due to the unavailability of relevant data, they cannot be utilized in interpreting interaction effects. Thus, only the specimens with a complete description are considered, and only their number is reported for each study. Hence, the two publications that do not present the results of their numerical simulations [41,58] are excluded from Figure 2B, Table 2, and the corresponding reviews. It should be noted that in the context of non-framed URM walls, the definition of aspect ratio can vary as different studies may consider it as the height-to-length dimension ratio or the length-to-height dimension ratio. This study uses the former definition across all the reviewed publications to maintain consistency in the collected data. It should be noted that the latter definition is more in line with the definition of aspect ratio used in the study of framed URM walls [94].

Experimental studies provide crucial insights into the seismic performance of masonry structures, capturing key parameters such as shear resistance, stiffness degradation, energy dissipation, and failure mechanisms under the influence of interaction effects. By applying lateral loads in controlled laboratory settings, these tests replicate earthquake-induced forces and help characterize the behavior of URM walls [95]. However, the high costs, complexity, and scalability limitations of physical testing significantly restrict the number of experiments that can be conducted, making it challenging to explore a wide range of influencing parameters [96]. Consequently, studies on direct IP-OOP interaction and

Flange effects in URM remain scarce, with only eight [54,56,68,71–75] and 11 [77–86] publications available on each topic, respectively. Among the 20 available direct IP-OOP interaction experiments, only eight [68,74] involve full-scale wall specimens, while the remaining 12 [56,71–73,75] focus on small-scale wallets due to the considerable challenges in designing and executing direct IP-OOP interaction tests. In contrast, Flange effect studies are conducted on 44 full-scale walls, as their experimental setups face fewer practical constraints.

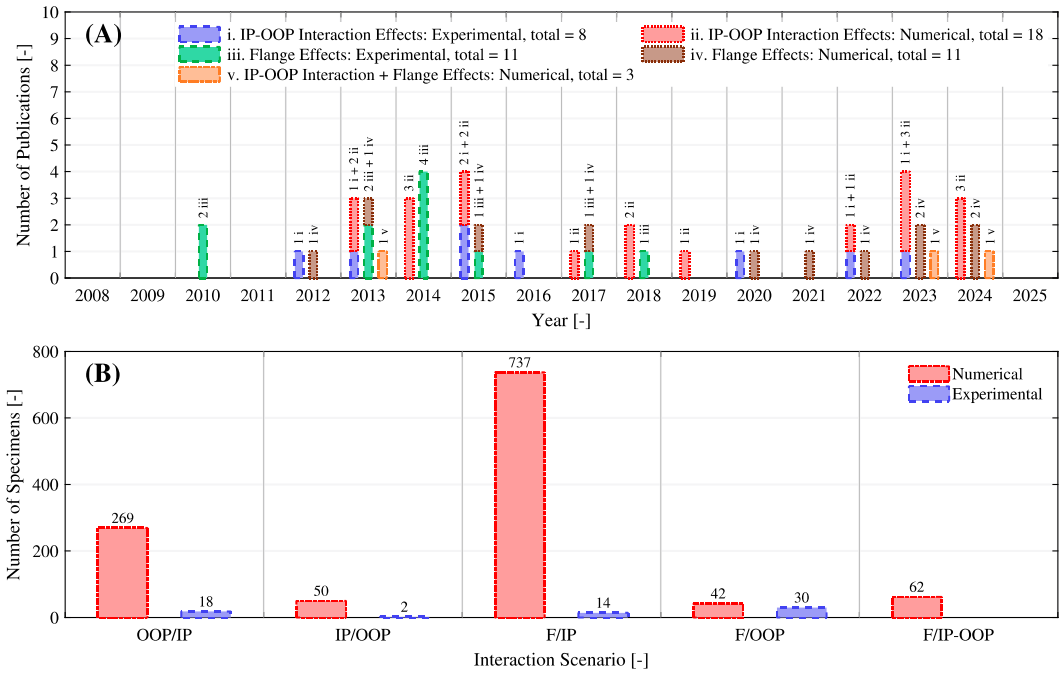

Figure 2. Overview of experimental and numerical studies focusing on non-framed unreinforced masonry walls under the effects of different interactions between IP and OOP behaviors: number of publications per year (**A**) and number of specimens (**B**). For the meaning of abbreviations, please refer to the Nomenclature section.

The experiments listed in Table 1 specifically focus on URM walls and the influence of different parameters on the extent to which different interaction effects occur. In other words, the reference non-flanged specimens under exclusive IP or OOP loading presented in the publications are excluded as they fall outside of the scope of the current review. Moreover, although several additional studies on flanged walls subjected to IP [97–101] or OOP [11,23,25,27,28,34,35,38,49,102–111] loading exist in the literature, they are excluded from the database for several reasons. First, some studies [11,23,27,49,102–105,112] use flanges purely as boundary elements to impose restrictions on the OOP response of the main panel rather than examining their structural influence. Second, other works investigate reinforced masonry walls [97], different strengthening techniques [35,38], or flange-to-wall connection improvements [108–111], which do not contribute to understanding Flange effects in unreinforced masonry. Third, several studies [28,34,106] focus on URM specimens but do not explicitly analyze the impact of flanges on the main wall or compare flanged cases with non-flanged references. Lastly, one study [101] investigates Flange effects on the axial response of the URM walls only, which falls outside the present review's focus.

Table 1. Experimental studies on the effects of different interactions between IP and OOP behaviors in non-framed unreinforced masonry walls. For the meaning of abbreviations, please refer to the Nomenclature section. Parentheses show the number of specimens with the specific features.

Interaction Scenario	Year	Publication(s)	URM Interaction Tests (Number—Type)	Scale (Test/Reality)	Masonry Unit Type	Mortar Type	Masonry Prism Compressive Strength (f'_m) [MPa]	Opening Type	Flange Configuration *	Flange/Wall Length Ratio (l_f/l)	Height/Length Aspect Ratio (h/l)	Length/Thickness Slenderness Ratio (h/t)	No. Wythes	Wall Thickness (t) [mm]	Loading Scenario and Sequence	IP Loading (Procedure, Apparatus, Boundary Conditions)	OOP Loading (Procedure, Apparatus, Boundary Conditions)	Vertical Overburden Stress/Strength (Flanges + Wall) [%]
OOP/IP	2012	[56,71]	5—Wt	1:1	HCLB (V)	1:3 (C:S)	8.0	–	–	–	1.0	6	1	100	CB (OOP, IP)	QSM, DiC, –	QSM, WFMiPL, 2WB	0
	2015	[75]	5—Wt	1:1	SFAB	Dry-Joint	6.8	–	–	–	0.67	4	1	115	CB (OOP, IP)	QSM, DiC, –	QSM, WFMiPL, 2WB	9.2
	2015	[54,74]	1—NFW	1:1	SCLB	1:1:5 (C:L:S)	4.5	–	–	–	0.9	15.2	1	100	CB (OOP, IP)	QSM, ToD, DC	QSM, ToL, 1WB-Ct	16
			1—NFW	1:1	SCLB	1:1:5 (C:L:S)	4.5	–	–	–	1.0	15.9	1	100	CB (OOP, IP)	QSC, ToD, DC	QSM, ToL, 1WB-Ct	16
			2—NFW	1:1	SCLB	1:1:5 (C:L:S)	4.5 (1) 1.6 (1)	–	–	–	1.0	15.9	1	100	CB (OOP, IP)	QSC, ToD, DC	QSM, ToD, 1WB-Ct	16
	2023	[68]	2—NFW	1:1	SCLB	1:6 (C:S)	3.3	–	–	–	1.0	6.3	1	230	CB (OOP, IP)	QSM, ToD, Ct	QSM, ToD, 1WB-Ct	0
			2—NFW	1:1	SCLB	1:6 (C:S)	4.8	–	–	–	1.25	6.3	1	230	CB (OOP, IP)	QSM, ToD, Ct	QSM, ToD, 1WB-Ct	0
IP/OOP	2020	[72,73]	2—Wt	1:1	HCLB (H)	1:1:5 (C:L:S)	4.0	–	–	–	1.0	10.8	1	80	SQ (IP, OOP)	QSM, DiC, –	QSM, WF3PL, 1WB-B	0
F/IP	2010	[77,79,113]	2—FW	1:1	SCLB	1:2:9 (C:L:S)	18.1	–	⌶	0.24	0.63 (1) 1.0 (1)	5.2 (1) 8.2 (1)	2	230	IP	QSC, ToD, DC	–	0 + [0.1 to 0.6]
			1—FW	1:1	SCLB	1:2:9 (C:L:S)	10.1	–	⌶	0.12	0.5	8.7	2	230	IP	QSC, ToD, DC	–	0 + [0.1 to 0.6]
			3–FW	1:1	SCLB	1:2:9 (C:L:S)	9.2 (1) 11.9 (1) 9.1 (1)	–	⌶ (1) ⊤ (1) ⊏ (1)	0.24	0.5	8.7	2	230	IP	QSC, ToD, DC	–	0 + [0.1 to 0.6]
	2013	[78]	2—FW	1:1	SCSBL	Adhesive	27.3	–	⊤	0.20	2.5	14.8	1	175	IP	QSC, ToD, Ct	–	8 + 8 (1) 17 + 17 (1)
			2—FW	1:1	SCSBL	Adhesive	22.7	–	⊤	0.22	2.85	14.8	1	175	IP	QSC, ToD, Ct	–	9 + 9 (1) 20 + 20 (1)
	2014	[81]	1—FW	1:2	SCLB	2:13 (C:S)	3.24	–	⌶	0.25	0.48	8.4	1	160	IP	QSC, ToD, DC	–	3.1 + 3.1
			1—FW	1:2	SCLB	2:13 (C:S)	3.24	–	⊏	0.36	0.7	12.3	1	110	IP	QSC, ToD, DC	–	3.1 + 3.1
	2018	[83]	2—FW	1:1	SCLB	1:4 (C:S)	4.34	W	⊏	0.32	1.0	13.5	2	225	IP	QSC, ToD, DC	–	1.8 + 1.1 (1) 5.3 + 3.7 (1)
F/OOP	2014	[80]	2—FW	1:5	SMB	Dry-Joint	NS	–	⌜	0.8	0.63 (1) 0.9 (1)	14.9	1	40	OOP	–	QSM, BR, 1WB-Ct	0 + 0
			1—FW	1:5	SMB	Dry-Joint	NS	–	⌜	1.1	1.25	14.9	1	40	OOP	–	QSM, BR, 1WB-Ct	0 + 0
			1—FW	1:5	SMB	Dry-Joint	NS	–	⌞⌟	0.4	0.9	14.9	1	40	OOP	–	QSM, BR, 1WB-Ct	0 + 0
			5—FW	1:5	SMB	Dry-Joint	NS	–	⌞⌟	0.3	0.60 (1) 0.67 (4)	14.9	1	40	OOP	–	QSM, BR, 1WB-Ct	0 + 0
			2—FW	1:5	SMB	Dry-Joint	NS	–	⊤	1.1	1.25	14.9	1	40	OOP	–	QSM, BR, 1WB-Ct	0 + 0
			4—FW	1:5	SMB	Dry-Joint	NS	–	⊤	0.8	0.63 (2) 0.9 (2)	14.9	1	40	OOP	–	QSM, BR, 1WB-Ct	0 + 0

Table 1. *Cont.*

Interaction Scenario	Year	Publication(s)	URM Interaction Tests (Number—Type)	Scale (Test/Reality)	Masonry Unit Type	Mortar Type	Masonry Prism Compressive Strength (f'_m) [MPa]	Opening Type	Flange Configuration *	Flange/Wall Length Ratio (l_f/l)	Height/Length Aspect Ratio (h/l)	Length/Thickness Slenderness Ratio (h/t)	No. Wythes	Wall Thickness (t) [mm]	Loading Scenario and Sequence	IP Loading (Procedure, Apparatus, Boundary Conditions)	OOP Loading (Procedure, Apparatus, Boundary Conditions)	Vertical Overburden Stress/Strength (Flanges + Wall) [%]
			2—FW	1:5	SMB	Dry-Joint	NS	–	⊓	1.1	1.25	14.9	1	40	OOP	–	QSM, BR, 1WB-Ct	0 + 0
			2—FW	1:5	SMB	Dry-Joint	NS	–	⊓	0.8	0.63 (1) 0.9 (1)	14.9	1	40	OOP	–	QSM, BR, 1WB-Ct	0 + 0
			2—FW	1:5	SMB	Dry-Joint	NS	W	⊓	0.7	0.53	14.9	1	40	OOP	–	QSM, BR, 1WB-Ct	0 + 0
			3—FW	1:5	SMB	Dry-Joint	NS	– (2) D (OF) (1)	⫙	0.7	0.53	14.9	1	40	OOP	–	QSM, BR, 1WB-Ct	0 + 0
	2015	[84–86]	2—FW	1:1	HCLB (V)	1:2 (C:S) (DHJ)	5.6	D	⊓ (1) ⊢ (1)	0.18	1.67	14.3	1	140	OOP	–	Dyn, ST, 1WB-Ct	2.4 + 2.4 (1) 4.4 + 4.4 (1)
	2017	[82]	4—FW	1:10	SSB	Dry-Joint	NS	–	⊔	0.78 (1) 0.34 (1) 0.28 (1) 0.25 (1)	0.31 (1) 0.36 (1) 0.43 (1) 1.0 (1)	7.3	1	17	OOP	–	QSM, BR, 1WB-Ct	0 + 0

* Assuming that in the plan view, the loading direction is from bottom to the top of the configuration.

Table 2. Numerical studies on the effects of different interactions between IP and OOP behaviors in non-framed unreinforced masonry walls. For the meaning of abbreviations, please refer to the Nomenclature section. Parentheses show the number of specimens with the specific features.

Interaction Scenario	Year	Publication(s)	URM Interaction Specimens (Number—Type)	Numerical Modeling Approach	Masonry Unit Type	Mortar Type	Masonry Prism Compressive Strength (f'_m) [MPa]	Opening Type	Flange Configuration *	Flange/Wall Length Ratio (l_f/l)	Height/Length Aspect Ratio (h/l)	Length/ Thickness Slenderness Ratio (h/t)	No. Wythes	Wall Thickness (t) [mm]	Loading Scenario and Sequence	IP Loading (Procedure, Apparatus, Boundary Conditions)	OOP Loading (Procedure, Apparatus, Boundary Conditions)	Vertical Overburden Stress/Strength (Flanges + Wall) [%]	Pre-Damage Levels
OOP/IP	2013	[56]	3—NFW	CoB	HCLB (V)	1:3 (C:S)	8.0	–	–	–	0.5 (1) 1.0 (1) 2.0 (1)	30	1	100	CB (OOP, IP)	QSM, ToD, DC-RTU	QSM, WFP, 2WB-FR4E	0	6 (3)
	2014	[57]	5—NFW	CoB	HCLB (V)	1:3 (C:S)	8.0	–	–	–	1.0	20 (1) 30 (1) 36 (1) 40 (1) 60 (1)	1	100	CB (OOP, IP)	QSM, ToD, DC-RTU	QSM, WFP, 2WB-FR4E	0	6 (5)
			4—NFW	CoB	HCLB (V)	1:3 (C:S)	4.0 (1) 6.0 (1) 8.0 (1) 10.0 (1)	–	–	–	1.0	30	1	100	CB (OOP, IP)	QSM, ToD, DC-RTU	QSM, WFP, 2WB-FR4E	0	6 (4)
			60—NFW	CoB	HCLB (V)	1:3 (C:S)	8.0	–	–	–	0.5 (12) 1.0 (36) 2.0 (12)	30	1	100	CB (OOP, IP)	QSM, ToD, DC-RTU	QSM, WFP, 2WB-FR4E	0	6 (60)

Table 2. *Cont.*

Interaction Scenario	Year	Publication(s)	URM Interaction Specimens (Number—Type)	Numerical Modeling Approach	Masonry Unit Type	Mortar Type	Masonry Prism Compressive Strength (f'_m) [MPa]	Opening Type	Flange Configuration *	Flange/Wall Length Ratio (l_f/l)	Height/Length Aspect Ratio (h/l)	Length/ Thickness Slenderness Ratio (h/t)	No. Wythes	Wall Thickness (t) [mm]	Loading Scenario and Sequence	IP Loading (Procedure, Apparatus, Boundary Conditions)	OOP Loading (Procedure, Apparatus, Boundary Conditions)	Vertical Overburden Stress/Strength (Flanges + Wall) [%]	Pre-Damage Levels
	2014	[59]	17—NFW	SMSBB	SCLB	1:2:9 (C:L:S)	10.5	–	–	–	1.0	10.0	1	100	SM (IP + OOP)	QSM, ToD, DC-RTU	QSM, ToD, 1WB-DC-RTU	1.14	1 (17)
			1—NFW	SMSBB	SCLB	1:2:9 (C:L:S)	10.5	–	–	–	1.0	10.0	1	100	SM (IP + OOP)	QSC, ToD, DC-RTU	QSC, ToD, 1WB-DC-RTU	1.14	1 (1)
	2015	[61]	1—NFW	SMSBB	SCLB	1:2:9 (C:L:S)	3.5	–	–	–	1.0	10.0	1	100	SM (IP + OOP)	QSM, ToD, DC-RTU	QSM, WFP, 1WB-B-RTRU	1.14	17 (1)
	2017	[62]	28—NFW	SMSBB	SCLB	1:1:6 (C:L:S)	10.0	–	–	–	0.5 (7) 1.0 (7) 1.5 (7) 2.0 (7)	16.0	1	137	SQ (OOP, IP)	QSM, ToD, DC	QSM, MHD, 1WB-B	1 to 25	5 (28)
			28—NFW	SMSBB	SCLB	1:1:6 (C:L:S)	10.0	–	–	–	0.5 (7) 1.0 (7) 1.5 (7) 2.0 (7)	16.0	1	137	CB (OOP, IP)	QSM, ToD, DC	QSM, MHD, 1WB-B	1 to 25	5 (28)
	2018	[63]	12—NFW	CoB	HCB (V)	1:1:6 (C:L:S)	8.5	–	–	–	0.6 (4) 0.8 (4) 1.0 (4)	22.7	1	110	CB (OOP, IP)	QSM, ToD, Ct	QSM, WFP, 2WB-FR4E	0, 9.1 to 27.3	Various
	2018	[64]	11—NFW	CoB	HCLB (V)	1:2:9 (C:L:S)	7.0 (1) 11.0 (9) 15.0 (1)	–	–	–	1.0	22.7	1	110	CB (OOP, IP)	QSM, ToD, Ct	QSM, WFP, 2WB-FR4E-F1SE	0, 6.7 to 18.2	Various
			1—NFW	CoB	HCLB (V)	1:2:9 (C:L:S)	11.0	–	–	–	1.0	22.7	1	110	CB (OOP, IP)	QSM, ToD, Ct	QSM, WFP, 2WB-FR4E-FTE	0	7 (1)
	2019	[65]	28—NFW	SMSBB	SCLB	1:1:6 (C:L:S)	10.0	–	–	–	0.5 (7) 1.0 (7) 1.5 (7) 2.0 (7)	8.8	1	250	SQ (OOP, IP)	QSM, ToD, DC	QSM, MHD, 1WB-B	1 to 25	5 (28)
			4—NFW	SMSBB	SCLB	1:1:6 (C:L:S)	10.0	–	–	–	0.5 (2) 1.5 (2)	8.8	1	250	SM (IP + OOP)	Dyn, ST, DC	Dyn, ST, 1WB-B	1 to 25	10 (4)
	2022	[66]	5—NFW	SMSBB	SCLB	1:1:6 (C:L:S)	11.5	–	–	–	0.7	11.0	1	90	CB (OOP, IP)	QSM, ToD, DC	QSM, WFP, 1WB-B	0, 5 to 20	Various
			20—NFW	SMSBB	SCLB	1:1:6 (C:L:S)	11.5	–	–	–	1.0 (5) 1.5 (5) 2.0 (5) 2.5 (5)	11.0 (5) 16.5 (5) 22.1 (5) 27.7 (5)	1	90	CB (OOP, IP)	QSM, ToD, DC	QSM, WFP, 1WB-B	0, 5 to 20	Various
	2023	[76]	3—NFW	SMSBB	SCLB	1:2:9 (C:L:S)	16.0	–	–	–	1.3	37.3	1	110	CB (OOP, IP)	QSM, ToD, Ct	QSM, WFP, 2WB-FR3E-NLC	0 (1) 6.25 (1) 12.5 (1)	5 (3)
			3—NFW	SMSBB	SCLB	1:2:9 (C:L:S)	16.0	–	–	–	1.0	26.8	1	110	CB (OOP, IP)	QSM, ToD, Ct	QSM, WFP, 2WB-FR3E-NLC	0 (1) 6.25 (1) 12.5 (1)	5 (3)
			3—NFW	SMSBB	SCLB	1:2:9 (C:L:S)	16.0	–	–	–	0.5	13.4	1	110	CB (OOP, IP)	QSM, ToD, Ct	QSM, WFP, 2WB-FR3E-NLC	0 (1) 6.25 (1) 12.5 (1)	5 (3)
	2023	[68]	2—NFW	CoB	SCLB	1:6 (C:S)	3.1 (1) 4.7 (1)	–	–	–	1.0 (1) 1.25 (1)	6.3	1	230	CB (OOP, IP)	QSM, ToD, Ct	QSM, ToD, 1WB-Ct	0.0	4 (2)

Table 2. *Cont.*

Interaction Scenario	Year	Publication(s)	URM Interaction Specimens (Number—Type)	Numerical Modeling Approach	Masonry Unit Type	Mortar Type	Masonry Prism Compressive Strength (f'_m) [MPa]	Opening Type	Flange Configuration *	Flange/Wall Length Ratio (l_f/l)	Height/Length Aspect Ratio (h/l)	Length/Thickness Slenderness Ratio (h/t)	No. Wythes	Wall Thickness (t) [mm]	Loading Scenario and Sequence	IP Loading (Procedure, Apparatus, Boundary Conditions)	OOP Loading (Procedure, Apparatus, Boundary Conditions)	Vertical Overburden Stress/Strength (Flanges + Wall) [%]	Pre-Damage Levels
	2024	[69,94]	16—NFW	SMSBB	SCLB	1:1:6 (C:L:S)	11.5	–	–	–	1.0	9.9 (6) 15.5 (2) 21.1 (2) 32.2 (6)	1	100	CB (OOP, IP)	QSM, ToD, Ct	QSM, WFP, 1WB-B	0, 2.4 to 19.1	4 (16)
			6—NFW	SMSBB	SCLB	1:1:6 (C:L:S)	11.5	–	–	–	0.75	9.9	1	100	CB (OOP, IP)	QSM, ToD, Ct	QSM, WFP, 1WB-B	0, 2.4 to 19.1	4 (6)
			2—NFW	SMSBB	SCLB	1:1:6 (C:L:S)	11.5	–	–	–	1.5	9.9	1	100	CB (OOP, IP)	QSM, ToD, Ct	QSM, WFP, 1WB-B	0 (1) 19.1 (1)	4 (2)
			6—NFW	SMSBB	SCLB	1:1:6 (C:L:S)	11.5	–	–	–	2.25	9.9	1	100	CB (OOP, IP)	QSM, ToD, Ct	QSM, WFP, 1WB-B	0, 2.4 to 19.1	4 (6)
IP/OOP	2013	[55]	5—NFW	CoB	SCLB	1:1:6 (C:L:S)	7.6	–	–	–	0.85	10 (1) 12 (1) 20 (1) 25 (1) 30 (1)	1	300 (1) 250 (1) 150 (1) 120 (1) 100 (1)	SC (IP, OOP, IP)	QSC, ToD, DC	QSLUC, WFP, 1WB-B	2.78	12 (5)
			7—NFW	CoB	SCLB	1:1:6 (C:L:S)	7.6	–	–	–	0.34 (1) 0.4 (1) 0.5 (1) 0.67 (1) 0.85 (1) 1.0 (1) 1.34 (1)	16	1	187.5	SC (IP, OOP, IP)	QSC, ToD, DC	QSLUC, WFP, 1WB-B	2.78	12 (7)
	2015	[60]	1—NFW	SMSBB	SCLB	1:2:9 (C:L:S)	10.5	–	–	–	1.0	10.0	1	100	CB (IP, OOP)	QSM, ToD, Ct	QSM, WFP, 1WB-B	1.14	3 (1)
			2—NFW	SMSBB	SCLB	1:2:9 (C:L:S)	10.5	–	–	–	1.0 (1) 2.0 (1)	10.0 (1) 20.0 (1)	1	100	SQ (IP, OOP)	QSLUC, ToD, DC-RTU	QSM, WFP, 1WB-B-RTRU	1.14	3 (2)
			1—NFW	SMSBB	SCLB	1:2:9 (C:L:S)	10.5	–	–	–	1.0	10.0	1	100	SQ (IP, OOP)	QSC, ToD, Ct	QSM, WFP, 1WB-B	1.14	3 (1)
			2—NFW	SMSBB	SCLB	1:2:9 (C:L:S)	10.5	–	–	–	1.0 (1) 2.0 (1)	10.0 (1) 20.0 (1)	1	100	SQ (IP, OOP)	QSC, ToD, DC-RTU	QSM, WFP, 1WB-B-RTRU	1.14	3 (2)
	2023	[67]	3—NFW	SMSBB	SCSB	2:1:16 (C:L:S)	6.3	– (2) W (1)	–	–	0.7	27.0	1	100	SQ (IP, OOP)	QSC, ToD, DC	QSM, WFP, 2WB-FRSE	7.8 (IP)—0.8 (OOP)	4 (3)
			2—NFW	SMSBB	SCSB	2:1:16 (C:L:S)	6.3	– (1) W (1)	–	–	0.7	27.0	1	100	CB (IP, OOP)	QSM, ToD, DC	QSM, WFP, 2WB-FRSE	7.8 (IP)—0.8 (OOP)	4 (2)
	2024	[70]	27—NFW	SMSBB	SCLB	1:1:6 (C:L:S)	4.0	– (3) W (9) D (9) W + D (6)	–	0.18	1.0	27.3	1	110	CB (IP, OOP)	QSM, ToD, Ct	QSM, WFP, 2WB-FR3E-NLC	0 (9) 12.5 (9) 25 (9)	4 (27)
F/IP	2012	[91]	4—FW	CoB	Not Specified	Not Specified	4.2	–	⊥	0.7 (1) 0.8 (1) 0.9 (1) 1.0 (1)	1.43	10.8	1	240	IP	QSC, ToD, DC	–	0 + 14.2	–
	2013	[87]	8—FW	SMSBB	HCB (V)	1:3 (C:S)	6.0	–	⊥	0.36 (2) 0.65 (2) 0.9 (2) 1.2 (2)	1.0	14	1	200	IP	QSM, ToD, Ct (4) QSM, ToD, DC-RTU (4)	–	10 + 10 (4) 20 + 20 (4)	–

Table 2. *Cont.*

Interaction Scenario	Year	Publication(s)	URM Interaction Specimens (Number—Type)	Numerical Modeling Approach	Masonry Unit Type	Mortar Type	Masonry Prism Compressive Strength (f'_m) [MPa]	Opening Type	Flange Configuration *	Flange/Wall Length Ratio (l_f/l)	Height/Length Aspect Ratio (h/l)	Length/ Thickness Slenderness Ratio (h/t)	No. Wythes	Wall Thickness (t) [mm]	Loading Scenario and Sequence	IP Loading (Procedure, Apparatus, Boundary Conditions)	OOP Loading (Procedure, Apparatus, Boundary Conditions)	Vertical Overburden Stress/Strength (Flanges + Wall) [%]	Pre-Damage Levels
			4—FW	SMSBB	HCB (V)	1:3 (C:S)	6.0	–	⊤	0.36 (1) 0.65 (1) 0.9 (1) 1.2 (1)	1.0	14	1	200	IP	QSM, ToD, Ct	–	10 + 10	–
			8—FW	SMSBB	HCB (V)	1:3 (C:S)	6.0	–	⊥	0.36 (2) 0.65 (2) 0.9 (2) 1.2 (2)	1.0	14	1	200	IP	QSM, ToD, Ct (4) QSM, ToD, DC-RTU (4)	–	10 + 10 (4) 20 + 20 (4)	–
	2015	[92]	3—FW	CoB	HCB (V)	1:3 (C:S)	6.0	–	⊥	0.16 (1) 0.37 (1) 0.58 (1)	1.0	14	1	200	IP	QSM, ToD, Ct	–	10 + 10	–
	2021	[88,89]	60—FW	SMSBB	SCLB	1:4 (C:S)	4.3	–	⊥	0.1 (12) 0.25 (12) 0.5 (12) 0.75 (12) 1.0 (12)	0.6 (12) 0.84 (12) 1.1 (12) 1.43 (12) 2.0 (12)	13.9	1	230	IP	QSM, ToD, Ct	–	0 + 15 (20) 0 + 20 (20) 0 + 30 (20)	–
			60—FW	SMSBB	SCLB	1:4 (C:S)	4.3	–	⊥	0.1 (12) 0.25 (12) 0.5 (12) 0.75 (12) 1.0 (12)	0.6 (12) 0.84 (12) 1.1 (12) 1.43 (12) 2.0 (12)	13.9	1	230	IP	QSM, ToD, SCt	–	0 + 15 (20) 0 + 20 (20) 0 + 30 (20)	–
			60—FW	SMSBB	SCLB	1:4 (C:S)	4.3	–	⊥	0.1 (12) 0.25 (12) 0.5 (12) 0.75 (12) 1.0 (12)	0.6 (12) 0.84 (12) 1.1 (12) 1.43 (12) 2.0 (12)	13.9	1	230	IP	QSM, ToD, DC	–	0 + 15 (20) 0 + 20 (20) 0 + 30 (20)	–
			60—FW	SMSBB	SCLB	1:4 (C:S)	4.3	–	⊏	0.1 (12) 0.25 (12) 0.5 (12) 0.75 (12) 1.0 (12)	0.6 (12) 0.84 (12) 1.1 (12) 1.43 (12) 2.0 (12)	13.9	1	230	IP	QSM, ToD, Ct	–	0 + 15 (20) 0 + 20 (20) 0 + 30 (20)	–
			60—FW	SMSBB	SCLB	1:4 (C:S)	4.3	–	⊏	0.1 (12) 0.25 (12) 0.5 (12) 0.75 (12) 1.0 (12)	0.6 (12) 0.84 (12) 1.1 (12) 1.43 (12) 2.0 (12)	13.9	1	230	IP	QSM, ToD, SCt	–	0 + 15 (20) 0 + 20 (20) 0 + 30 (20)	–
			60—FW	SMSBB	SCLB	1:4 (C:S)	4.3	–	⊏	0.1 (12) 0.25 (12) 0.5 (12) 0.75 (12) 1.0 (12)	0.6 (12) 0.84 (12) 1.1 (12) 1.43 (12) 2.0 (12)	13.9	1	230	IP	QSM, ToD, DC	–	0 + 15 (20) 0 + 20 (20) 0 + 30 (20)	–
	2022	[90]	60—FW	SMSBB	SCLB	1:2:9 (C:L:S)	2.0 (24) 4.0 (12) 6.0 (12) 8.0 (12)	–	⊥	0.66	0.5 (15) 1.0 (15) 1.5 (15) 2.0 (15)	6.8 (15) 13.6 (15) 20.5 (15) 27.3 (15)	1	110	IP	QSM, ToD, DC-RTU	–	0 + 1.25 to 0 + 100	–
			48—FW	SMSBB	SCLB	1:2:9 (C:L:S)	2.0 (12) 4.0 (12) 6.0 (12) 8.0 (12)	–	⊤	0.66	0.5 (15) 1.0 (15) 1.5 (15) 2.0 (15)	6.8 (12) 13.6 (12) 20.5 (12) 27.3 (12)	1	110	IP	QSM, ToD, DC-RTU	–	0 + 1.25 to 0 + 100	–
			72—FW	SMSBB	SCLB	1:2:9 (C:L:S)	2.0 (36) 4.0 (12) 6.0 (12) 8.0 (12)	–	⊥	0.66	0.5 (18) 1.0 (18) 1.5 (18) 2.0 (18)	6.8 (18) 13.6 (18) 20.5 (18) 27.3 (18)	1	110	IP	QSM, ToD, DC-RTU	–	0 + 1.25 to 0 + 100	–

Table 2. *Cont.*

Interaction Scenario	Year	Publication(s)	URM Interaction Specimens (Number—Type)	Numerical Modeling Approach	Masonry Unit Type	Mortar Type	Masonry Prism Compressive Strength (f'_m) [MPa]	Opening Type	Flange Configuration *	Flange/Wall Length Ratio (l_f/l)	Height/Length Aspect Ratio (h/l)	Length/Thickness Slenderness Ratio (h/t)	No. Wythes	Wall Thickness (t) [mm]	Loading Scenario and Sequence	IP Loading (Procedure, Apparatus, Boundary Conditions)	OOP Loading (Procedure, Apparatus, Boundary Conditions)	Vertical Overburden Stress/Strength (Flanges + Wall) [%]	Pre-Damage Levels
			48—FW	SMSBB	SCLB	1:2:9 (C:L:S)	2.0 (12) 4.0 (12) 6.0 (12) 8.0 (12)	–	⊏	0.66	0.5 (12) 1.0 (12) 1.5 (12) 2.0 (12)	6.8 (12) 13.6 (12) 20.5 (12) 27.3 (12)	1	110	IP	QSM, ToD, DC-RTU	–	0 + 1.25 to 0 + 100	–
	2023	[76]	3—FW	SMSBB	SCLB	1:2:9 (C:L:S)	16.0	–	⌶ (1) ⊏ (1) ⊥ (1)	0.14	1.3	37.3	1	110	IP	QSM, ToD, Ct	–	0 + 0	–
			9—FW	SMSBB	SCLB	1:2:9 (C:L:S)	16.0	–	⌶ (3) ⊏ (3) ⊥ (3)	0.14	1.0	26.8	1	110	IP	QSM, ToD, Ct	–	0 + 0 (3) 12.5 + 12.5 (3) 25 + 25 (3)	–
			3—FW	SMSBB	SCLB	1:2:9 (C:L:S)	16.0	–	⌶ (1) ⊏ (1) ⊥ (1)	0.14	0.5	13.4	1	110	IP	QSM, ToD, Ct	–	0 + 0	–
	2024	[93]	16—FW	CoB	SCLB	Not Specified	2.7	–	⌶ (4) ⊤ (4) ⊏ (4) ⌈ (4)	1.5 (4) 1.0 (4) 0.75 (4) 0.5 (4)	0.5 (4) 0.75 (4) 1.0 (4) 1.5 (4)	15.0	1	200	IP	QSM, ToD, DC	–	3.7 + 3.7	–
			16—FW	CoB	SCLB	Not Specified	2.7	–	⌶ (4) ⊤ (4) ⊏ (4) ⌈ (4)	1.5 (4) 1.0 (4) 0.75 (4) 0.5 (4)	0.5 (4) 0.75 (4) 1.0 (4) 1.5 (4)	6.0	1	500	IP	QSM, ToD, DC	–	3.7 + 3.7	–
			16—FW	CoB	SCLB	Not Specified	2.7	–	⌶ (4) ⊤ (4) ⊏ (4) ⌈ (4)	1.5 (4) 1.0 (4) 0.75 (4) 0.5 (4)	0.5 (4) 0.75 (4) 1.0 (4) 1.5 (4)	8.6	1	350	IP	QSM, ToD, DC	–	1.8 + 1.8	–
			16—FW	CoB	SCLB	Not Specified	2.7	–	⌶ (4) ⊤ (4) ⊏ (4) ⌈ (4)	1.5 (4) 1.0 (4) 0.75 (4) 0.5 (4)	0.5 (4) 0.75 (4) 1.0 (4) 1.5 (4)	8.6	1	350	IP	QSM, ToD, DC	–	3.7 + 3.7	–
			16—FW	CoB	SCLB	Not Specified	2.7	–	⌶ (4) ⊤ (4) ⊏ (4) ⌈ (4)	1.5 (4) 1.0 (4) 0.75 (4) 0.5 (4)	0.5 (4) 0.75 (4) 1.0 (4) 1.5 (4)	8.6	1	350	IP	QSM, ToD, DC	–	7.3 + 7.3	–
	2024	[70]	27—FW	SMSBB	SCLB	1:1:6 (C:L:S)	4.0	– (3) W (9) D (9) W + D (6)	⌶	0.18	1.0	27.3	1	110	IP	QSM, ToD, Ct	–	0 + 0 (9) 12.5 + 12.5 (9) 25 + 25 (9)	–

Table 2. *Cont.*

Interaction Scenario	Year	Publication(s)	URM Interaction Specimens (Number—Type)	Numerical Modeling Approach	Masonry Unit Type	Mortar Type	Masonry Prism Compressive Strength (f'_m) [MPa]	Opening Type	Flange Configuration *	Flange/Wall Length Ratio (l_f/l)	Height/Length Aspect Ratio (h/l)	Length/ Thickness Slenderness Ratio (h/t)	No. Wythes	Wall Thickness (t) [mm]	Loading Scenario and Sequence	IP Loading (Procedure, Apparatus, Boundary Conditions)	OOP Loading (Procedure, Apparatus, Boundary Conditions)	Vertical Overburden Stress/Strength (Flanges + Wall) [%]	Pre-Damage Levels
F/OOP	2023	[76]	3—FW	SMSBB	SCLB	1:2:9 (C:L:S)	16.0	–	⊢ (1) ⨿ (1) ⊥ (1)	0.14	1.3	37.3	1	110	OOP	–	QSM, WFP, 2WB-FRTE-NLC	0 + 0	–
			9—FW	SMSBB	SCLB	1:2:9 (C:L:S)	16.0	–	⊢ (3) ⨿ (3) ⊢ (3)	0.14	1.0	26.8	1	110	OOP	–	QSM, WFP, 2WB-FRTE-NLC	0 + 0 (3) 6.25 + 6.25 (3) 12.5 + 12.5 (3)	–
			3—FW	SMSBB	SCLB	1:2:9 (C:L:S)	16.0	–	⊢ (1) ⨿ (1) ⊥ (1)	0.14	0.5	13.4	1	110	OOP	–	QSM, WFP, 2WB-FRTE-NLC	0 + 0	–
	2024	[70]	27—FW	SMSBB	SCLB	1:1:6 (C:L:S)	4.0	– (3) W (9) D (9) W + D (6)	⊢	0.18	1.0	27.3	1	110	OOP	–	QSM, WFP, 2WB-FRTE-NLC	0 + 0 (9) 12.5 + 12.5 (9) 25 + 25 (9)	–
F/IP-OOP	2013	[87]	4—FW	SMSBB	HCB (V)	1:3 (C:S)	5.95	–	⊥	0.36 (1) 0.65 (1) 0.9 (1) 1.2 (1)	1.0	14	1	200	SM (IP + OOP)	QSM, ToD, Ct	QSM, ToD, 1WB-Ct	10 + 10	4 (4)
			4—FW	SMSBB	HCB (V)	1:3 (C:S)	5.95	–	⊥	0.36 (1) 0.65 (1) 0.9 (1) 1.2 (1)	1.0	14	1	200	SM (IP + OOP)	QSM, ToD, DC-RTU	QSM, ToD, 1WB-DC-RTU	20 + 20	4 (4)
	2023	[76]	9—FW	SMSBB	SCLB	1:2:9 (C:L:S)	16.0	–	⊥ (3) ⊏ (3) ⊢ (3)	0.14	1.3	37.3	1	110	CB (OOP, IP)	QSM, ToD, Ct	QSM, WFP, 2WB-FRTE-NLC	0 + 0 (3) 6.25 + 6.25 (3) 12.5 + 12.5 (3)	Various
			9—FW	SMSBB	SCLB	1:2:9 (C:L:S)	16.0	–	⊥ (3) ⊏ (3) ⊢ (3)	0.14	1.0	26.8	1	110	CB (OOP, IP)	QSM, ToD, Ct	QSM, WFP, 2WB-FRTE-NLC	0 + 0 (3) 6.25 + 6.25 (3) 12.5 + 12.5 (3)	Various
			9—FW	SMSBB	SCLB	1:2:9 (C:L:S)	16.0	–	⊥ (3) ⊏ (3) ⊢ (3)	0.14	0.5	13.4	1	110	CB (OOP, IP)	QSM, ToD, Ct	QSM, WFP, 2WB-FRTE-NLC	0 + 0 (3) 6.25 + 6.25 (3) 12.5 + 12.5 (3)	Various
	2024	[70]	27—FW	SMSBB	SCLB	1:1:6 (C:L:S)	4.0	– (3) W (9) D (9) W + D (6)	⊥	0.18	1.0	27.3	1	110	CB (IP, OOP)	QSM, ToD, Ct	QSM, WFP, 2WB-FRTE-NLC	0 + 0 (9) 12.5 + 12.5 (9) 25 + 25 (9)	4 (27)

* Assuming that in the plan view, the loading direction is from bottom to the top of the configuration.

The limitations inherent to experimental works have led to an increasing reliance on numerical modeling as an alternative for studying interaction effects. Numerical simulations provide a cost-effective and flexible means to investigate interaction effects, enabling extensive parametric studies that account for factors challenging to control in physical tests, such as material variability, boundary conditions, and dynamic loading conditions. Their capacity to replicate full-scale structures further enhances their role in advancing masonry research and improving predictive models for seismic behavior [114]. As listed in Table 2, the numerical studies of interaction effects in non-framed URM walls follow two modeling methodologies, categorized based on their approach to the geometrical representation of masonry. The first, the simplified micro-scale block-based (SMSBB) modeling approach, represents masonry as an assembly of solid blocks, representing masonry units, connected by zero-thickness joints, representing mortar. SMSBB models follow a discrete cracking approach wherein the possible cracking and damaging paths of masonry are explicitly simulated via the discontinuity between the blocks. The second methodology, called the continuum-based (CoB) modeling approach, realizes the entire geometry of masonry as a continuum body representing the complete mortar-unit assembly, following a smeared cracking approach wherein the nonlinear behaviors are distributed throughout the continuum [115]. Further information regarding these modeling approaches is available in Ref. [116].

Despite the limited number of numerical studies explicitly addressing interaction effects in non-framed URM walls, they represent the dominant methodology in the literature, extrapolating available experimental findings to generate data across a wide range of scenarios. Specifically, 319, 779, and 62 specimens are studied numerically in 18 [55–70,76,94], 11 [41,70,76,82,87–93], and three [70,87,90] publications for direct IP-OOP interaction, flange, and F/IP-OOP interaction effects, respectively. Among the 319 numerical specimens studied under direct IP-OOP interaction effects, 84% focus on OOP/IP interaction, with only 50 [55,60,68,70] dedicated to IP/OOP interaction effects. Similarly, 87% of the 779 simulations addressing Flange effects focus on F/IP interaction effects, while only 42 examine F/OOP interaction effects [70,76]. The emphasis on IP behavior is understandable, as the IP response of individual walls forms the primary path for transferring lateral and vertical loads to the foundation in real-world structures, necessitating a thorough understanding of its variations under OOP/IP and F/IP interaction effects [68]. However, the lack of research on IP/OOP and F/OOP interactions is concerning, as URM walls are significantly weaker in the OOP direction compared to IP, and often lose OOP stability during earthquakes, leading to the loss of both lateral and vertical IP load-bearing systems and total structural collapse [74]. Moreover, in the case of direct interactions, IP damage leads to the loss of strength across the entire thickness of the walls along the crack path, which severely affects the OOP behavior. Addressing this gap is crucial for improving predictive capabilities and seismic mitigation strategies.

4. Current Findings Regarding Interaction Effects in Non-Framed URM Walls

This section reviews the findings of studies on direct IP-OOP interaction and Flange effects in non-framed URM walls, focusing on identifying the key parameters influencing these interaction mechanisms. The research on direct IP-OOP interaction effects [54–76] is analyzed in Section 4.1, while studies on Flange effects [77–93] are reviewed in Section 4.2. Additionally, publications addressing F/IP-OOP interaction effects [70,76,87] are explored within Section 4.2 to assess the potential impact of flanges on wall behavior under direct IP-OOP interaction effects. The direct IP-OOP interaction and Flange effects are generally evaluated based on their consequence on the IP and OOP strength, stiffness, and damage

propagation of the walls, with some studies also considering deformation capacity. Given the limited availability of experimental data, numerical simulations are regarded in the review as the primary source of information, providing the most comprehensive insights into wall-level behavior. Accordingly, experimental studies, while valuable, are used as supplementary references, particularly where numerical data on specific parameters remain unavailable. It should be noted that, given the extensive datasets generated in numerical studies, comprising thousands of data points to quantify interaction effects, and the thorough visualization and interpretation of these outcomes in the cited publications, this paper refrains from re-illustrating such data. Instead, only a written summary of the key findings is provided. Readers are encouraged to consult the referenced sources for further insights.

4.1. Direct Interactions: IP-OOP Interaction Effects

This section examines numerical and experimental studies on IP/OOP and OOP/IP interaction effects in non-framed URM walls. Given the larger body of research on OOP/IP interactions, these studies are first reviewed in Section 4.1.1. The remaining works addressing IP/OOP interactions are then analyzed in Section 4.1.2. Various IP and OOP boundary conditions are used in the study of direct IP–OOP interactions, each leading to complex behaviors and distinct effects on the wall response. A pictorial representation of the boundary conditions used in different studies, along with the typical crack patterns associated with them, is provided in Figure 3. Boundary conditions in the IP direction are shown in Figure 3A–C, and those in the OOP direction in Figure 3D–N. This figure is referenced throughout the section to support clearer communication of the discussions.

4.1.1. Effects of OOP Response on the IP Wall Behavior (OOP/IP Interaction Effects)

This subsection reviews eight wall tests [68,74] and 14 numerical publications [56,57,59,61–66,68,69,76,94] on OOP/IP interactions in non-framed URM walls. The 10 wallet tests [56,117] are excluded from the discussion as they focus only on changes in peak IP strength under simplified conditions resembling infill walls. In contrast, the wall tests are included in the review, as they provide a more comprehensive understanding of full-wall behavior up to collapse. However, their limited number and inconsistent findings prevent definitive conclusions. It should be noted that while all numerical studies investigate wall specimens, four works [56,57,63,64] rely on wallet test data for calibrating and validating their modeling approaches.

The influence of OOP pre-load or pre-deformation on the IP response, which has been the primary focus of existing OOP/IP interaction studies, varies from negligible to significant depending on boundary conditions, vertical pre-compression, geometry, material properties, and loading assumptions. The discussion first addresses the effects of OOP pre-load. Generally, low OOP pre-load (below 40% of OOP strength) does not alter the IP crack pattern but weakens diagonal strut formation in double-clamped walls and reduces vertical confinement in cantilever ones, leading to slight reductions in IP strength and stiffness. Moderate OOP pre-load (40–70% of OOP strength) causes partially cracked joints along the wall length, reducing the effective cross-section resisting IP load [63]. High OOP pre-load (above 70% of OOP strength) compromises overall wall stability, causing crushing at the compressed edge or increasing torsion and OOP deformation during the IP loading step. This often shifts the failure mechanism to a mixed IP and OOP collapse [63,66]. Both experimental and numerical studies limit OOP pre-load to values below the peak OOP capacity [61,66], ensuring walls retain enough OOP resistance to prevent collapse before IP loading.

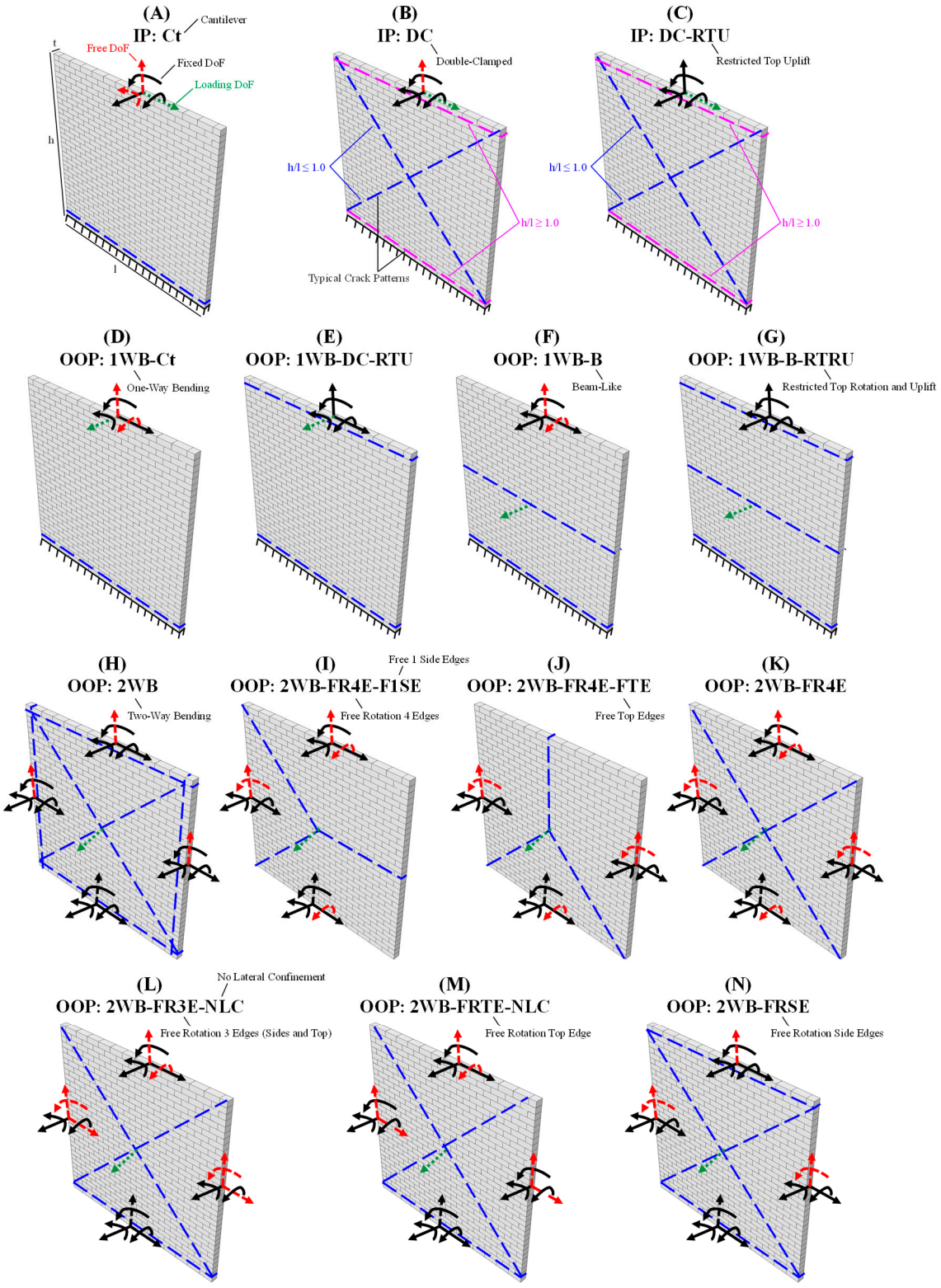

Figure 3. IP and OOP boundary conditions used to study the effects of the direct IP–OOP interaction on the behavior of non-framed unreinforced masonry walls, based on the available data. The IP boundary conditions include Ct (**A**), DC (**B**), and DC-RTU (**C**), while the OOP boundary conditions consist of 1WB-Ct (**D**), 1WB-DC-RTU (**E**), 1WB-B (**F**), 1WB-B-RTU (**G**), 2WB (**H**), 2WB-FR4E-F1SE (**I**) 2WB-FR4E-FTE (**J**), 2WB-FR4E (**K**), 2WB-FR3E-NLC (**L**), 2WB-FRTE-NLC (**M**), and 2WB-FRSE (**N**). Typical crack patterns associated with failure mode under each boundary condition are shown with dashed blue or pink lines. The abbreviation "DoF" stands for degree of freedom. Fixed, free, and loaded DoFs are shown with solid black, dashed red, and dotted green arrows, respectively. For the meaning of other abbreviations, please refer to the Nomenclature section.

For the case of OOP pre-deformation, a displacement-controlled setting is used. Hence, the pre-deformation can go beyond the elastic range. This case has a more prominent effect on IP strength and stiffness because the subsequent IP loading significantly reduces the effective cross-section and concentrates stresses at one end of the wall, causing flexural crushing under the combination of the loads, especially in cantilever walls [68]. Larger pre-deformation can also cause pure OOP to collapse due to complete loss of OOP resistance before the IP load-bearing capacity of the wall is utilized [62]. The influence of OOP pre-damage and simultaneous OOP loading will be discussed in the following subsections. The studies on OOP/IP interactions under OOP pre-damage do not show any different behaviors compared to the counterparts under OOP pre-deformation [62]. However, studies of IP/OOP interactions under simultaneous loading demonstrate slightly higher sensitivity to OOP/IP interactions [59,61,65]. The details of these interaction effects, along with the parameters influencing them, shown in Figure 4, are discussed in the following sub-sections. For the case of OOP pre-deformation, displacement-controlled loading is used to allow deformation beyond the elastic range, exerting a more pronounced effect on IP strength and stiffness. The pre-deformation significantly reduces the effective cross-section during IP loading and concentrates stresses at one end of the wall, causing flexural crushing, notably in cantilever walls [68]. Larger pre-deformation can even result in pure OOP collapse before the IP load-bearing capacity is mobilized [62].

The effects of pre-damage and simultaneous OOP loading are discussed in the subsequent sections. Moreover, the impacts of variation in different wall properties, shown for numerical specimens in Figure 4, on these interaction effects are investigated. In short, studies on OOP/IP interactions under OOP pre-damage show no distinct differences from those under OOP pre-deformation [62]. However, IP/OOP interactions under simultaneous loading exhibit slightly greater sensitivity to OOP/IP effects [59,61,65].

Boundary Conditions

Various boundary conditions for IP and OOP loading are adopted in different OOP/IP interaction studies, as illustrated in Figure 4A,B, respectively, to simulate the diverse interactions observed between masonry walls and surrounding structural elements in real-world buildings.

For IP boundary conditions, 24% of numerical simulations [63,64,68,69,76] and 50% of wall tests [68] assume a cantilever configuration (Figure 3A), where the top of the specimen is free to rotate about its OOP axis, mimicking the effects of flexible floor or roof diaphragms. In contrast, the double-clamped boundary condition (Figure 3B), which restricts this top rotation and represents rigid diaphragms, is applied in 42% of the numerical simulations [56,57,59,61,62,65] and the remaining four wall tests [74]. Finally, 34% of the numerical simulations [56,57,59,61] adopt a modified double-clamped setting (Figure 3C) that additionally prevents vertical translation at the top of the walls (termed vertical uplift).

A greater range of boundary conditions is adopted in the OOP direction. All eight wall experiments [68,74] use a one-way bending configuration, in which the OOP pre-load is applied at the top of the wall, allowing a cantilever-type OOP motion that simulates piers between openings in single-story buildings (Figure 3D). Only two numerical simulations (1% of the dataset) [68] follow this approach, while another 7% [59,61] use a double-clamped one-way bending setup with uplift restrictions at the top (Figure 3E). A majority of numerical simulations (53%) [62,65] adopt a modified one-way bending condition, restricting OOP displacement also at the top and imposing a beam-like motion, with OOP load applied either at wall mid-height or dynamically at the boundaries (Figure 3F). The remaining studies (39%) simulate two-way bending boundary conditions (Figure 3G), representative of full exterior walls restrained by perpendicular walls at the sides and

by the roof and base at their horizontal edges. However, the number of fixed edges and the rotational constraints applied at the edges vary. In ref. [64], 11 specimens (4%) assume one lateral edge to be completely unrestrained, representing exterior walls or interior ones interrupted by large openings or architectural features (Figure 3I). Moreover, one specimen (1%) in ref. [64] considers a free top edge, simulating exterior walls with flexible roof diaphragms or non-load-bearing interior walls (Figure 3J). The four edges of specimens in [56,57,63,64], comprising 31% of the dataset, are modeled with restrained OOP displacements, but free rotations during OOP deformation (Figure 3K). Finally, nine specimens (3% of data) in ref. [76] are supported on the four sides, with free top and side-edge rotations, and without restrictions to lateral IP horizontal movement of the side edges (Figure 3L).

The choice of boundary conditions plays the most critical role in governing OOP/IP interaction effects, as different constraints dictate distinct failure mechanisms during both IP and OOP loading. These variations, in turn, significantly alter the extent of interaction effects. Specifically, boundary conditions that promote similar crack propagation patterns in both IP and OOP loading phases tend to amplify interaction effects, as damage localization and stress redistribution follow similar paths in both directions.

For instance, the numerical study in ref. [65] on a square wall with height-to-length aspect ratio (h/l) equal to 1.0, height-to-thickness slenderness ratio (h/t) equal to 9.9, and masonry prism compressive strength (f'_m) equal to 10.0 MPa with double-clamped IP (Figure 3B) and one-way bending beam-like OOP (Figure 3F) boundary conditions reports only a 35% reduction in IP strength at the highest OOP pre-deformation (50% of thickness). In contrast, the experiment in ref. [68] on a geometrically similar wall (h/l = 1.0, h/t = 6.3, and (f'_m) = 4.8 MPa), but with cantilever IP (Figure 3A) and one-way bending cantilever OOP (Figure 3D) conditions, exhibits a significantly higher 67% drop in IP strength and an 80% reduction in stiffness at an OOP pre-deformation of just 2.6% of the thickness. This stark difference is attributed to the choice of OOP boundary conditions. In the first case, the beam-like OOP deformation induces horizontal cracking distributed along the mortar joints at mid-height of the wall, which has minimal impact on the subsequent diagonal cracking and shear resistance under double-clamped IP loading. Conversely, in the second case, the cantilever OOP deformation localizes the cracks in the bottom mortar joint, which reopens under a similar flexural (rocking) movement in IP loading, amplifying the interaction effects.

Similarly, the double-clamped IP (Figure 3B) response of walls tested in ref. [74] (h/l = 1.05, h/t = 15.9, and f'_m = 9.6 MPa) shows almost no sensitivity to OOP pre-load and pre-deformation imposed in a one-way bending cantilever OOP (Figure 3D) setting, with only a 20% reduction in IP stiffness and no change in IP strength at an OOP pre-deformation of 10% of the wall thickness. This is because the diagonal shear failure governing the IP response remains unaffected by the horizontal cracks formed under cantilever OOP loading. The differences in material properties and thickness between the three studies are not expected to have influenced the comparison, as damage in all cases is concentrated in mortar joints, which have similar properties in the cited studies. Furthermore, variations in wall slenderness are assumed to have a negligible effect on cantilever OOP deformation and its resulting damage patterns [62].

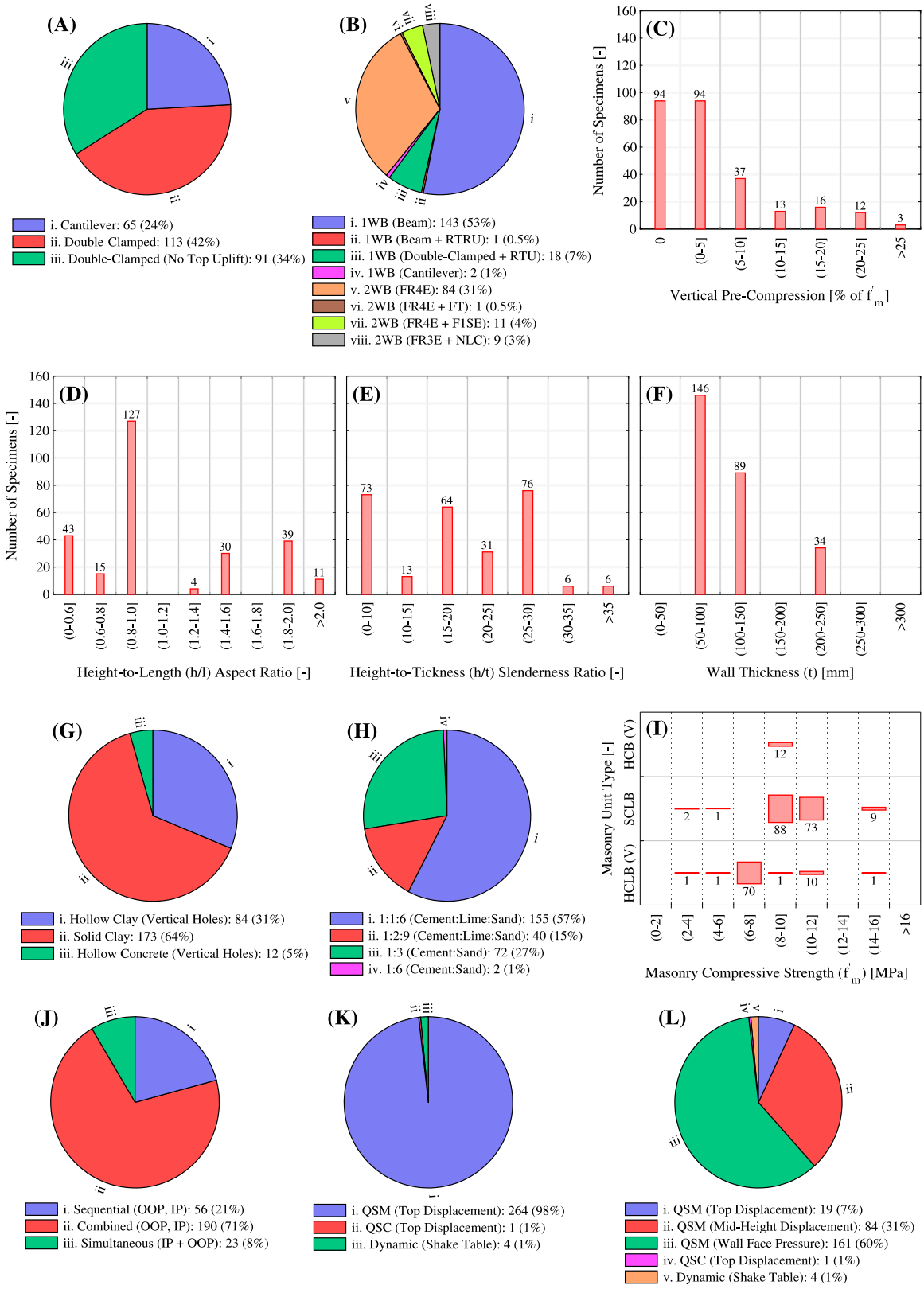

Figure 4. Overview of numerical studies focusing on the effects of OOP response on the IP behavior (OOP/IP interaction) in non-framed unreinforced masonry walls: classification of the specimens based on IP (**A**) and OOP (**B**) boundary conditions, amount of vertical pre-compression (**C**), aspect ratio (**D**), slenderness ratio (**E**), thickness (**F**), type of masonry (**G**), mortar mixture (**H**), compressive strength of masonry (**I**), loading scenario (**J**), and IP (**K**) and OOP (**L**) loading procedure and apparatus. For the meaning of abbreviations, please refer to the Nomenclature section.

Walls subjected to OOP load simultaneous to IP loading with low OOP:IP component proportions (as high as 4:1) at their top under a double-clamped boundary condition with fixed uplift (Figure 3C for IP and Figure 3E for OOP) in ref. [59] develop horizontal cracks at both the top and bottom mortar joints, rather than only a single base crack seen in cantilever OOP pre-loading conditions. Nevertheless, these walls exhibit similar OOP/IP interaction effects (under double-clamped fixed-uplift IP loading) when compared to experimental specimens tested under regular cantilever OOP conditions [74]. This is again attributed to the fact that horizontal cracks formed during OOP loading do not interact with diagonal shear cracks developed in the subsequent IP phase, reinforcing the critical role of boundary conditions in governing interaction effects.

A comparison between refs. [66] and [56] further illustrates how the IP double-clamped shear failure mechanism is more affected when a two-way bending OOP pre-loading is adopted rather than one-way bending. Two square walls (h/l = 1.0, h/t = 16.5 and 20, and f'_m = 8 MPa) with double-clamped IP (Figure 3B) boundary conditions are subjected to different OOP pre-loading conditions, one to one-way bending beam-like pre-loading (Figure 3F) in ref. [66] and one to two-way bending OOP pre-loading (Figure 3K) in ref. [56]. The results indicate that even high one-way bending pre-load, reaching up to 85% of the OOP strength, causes only a 30% reduction in IP strength in the first wall. Whereas the wall undergoing two-way bending pre-load exhibits the same degree of IP degradation already at a pre-load level 50% of OOP strength, and shows a 50% IP strength drop at 85% pre-load. This is attributed to the diagonal cracking induced by two-way bending, which mirrors the crack patterns typically seen in double-clamped IP (Figure 3B) loading, exacerbating the interaction effects. In contrast, a similar wall (h/l = 1.0, h/t = 22.7, and f'_m = 8.55 MPa) modeled in ref. [63] under two-way bending OOP pre-load but with cantilever IP boundary conditions shows only a 4% reduction in IP strength at 50% pre-load. It should be noted that, at a higher OOP pre-load (85% of wall strength), the formation of horizontal cracks at the base and sides significantly impacts the IP response of the wall, resulting in a 55% strength reduction. Nevertheless, this suggests a lower sensitivity of cantilever walls to moderate two-way bending pre-load, as the IP rocking cracks initially do not intersect with those formed during OOP loading.

For the 12 specimens modeled with a free edge in ref. [64], one wall with a free top edge (Figure 3J) exhibits no difference in OOP/IP interaction effects compared to its fully supported counterpart (Figure 3K) in ref. [63]. However, the 11 walls with free side edges demonstrate a reduced sensitivity to OOP pre-load, showing only a 10% reduction in IP strength at OOP pre-load as high as 85% of their total OOP strengths. Their fully supported reference wall experiences a 40% reduction in IP strength under the same pre-load level. This disparity is attributed to different OOP crack propagation patterns. In the three-side-supported walls with a free right edge (under zero to moderate pre-compression), the supported (left) side exhibits diagonal cracks extending from the corners to the mid-height, similar to fully supported walls. Meanwhile, the unsupported (right) side only develops a horizontal crack extending from the mid-height to the free edge, which aligns less with the subsequent cantilever IP crack pattern, minimizing the impact on IP behavior.

Lateral confinement also plays a significant role in OOP/IP interactions. The square wall in ref. [76] (h/l = 1.0, h/t = 26.8, and f'_m = 16 MPa) subjected to two-way bending OOP pre-loading with free lateral movement of its side edges (Figure 3K) retains only 60% of its double-clamped IP strength when exposed to an OOP pre-load at 60% of its total OOP strength. This is 20% lower than a similar wall (h/l = 1.0, h/t = 22.7, and f'_m = 8.5 MPa) simulated in ref. [63] under identical OOP pre-load but with lateral confinement (Figure 3L). Although both walls exhibit similar crack patterns under OOP loading, the absence of lateral confinement in the first case reduces horizontal arching effects, lead-

ing to larger OOP crack openings. This, in turn, accelerates the degradation of IP strength despite the non-confined wall being made of stronger masonry materials.

Vertical Pre-Compression

Vertical compressive load applied at the top of the walls before IP and OOP loading is incorporated in 65% of numerical simulations [59,61–66,69,76] and in four wall tests [74] to replicate the behavior of load-bearing walls in single- or multi-story buildings. The remaining specimens [56,57,63,64,66,68,69,76] are studied without pre-compression, representing non-load-bearing walls. Figure 4C illustrates the distribution of vertical pre-compression magnitudes used across different studies.

Numerical sensitivity analyses on the effects of vertical pre-compression are present in refs. [62–64,66,69,76] wherein a broad range of pre-compression values is explored, varying from 1% to 27% of f'_m. Lower pre-compression levels, up to 5% of f'_m, significantly mitigate OOP/IP interaction effects by maintaining higher IP strength under different OOP pre-loads. As shown in ref. [69] for a square wall ($h/l = 1.0$, $h/t = 32.2$, $f'_m = 11.5$ MPa), this effect arises because pre-compression limits vertical displacement at the top of the wall, enhancing confinement through the activation of vertical arching during OOP loading and diagonal compressive struts during IP loading. In this case, the pre-compressed wall exhibits up to 40% lower IP strength degradation at an OOP pre-load equal to 80% of its OOP strength compared to the non-compressed one. On the other hand, ref. [63] reports that higher pre-compression levels can have adverse effects. For a similar wall ($h/l = 1.0$, $h/t = 22.7$, $f'_m = 8.5$ MPa), moderate pre-compression up to 10% of f'_m leads to crushing and a slight reduction in the effective cross-section, causing a 20% greater IP stiffness drop for the wall at an OOP pre-load of 80% of its OOP capacity. Pre-compressions between 10% and 18% of f'_m do not further increase IP strength reduction, but alter the IP deformation of cantilever walls from flexural to a more shear-dominant mode by restricting top-edge rotation [66]. More extreme cases, with pre-compression between 18% and 28% of f'_m, show another increase in IP strength reduction, up to 20% higher in ref. [62], as crushing failures occur at all OOP pre-load levels. The IP double-clamped walls exhibit lower sensitivity to pre-compression compared to IP cantilever walls, since their boundary condition inherently confines their IP deformation and dictates an IP shear failure, similar to what increasing pre-compression does for cantilever walls [66].

The effects of pre-compression are more pronounced in tall walls ($h/l > 1.0$), regardless of the IP boundary conditions, since they show flexural response IP that is more sensitive to vertical load variations [62,76]. For example, the tall ($h/l = 1.4$) IP double-clamped (Figure 3B) wall under moderate vertical pre-compression in ref. [76] shows 20% higher IP strength under a two-way bending OOP pre-load (Figure 3L) of 80% of its strength compared to when no pre-compressions are applied. Meanwhile, the response of square and squat ($h/l = 0.5$) walls in the study to OOP/IP interaction effects shows no sensitivity to the amount of vertical pre-compression.

Wall Geometry

The numerical simulations and wall tests are conducted exclusively on full-scale, single-wythe masonry specimens without openings. As a result, this study lacks the necessary information regarding the influence of multiple wythes or perforations on OOP/IP interactions. However, a wide range of specimens with different height-to-length aspect ratios (h/l), height-to-thickness slenderness ratios (h/t), and thicknesses are studied, as illustrated in Figure 4D–F, respectively. Numerical studies encompass a broad spectrum of geometries, ranging from tall slender walls ($h/l > 1.0$ and $h/t > 20$) to squat thick walls ($h/l < 1.0$ and $h/t < 10$). In contrast, experimental campaigns primarily focus on square-like

walls (h/l≃1.0), with the four specimens in ref. [68] exhibiting a low slenderness ratio (h/t = 6.3) and the four specimens in ref. [74] being significantly more slender (h/t≃15.5). Figure 4D further reveals that, while tall and square geometries are well represented in numerical simulations, squat walls (h/l < 0.9) account for only 21% of the data. Additionally, although a variety of slenderness ratios are considered, as shown in Figure 4E, they are primarily obtained by modifying the height while changing the thickness between three dominant categories (50–100 mm, 100–150 mm, and 200–250 mm). As a result, Figure 4F highlights a lack of data for extremely thin (t < 50 mm) and thick (t > 250 mm) walls. Although the lack of data, for instance, for extremely thin walls, is justified since such extreme configurations are rarely used in construction practices.

The numerical sensitivity studies [56,62,63,66,69,76] demonstrate that the effect of aspect ratio on OOP/IP interactions is highly dependent on the adopted IP and OOP boundary conditions, as well as the level of vertical pre-compression. The lowest sensitivity is observed in the IP cantilever (Figure 3A) walls of ref. [63], pre-loaded under a two-way bending OOP configuration (Figure 3K), where different wall geometries exhibit similar behavior across different pre-compression levels and OOP pre-load. This is attributed to the fact that, in this setup, OOP pre-load does not significantly alter the IP failure mechanism. Conversely, the highest sensitivity is reported in ref. [56], where double-clamped IP (Figure 3B) and two-way bending OOP (Figure 3K) boundary conditions are applied with zero pre-compression. The squat specimen (h/l = 0.5) exhibits minimal sensitivity to OOP/IP interaction effects, retaining 70% of its IP strength under an OOP pre-load equal to 80% of its OOP strength. In contrast, the tall specimen (h/l = 2.0) reaches the same IP strength drop at a lower OOP pre-load level (55% of OOP capacity) and maintains only 30% of its IP strength at 80% OOP pre-load. Both walls develop similar diagonal cracks during OOP pre-loading, but the tall wall undergoes rocking deformation in the IP phase, which, when combined with the OOP arching effect, results in increased crushing and greater degradation of IP strength. On the contrary, the squat wall exhibits a shear-dominated IP failure mechanism that remains largely unaffected by the vertical stresses. These findings align with the observations of ref. [76].

In [62,66,69], a one-way bending beam-like OOP (Figure 3F) boundary condition is adopted. Among them, ref. [66] applies double-clamped IP (Figure 3B) constraints with OOP pre-loading, ref. [62] simulates double-clamped IP (Figure 3B) walls subjected to OOP pre-deformation, and ref. [69] considers cantilever IP (Figure 3A) conditions with OOP pre-load. Despite the different configurations, all three studies report comparable behavior between squat (h/l = 0.5–0.75) and square walls (h/l = 1.0). In ref. [69], the aspect ratio has almost no influence on the interaction, as the crack forming at the base during the cantilever IP (Figure 3A) loading phase remains unaffected by the mid-height crack induced by the OOP pre-load (Figure 3F). Consequently, the IP response remains the same across different geometries. However, notable differences arise in refs. [62,66] when transitioning from square walls to tall walls (h/l > 1.5), with OOP pre-load or pre-deformation causing up to 40% lower IP strength reductions. This trend aligns with previous findings, as the double-clamped IP response of tall walls (Figure 3B) involves rocking deformation with horizontal cracks forming at the top and bottom bed joints, making them less susceptible to one-way bending OOP action (Figure 3F) than shorter walls with IP cracks developing at their mid-heights. Notably, as vertical pre-compression increases, these differences diminish, and all geometries converge toward similar behavior due to crushing failures occurring across all pre-load and pre-deformation levels. However, this effect is less pronounced in walls subjected to two-way bending OOP pre-loading [56,62,63,66,69,76], as their response remains less sensitive to variations in pre-compression.

The influence of slenderness ratio on OOP/IP interaction also varies depending on the adopted boundary conditions. Specifically, its impact is minimal when walls are subjected to one-way bending beam-like OOP pre-loading or pre-deformation combined with double-clamped IP loading, as demonstrated in ref. [62,66]. This is because the OOP response of one-way bending walls, along with the associated damage and crack patterns, remains largely independent of wall thickness, provided that pre-compression is applied concentrically or in the absence of vertical load [118]. When IP boundary conditions are changed to cantilever, increasing the slenderness ratio results in a more pronounced amplification of interaction effects under one-way bending OOP pre-loading in the square walls (h/l = 1.0) simulated in ref. [69]. This is attributed to the higher second-order moments induced by the OOP pre-load in slender walls (h/t = 32.2), which contribute to a 20% greater reduction in IP strength at an 80% OOP pre-load level compared to thicker walls (h/t = 9.9).

On the other hand, ref. [57] reports that under two-way bending OOP pre-load and double-clamped IP deformation, a configuration particularly sensitive to interaction effects, thicker walls (h/l = 1.0 and h/t = 20.0) exhibit 20% higher IP strength reductions across all pre-load levels compared to thinner walls (h/l = 1.0 and h/t = 60.0), ultimately retaining only 50% of their IP capacity at an 80% OOP pre-load. This is explained by the lower arching action in slender walls, which reduces compressive stresses and the likelihood of crushing failures during both OOP and IP loading. Nevertheless, when large slenderness ratios, more commonly observed in real-world constructions (h/t = 20–30), are considered, the variations in interaction effects remain minor. Although additional studies for lower slenderness ratios (h/t < 20) under double-clamped IP and two-way bending OOP boundary conditions do not exist, it is assumed that the influence of slenderness ratio on OOP/IP interaction can generally be disregarded in this configuration.

Materials Properties

The classification of numerical specimens based on the type of masonry units and mortar compositions used in simulations is illustrated in Figure 4G,H, respectively. The majority of numerical studies are conducted on walls constructed with solid clay bricks (64%) or hollow clay blocks with vertically oriented holes (31%). A smaller subset of 12 walls (5%) in ref. [63] features hollow concrete blocks with vertical holes. Similarly, the eight experimental walls tested in refs. [68,74] are built using solid clay bricks, which aligns with the dominant material choice adopted in numerical models. Regarding mortar composition, simulations primarily consider cement-based mortars, either with (72%) or without (38%) lime binder. The compressive strength of masonry, derived from uniaxial loading of the masonry assemblies used in numerical studies, is presented in Figure 4I. The data indicate a predominant focus on high-strength materials in the available research, with compressive strengths ranging between 6 and 12 MPa.

The influence of material properties, such as masonry compressive strength, on OOP/IP interaction effects is investigated in the numerical simulations of refs. [57,64] on square walls (h/l = 1.0) constructed with hollow clay blocks. The study in ref. [57] applies two-way bending OOP pre-load (Figure 3K), followed by double-clamped IP loading (Figure 3B), while ref. [64] considers two-way bending OOP pre-loading with a free side edge (Figure 3I), followed by cantilever IP (Figure 3A) deformation. Although unidirectional IP and OOP responses exhibit sensitivity to all material variations, only specific properties significantly affect OOP/IP interaction, and their impact varies depending on the IP failure mode and boundary conditions.

In cantilever IP (Figure 3A) walls ref. [64], the most influential parameters are the tensile strengths of masonry in the vertical and horizontal directions, which govern both the extent of damage imposed by OOP pre-load and the crack re-opening during subsequent

flexural IP deformation. However, even substantial increases, 133% in vertical tensile strength or 200% in horizontal tensile strength, only slightly alter OOP/IP interactions, likely due to the inherently low sensitivity of cantilever IP walls to two-way bending OOP pre-load (Figure 3K). Conversely, in double-clamped IP walls [57], the tensile strength and elastic modulus of masonry in the horizontal direction are identified as the most critical factors. Within the continuum-based modeling approach of ref. [57], these parameters represent the tensile stiffness and strength of vertical mortar joints and masonry units, as well as the shear stiffness and strength in horizontal joints, all of which influence diagonal cracking in two-way bending OOP deformation and the shear failure mode of double-clamped IP (Figure 3B) walls. Reducing the tensile strength by 50% (from 2 MPa to 1 MPa) leads to an average 40% increase in IP strength reduction at an OOP pre-load of 80% of capacity, likely due to crack diffusion across larger wall areas during OOP pre-loading and IP deformation. Reducing the horizontal elastic modulus by 50% (from 16 GPa to 8 GPa) results in a 20% reduction in OOP/IP interaction effects at the same OOP pre-load level, attributed to increased stress concentration of cracking in mortar joints due to the larger stiffness.

Despite expectations that compressive strength would significantly influence interaction effects due to its role in controlling crushing failures, both studies report low sensitivity to variations in horizontal and vertical compressive strengths. This is likely due to the parameter being tested only within a high range (4–10 MPa) and the absence of pre-compression (0 MPa applied). Additional sensitivity analyses are not conducted for other combinations of IP and OOP boundary conditions, such as double-clamped IP walls (Figure 3B) under one-way bending OOP loading or cantilever IP walls under one-way bending OOP pre-load (Figure 3D–G). However, it is reasonable to infer that OOP/IP interaction effects would remain low in the former due to minimal interaction of IP and OOP responses in these boundary conditions, while the latter would exhibit sensitivity to the tensile strength of horizontal mortar joints, as cracks primarily develop in these regions.

Loading Scenario and Methodology

The classification of numerical studies based on loading scenarios, procedures, and apparatus used to investigate OOP/IP interaction effects is illustrated in Figure 4J–L, respectively. In terms of loading scenarios, all wall tests and 70% of numerical simulations examine OOP/IP interactions under the CB loading sequence, where OOP load or deformation is applied and then held constant during the subsequent IP loading phase. The remaining numerical simulations adopt an SQ approach in 56 cases (21%) [62,65] and an SM approach in 23 cases (9%) [59,61,65]. Regarding loading procedures, 97% of studies apply OOP pre-load, pre-deformation, or pre-damage using quasi-static monotonic (QSM) loading. Only one SM specimen in [59] and four in ref. [65] employ quasi-static cyclic (QSC) and dynamic (Dyn) OOP loads, respectively. Similarly, IP loading is applied using QSM in 98% of numerical simulations and five wall tests [68,74]. The exceptions include 3 CB wall tests in ref. [74] and one SM specimen in ref. [59], which apply QSC IP loading, as well as four SM specimens in [65] subjected to dynamic IP loading. A variety of loading apparatuses are used for OOP loading. In CB studies, OOP pre-deformation is imposed as displacements either at the top (1% of specimens [68]) or mid-height of the walls (10% of specimens [62]). SQ studies pre-damage the specimens via mid-height OOP displacements. SM specimens are loaded in the OOP direction using top displacements in 19 cases [59,61], while the four dynamic SM simulations in ref. [65] assume the use of a shake table. The IP load of all specimens is applied as top displacements, except for the four dynamic SM simulations in ref. [65] using a shake table. The following analyze the data within

each loading scenario to evaluate the influence of these loading assumptions on OOP/IP interaction effects.

- OOP Pre-Load and Pre-Deformation

In the CB loading scenario, a distinction is made between OOP pre-load and pre-deformation, with the former applied in 59% of numerical simulations and two wall tests [74], and the latter used in 11% of numerical simulations [62,68] and the remaining six wall tests [68,74]. The choice between these methods depends on the study objectives and available testing facilities, and it can lead to different interaction effects. Pre-deformation, imposed by applying and maintaining a specific displacement, simulates structures that have undergone irreversible deformation from prior loading events. In this method, the OOP displacements remain fixed during subsequent IP loading. In contrast, OOP pre-load, applied as a fraction of the total OOP strength of the walls, allows displacements to evolve during IP loading, potentially leading to nonlinear behavior or even OOP collapse as IP damage progresses.

The experiments in ref. [74] show that the two pre-loaded walls are prone to collapse in the OOP direction with the progression of IP damage. In contrast, the two pre-deformed identical walls maintain stability up to IP failure, although the two pairs of walls show similar IP stiffness and strengths. Hence, the amount of OOP pre-load is considered within the elastic range of the OOP response of the wall (usually causing drifts as much as 10% of the thickness), whereas large pre-deformation as much as 50% of the wall thickness is also adopted [62]. Comparison of the walls simulated in refs. [66] and [69] further highlights this difference. The walls have similar geometries, material properties, and pre-compression levels ($h/l = 1.5$, $h/t = 16.5$, $f'_m = 11.5$ MPa, 10% vertical load). While both use double-clamped IP and one-way bending beam-like OOP boundary conditions, the former has OOP pre-load simulating airbag load, and the latter is subjected to OOP mid-height pre-deformation. The strength drop begins at an OOP pre-load of 80% of capacity in the first wall, which corresponds to the same OOP pre-deformation level observed at the first IP strength drop of the second wall. However, the first wall fails after 99% pre-loading as it cannot maintain equilibrium due to increased OOP deformation during IP loading. In comparison, the second wall maintains stability even with five times larger OOP pre-deformation, and fails due to flexural crushing of the cross-section under mixed IP and OOP loads.

The influence of IP and OOP loading procedures on CB interaction effects remains largely unexplored, as most studies adopt QSM loading for both directions. The limited data available in ref. [74] suggest no significant difference in the three CB wall tests that use QSC IP loading compared to one wall in the same study that employs QSM IP loading.

- OOP Pre-Damage

Regarding the OOP/IP interaction effects under OOP pre-damage in the SQ loading scenario, refs. [62,65] numerically investigate walls with varying aspect ratios subjected to mid-height one-way bending beam-like OOP pre-deformation, followed by IP loading under double-clamped top displacement. The results indicate no significant difference in IP strength degradation compared to CB-loaded counterparts. However, a key distinction is that in SQ loading, the OOP instability and compressive failure typically associated with OOP pre-load or pre-deformation in CB loading do not occur. Instead, the impact of pre-damage is primarily reflected in the reduction of the effective cross-section available to resist IP load.

- OOP Simultaneous Load

Studies on OOP/IP interaction effects in SM loading scenarios [59,61,65] do not include direct comparisons with reference simulations under other loading scenarios. However,

they provide valuable insights into OOP/IP interactions during SM loading and the influence of different loading procedures, including QSC and dynamic loading.

Ref. [59] investigate numerically 18 square walls (h/l = 1.0, h/t = 10.0) subjected to bi-directional displacement-controlled top loading with IP (Figure 3C) and OOP (Figure 3E) double-clamped boundary conditions with fixed uplift. In 17 specimens, OOP and IP loads are applied as QSM displacements with varying proportions from 1:4 to 50:1 (OOP:IP ratio) to assess changes in IP and OOP responses as the total load gradually transitions from IP to OOP. The results show that the IP shear mechanism dominates up to a 3:1 OOP:IP ratio, while intermediate proportions (3:1 to 9:1) exhibit mixed failure modes involving shear cracking, OOP rocking, and base torsion. Higher OOP proportions (10:1 and beyond) lead to a transition towards OOP flexural failure. The total peak strength remains nearly equal to the pure IP strength up to a 3:1 proportion, experiencing only a 20% reduction up to 10:1 (corresponding to an 84° deviation of the applied total load from the IP direction). The reaction force direction remains primarily IP until 3:1 and deviates by only 7.5° at 10:1. Only the application of higher OOP:IP load proportions leads to a drastic transition of the amount and direction of the total strength towards pure OOP, which is significantly less than the IP strength in terms of magnitude. Furthermore, while the individual IP and OOP initial stiffness components remain unchanged across loading proportions, the total stiffness in the loading direction gradually reduces towards the pure OOP stiffness, exhibiting a smoother transition compared to the strength drop. Regardless of the initial loading proportion, the reaction force inclination shifts towards the IP direction as damage progresses. The IP component of the displacement at peak load remains similar across all proportions, but the total displacement is primarily dictated by the OOP component. The study also includes one wall subjected to QSC loading at a 3:1 proportion, which follows the same mixed failure mode and OOP/IP interaction patterns as its QSM counterpart, suggesting no significant differences due to cyclic loading at this proportion.

Ref. [65] analyze one tall (h/l = 1.5) and one squat (h/l = 0.5) wall (both h/t = 16) under two pre-compression levels (2% and 10%) subjected to 10 sets of bidirectional tectonic ground motions (equal PGAs in both directions) scaled incrementally in a dynamic analysis (IDA). IP motion is applied at the base only under a double-clamped configuration (Figure 3B), while OOP accelerations are imposed at the top and bottom of the walls in a one-way bending beam-like condition (Figure 3F). The averaged envelop force-displacement curves (extracted from the dynamic analyses) reveal a 30% reduction in peak and residual IP strengths compared to reference simulations under QSM loading (applied IP at the top of the specimen and OOP at the mid-height). The tall wall also exhibits up to a 10% lower initial IP stiffness, particularly under the higher pre-compression level. These findings suggest that OOP/IP interaction effects may be more severe during actual seismic events than in quasi-static analyses. However, since there is no comparison with a reference case (under IP or OOP dynamic loading), this might relate to more severe dynamic effects in general, not necessarily caused by OOP/IP interaction effects.

4.1.2. Effects of IP Response on the OOP Wall Behavior (IP/OOP Interaction Effects)

The four numerical publications [55,60,67,70] that investigate IP/OOP interaction effects in non-framed URM walls are reviewed in this section. The two wallet tests in refs. [72,73] are excluded, as these specimens do not show any OOP resistance because of excessive IP pre-damage. Compared to OOP/IP interaction effects, significantly fewer numerical simulations have been conducted on IP/OOP interaction effects (50 vs. 269). Nonetheless, these studies provide valuable preliminary sensitivity analyses on the role of geometrical and loading parameters, offering critical insights into factors governing IP/OOP interactions. While IP pre-load, pre-deformation, or pre-damage in IP/OOP inter-

actions can stem from various sources, existing research [55,60,67,70] has predominantly focused on those induced by seismic actions. Only one numerical study [119] has examined settlement-induced pre-damage effects on the seismic response of URM façades. However, in the study, both settlement and subsequent earthquake loading are applied exclusively in the IP direction, leaving the impact of IP-induced settlement on OOP behavior unaddressed.

Findings indicate that IP pre-damage and pre-deformation can reduce OOP strength and stiffness by up to 67%, primarily by forming cracking paths that act as failure planes during subsequent OOP loading. However, these effects only emerge after the walls surpass their peak IP strength and enter the inelastic response regime during pre-loading or pre-damaging before OOP loading. Furthermore, once a critical IP pre-damage or pre-deformation threshold is reached, corresponding to the complete formation of IP cracks, the interaction effects stabilize, and the walls retain residual OOP strength and stiffness [55].

The following subsections discuss the influence of different parameters on IP/OOP interaction effects in order of importance. Figure 5 classifies the numerical studies on IP/OOP interaction effects based on different properties. All specimens are constructed with solid clay (90%) or calcium silicate (10% in ref. [67]) bricks and cement-based mortar with different ratios of lime binder, and the studies under different loading scenarios do not systematically explore the effect of material properties. Similarly, the role of vertical pre-compression is only investigated in ref. [62], with no consistent trends observed. Moreover, all specimens are studied with surface pressure simulating airbag load used as the OOP loading apparatus, and top displacement used for all IP loadings. These assumptions prevent the analysis of variations in vertical load, loading apparatus, and material properties on IP/OOP interaction effects. Hence, the attention in the following subsections is primarily given to the influence of loading methodology and geometrical properties.

Loading Scenario, Methodology, and Boundary Conditions

The distribution of loading scenarios used in numerical studies on IP/OOP interactions is shown in Figure 5J. Similar to OOP/IP studies, the CB scenario is the most common, with 30 specimens (60%) subjected to IP pre-deformation before OOP loading [60,67,70]. Additionally, 12 walls (24%) [55] undergo SC loading, where IP and OOP loads are alternated stepwise to simulate the progressive effects of incremental IP damage. Finally, SQ loading is adopted in eight specimens (16%) [60,67] for pre-damaging the walls in the IP direction before applying the OOP load.

The boundary conditions assumed for IP and OOP loading are shown in Figure 5A,B, respectively. In CB simulations, 28 specimens experience IP cantilever (Figure 3A) pre-deformation, coupled with one-way bending beam-like OOP boundary conditions (Figure 3F) in one case [60] and two-way bending with no lateral confinement and free side and top rotations (Figure 3L) in 27 cases [70]. Only two CB specimens in ref. [67] incorporate IP double-clamped conditions (Figure 3B) with two-way bending OOP load and free side-edge rotations (Figure 3N). In SQ simulations, IP pre-damaging is applied under cantilever boundary conditions (Figure 3A) in one specimen [60], under double-clamped conditions (Figure 3B) in three [67], and under double-clamped conditions with restricted top uplift in four [60]. The OOP loading configurations for these SQ specimens vary. The one specimen in ref. [60] is subjected to one-way bending beam-like (Figure 3F) OOP loading, the three in ref. [67] experience two-way bending with free side-edge rotations (Figure 3N), and the last four in ref. [60] undergo one-way bending double-clamped OOP loading with restricted top uplift (Figure 3G). Finally, the 12 SC specimens [55] are tested with double-clamped IP loading (Figure 3B) and one-way bending beam-like OOP (Figure 3F) conditions.

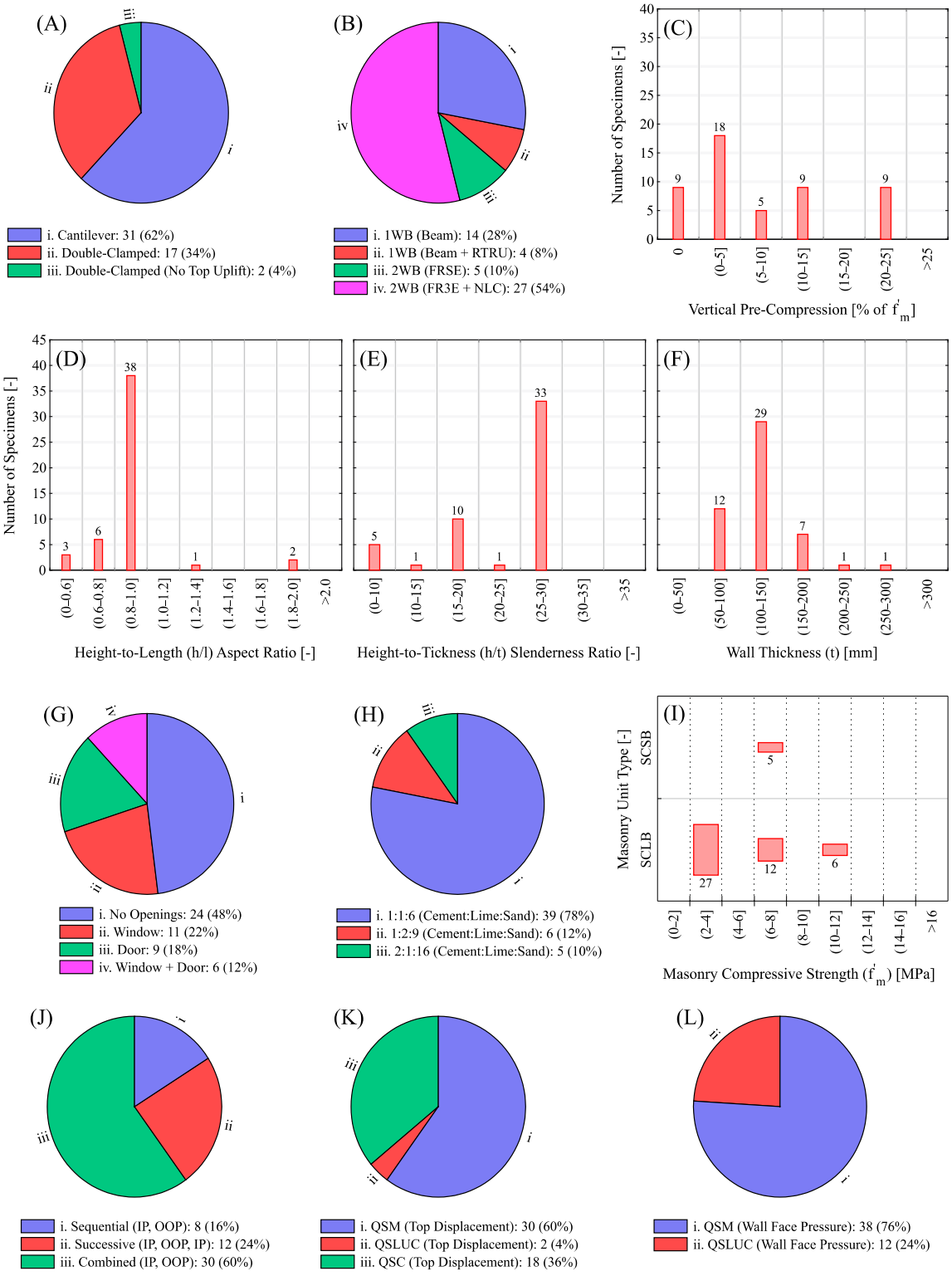

Figure 5. Overview of numerical studies focusing on the effects of IP response on the OOP behavior (IP/OOP interaction) in non-framed unreinforced masonry walls: classification of the specimens based on IP (**A**) and OOP (**B**) boundary conditions, amount of vertical pre-compression (**C**), aspect ratio (**D**), slenderness ratio (**E**), thickness (**F**), type of openings (**G**), mortar mixture (**H**), compressive strength of masonry (**I**), loading scenario (**J**), and IP (**K**) and OOP (**L**) loading procedure and apparatus. For the meaning of abbreviations, please refer to the Nomenclature section.

The loading procedures adopted in IP and OOP directions are shown in Figure 5K,L. The IP pre-deformation is applied using QSM loading in all CB studies [60,67,70]. In

contrast, the 12 SC simulations [55] and the IP pre-damaging in 6 SQ cases [60,67] employ QSC loading. Only two SQ specimens in ref. [60] undergo quasi-static load-unload cycles (QSLUC) of IP loading. In the OOP direction, all specimens are loaded with QSM, except for the 12 SC walls in ref. [55], where QSLUC is used to facilitate the alternating sequence of IP and OOP loading steps. The influence of loading scenarios, boundary conditions, and loading procedures on IP/OOP interactions is discussed in the following.

- Loading Scenario

The comparative effects of SQ and CB loading scenarios are investigated in [60], where two identical square walls (h/l = 1.0, h/t = 10) with cantilever IP boundary conditions (Figure 3A) are subjected to different cantilever IP loading histories before OOP testing in a one-way bending beam-like configuration. The SQ wall, subjected to IP pre-damage, exhibits no reduction in OOP strength. In contrast, the CB wall, with a 0.15% IP drift pre-deformation, experiences a 26% decrease in OOP strength, a 40% drop in OOP stiffness, and a 192% increase in ultimate OOP deformation. This discrepancy is attributed to residual torsion in the CB wall, which prevents both its toes from contributing equally to OOP resistance. As a result, further torsional effects and base detachment occur during OOP loading. Meanwhile, the SQ wall goes back to its initial state at the end of the pre-damaging step. A similar study reported in ref. [67] examines two squat slender (h/l = 0.7, h/t = 27) walls under double-clamped IP boundary conditions (Figure 3B) and OOP two-way bending with free side rotations (Figure 3N), one subjected to SQ loading and the other to CB loading. Both walls show comparable IP/OOP interaction effects up to an IP drift of 0.14%. However, at 0.2% drift, the CB wall completely loses its OOP strength due to excessive mixed IP and OOP deformations, whereas the SQ wall retains 40% of its OOP capacity. The presence of openings slightly alters these behaviors, as observed in ref. [67], where a CB and a SQ wall with window openings show similar OOP degradation to their solid counterparts, but with only a 10% higher strength reduction at 0.14% IP drift, possibly due to stress redistribution around the opening.

Regarding SC loading, a relatively squat wall reported in ref. [55] (h/l = 0.84, h/t = 10) exhibits even greater performance degradation than the CB wall in ref. [60], with a 67% reduction in OOP strength at 0.22% IP pre-damage drift. This severe loss is likely due to cumulative damage from multiple alternating IP and OOP loading cycles. However, the influence of IP boundary conditions must be considered, as this wall is loaded under a double-clamped IP configuration (Figure 3B), which introduces mid-height cracks that may reopen during its one-way bending beam-like OOP loading (Figure 3F), amplifying IP/OOP interactions. Additionally, the use of QSC IP loading in ref. [55], as opposed to the QSM procedure in [60], may have caused greater damage (see Section 4.1.2).

Concerning SM loading, the study conducted in ref. [59] suggests that IP deformation concurrent with OOP loading (with a 1:50 ratio to OOP load) significantly enhances OOP performance, increasing the total strength by 380% and peak deformation by 1700% due to improved wall stability as a result of the IP diagonal compressive strut adding to the vertical arching effect during OOP deformation. Further increasing the IP load proportion (1:10 to 1:4) shifts the failure mode toward IP deformation, increasing total strength by 500%.

- Boundary Conditions

As observed for the OOP/IP interaction, the extent of IP/OOP interaction effects is strongly influenced by the adopted IP and OOP boundary conditions, particularly whether the damage induced during IP pre-loading or pre-deformation aligns with the failure mechanisms of the subsequent OOP loading step.

In the CB scenario, a wall subjected to OOP loading with one-way bending beam-like (Figure 3F) boundary conditions [60] experiences a 30% reduction in OOP strength at a cantilever IP (Figure 3A) pre-damage level corresponding to 0.2% drift. This limited reduction occurs because the OOP deformation mode is only marginally affected by the base crack developed during IP loading. Even lower sensitivity is observed in a wall with OOP two-way bending (Figure 3N) and IP cantilever (Figure 3A) conditions [70], which shows only a 15% average strength drop at the same pre-damage level across different pre-compression levels, as its diagonal OOP crack pattern does not align with the primary base crack from IP loading.

More pronounced effects of boundary conditions emerge when comparing SQ specimens. The one-way bending beam-like OOP (Figure 3F) response of a square SQ wall ($h/l = 1.0$, $h/t = 10$) described in ref. [60] remains virtually unaffected, even at the highest cantilever IP (Figure 3A) pre-damage levels (up to 0.45% drift), as the IP cracks localize at the base but its subsequent OOP cracks concentrate at the mid-height mortar joint. However, when the same SQ wall is subjected to uplift-restricted double-clamped IP loading (Figure 3C) and one-way bending beam-like OOP (Figure 3G) deformation, it exhibits a 56% reduction in OOP strength and a 41% drop in deformation capacity at peak resistance for the same IP pre-damage level. This significant decrease is attributed to the dominance of shear deformation in the second case, where cracks propagate throughout the surface and intersect those formed during the IP shear failure. Similarly, double-clamped IP (Figure 3B) walls ($h/l = 0.67$, $h/t = 27$) subjected to OOP two-way bending with free side rotation (Figure 3N) [67] show considerable sensitivity, losing nearly 50% of their OOP capacity at a 0.2% IP drift pre-damage level. However, this severe degradation may be exacerbated by the large slenderness of these walls or the use of QSC pre-damage.

- Loading Procedure

The comparison between IP/OOP interactions under QSLUC and QSC IP double-clamped pre-damage is presented in ref. [60], where three similar walls are simulated, two subjected to QSLUC pre-damage where they are pushed to the target IP drift and returned to their initial position without being loaded in the opposite direction, and one subjected to full QSC cycles. The results show that QSLUC walls experience 35% and 24% lower reductions in OOP strength and peak deformation, respectively, compared to their QSC counterpart at equivalent pre-damage levels. This difference arises from the distinct damage distributions in the two cases. In QSLUC loading, crushing is concentrated only at two opposite corners of the wall, whereas in QSC loading, all corners undergo damage due to the repeated reversals of the applied load. Additionally, the diagonal strut formed in QSLUC pre-damaged walls provides a confining effect, mitigating OOP strength loss, whereas this stabilizing influence decreases in QSC pre-damaged walls due to the more widespread cracking and deterioration of the masonry.

Geometry

The distributions of aspect ratios (h/l), slenderness ratios (h/t), and thicknesses of numerical specimens are shown in Figure 5D–F, respectively. Similar to OOP/IP interactions studies, most IP/OOP interaction simulations focus on close-to-square walls ($0.8 < h/l \leq 1.0$), while extremely large slenderness ratios ($h/t > 30$) remain unrepresented, and very thin ($t < 50$ mm) and thick ($t > 200$ mm) specimens are scarce.

The influence of geometry on IP/OOP interaction effects depends on the adopted boundary conditions and loading scenarios. Among the SC simulations reported in ref. [55], six walls with similar slenderness ratios ($h/t = 16$) and aspect ratios ranging from 0.75 to 3.0 undergo double-clamped IP (Figure 3B) pre-damage, followed by one-way bending beam-like OOP (Figure 3F) loading. While the onset of OOP strength degradation and

the residual capacity are similar across all walls, the rate of strength reduction is higher in squat walls (h/l < 1.0). For instance, at 0.15% IP pre-damage drift, the tallest wall (h/l = 0.75) retains 95% of its OOP strength, whereas the squat wall (h/l = 0.34) reaches its residual capacity with a 62% reduction. This suggests that squat walls are more sensitive to crushing due to the formation of diagonal compressive struts during IP loading. In the same study, six additional walls with similar aspect ratios (h/l = 0.84) but varying slenderness ratios (h/t = 10–30) show minimal differences in the rate and magnitude of OOP strength reduction. The absence of vertical arching effects, attributed to low pre-compression (3% of f'_m) and unrestricted uplift at the top likely explains this behavior. Under these conditions, residual OOP strength and the initiation of OOP degradation appear independent of wall geometry. In contrast, ref. [60] reports one square (h/l = 1.0, h/t = 10) and one tall (h/l = 2.0, h/t = 20) wall under fixed-uplift double-clamped IP (Figure 3C) pre-damage and one-way bending OOP (Figure 3G) loading, where the tallest wall exhibits a 15% lower residual OOP strength and an 80% greater stiffness reduction. This disparity is attributed to severe crushing failures at the toes and base of the tall wall during its flexural movement in the pre-damaging phase, as well as large OOP confinement due to the fixity of the uplift, while the squat wall primarily develops shear cracks less affected by such phenomena.

Presence of Openings

Unlike studies on OOP/IP interaction effects, walls with openings are more frequently represented in IP/OOP investigations, as illustrated in Figure 5G. Specifically, ref. [70] simulates nine walls with window openings, nine with door openings, and six with combined window and door openings under CB loading, incorporating different levels of vertical pre-compression. Two window and door sizes are examined in the first 18 walls, with windows occupying between 8% and 21% of the wall surface and doors covering 19% to 30%. The remaining six walls feature both doors and windows, collectively accounting for 25% of the surface area. Additionally, walls with smaller windows and doors are analyzed in both symmetric and asymmetric configurations. Another two walls with asymmetric windows (26% of the surface area) are considered in ref. [67], one subjected to CB loading and the other one to SQ loading.

The walls in [67] exhibit significantly lower sensitivity to IP/OOP interactions than their counterparts without opening, maintaining 25% and 85% higher OOP strength under similar IP pre-damage and pre-deformation, respectively. While this reduced sensitivity may be attributed to the diminished lateral and vertical arching effects in walls with an opening, it could also result from the low pre-compression levels applied at the top boundary (8% of f'_m in IP loading and 0.8% in OOP loading). In contrast, ref. [70] finds that walls with openings generally exhibit similar IP/OOP interaction effects to walls without openings, except for those featuring both window and door openings or large openings under high pre-compression (12% of f'_m). In these cases, the large openings cause stress concentrations and excessive crushing at the corners of piers and spandrels, leading to up to 30% greater OOP strength reduction compared to solid walls (i.e., walls without openings). The solid walls in ref. [70] do not exhibit such sensitivity to vertical load, as they lack these localized stress concentrations. Furthermore, in walls subjected to high pre-compression, openings disrupt the diagonal compressive struts formed during IP pre-deformation, further reducing OOP strength relative to their counterparts without openings. All specimens, regardless of the presence of openings or pre-compression, experience ultimate OOP strength drops of up to 20%, except for one wall with a combined window and door opening, which undergoes a 40% reduction. This higher degradation occurs because the top edges of the wall and window align at the same elevation, facilitating cracking at the bottom and top of the pier between them during IP loading, thereby

accelerating its OOP collapse. These findings further underscore the significance of opening size and configuration in determining the extent of IP/OOP interaction effects.

4.2. Indirect Interactions: Flange Effects

This section reviews numerical and experimental studies investigating the influence of flanges on the IP and OOP response of non-framed URM walls, as well as their behavior under direct IP-OOP interactions. Given the greater availability of data, the review begins with studies on the Flange effects on the IP response of main walls (F/IP interaction) in Section 4.2.1. Next, research on the Flange effects on the OOP response of main walls (F/OOP interaction) is explored in Section 4.2.2. Lastly, the findings of numerical studies on the flange influence on the response under direct IP-OOP interaction effects (F/IP-OOP interaction) are discussed in Section 4.2.3.

4.2.1. Flange Effects on the IP Response of Main Walls (F/IP Interaction Effects)

This section reviews the 14 experimental tests [77–79,81,83,113] and 737 numerical simulations [70,76,87–93] investigating F/IP interaction effects. The extent of F/IP interaction effects ranges from negligible to highly significant, depending on factors such as the boundary conditions, vertical pre-compression, flange configuration and size, and the geometric characteristics of the main panel. Figure 6 visualizes how the addition of flanges changes the IP behavior under different boundary conditions. Overall, the presence of flanges increases IP strength and stiffness by introducing additional vertical constraints and altering flexural failure mechanisms into shear-dominated ones, especially in cantilever walls (Figure 6A), as well as increasing the effective cross-section of double-clamped walls (Figure 6B). This might also introduce a detrimental effect, as the change in failure mechanism typically comes with a reduction in wall ductility. The impact of flanges is most pronounced in cantilever and square-to-tall walls, where the reference non-flanged walls exhibit flexural failure. Among different configurations, walls featuring flanges on both sides and ends (⌶ walls) demonstrate the highest increase in IP stiffness and peak shear capacity. While longer flanges provide greater strength or stiffness increments, their influence reaches a threshold beyond which further length increases yield no additional change. The following subsections analyze the effects of each of these parameters, illustrated for numerical specimens in Figure 7, on F/IP interaction effects.

Boundary Conditions

The classification of numerical simulations on F/IP interaction based on IP boundary conditions is shown in Figure 7A. The majority of studies, specifically 28% and 32%, assume double-clamped conditions with free and restrained top uplift, respectively. Another 24% [70,76,87–89,92] adopt cantilever configurations, while the remaining 16% [88,89] use a semi-cantilever setup, where the load application point (zero-moment location) is positioned at 75% of the wall height instead of 50% (double-clamped) or 100% (cantilever) [19].

The sensitivity of ⌶ walls to different boundary conditions is extensively analyzed in refs. [88,89]. In double-clamped walls, F/IP interaction effects remain limited to maximum variations in the range of 20%, except when the pre-compression level is lowered (from 30% f'_m to 15%). In such cases, the non-flange variants of tall walls (h/l = 2.0) experience rocking, while non-flanged square (h/l = 1.0) and squat walls (h/l = 0.6) undergo toe crushing due to flexural deformation. Flanges mitigate these effects by introducing additional axial constraints that eliminate rocking in the former and increasing the effective cross-section to reduce crushing in the latter two. As a result, IP strength increases by up to 50% across all aspect ratios, while stiffness increases by 11% in squat walls and 60% in tall walls. The effect of flanges is even more pronounced in cantilever walls. Under the lowest pre-compression (15% of f'_m), tall walls exhibit up to 175% greater IP strength and

375% higher stiffness compared to their non-flanged counterparts. Square walls also show substantial gains, with a 150% increase in strength and a 115% rise in stiffness, whereas squat walls display improvements similar to those observed in double-clamped cases, likely due to their comparable failure mechanisms. Semi-cantilever walls behave similarly to double-clamped walls, as their primary failure mode is shear. These trends are corroborated by numerical findings in refs. [87,90,93].

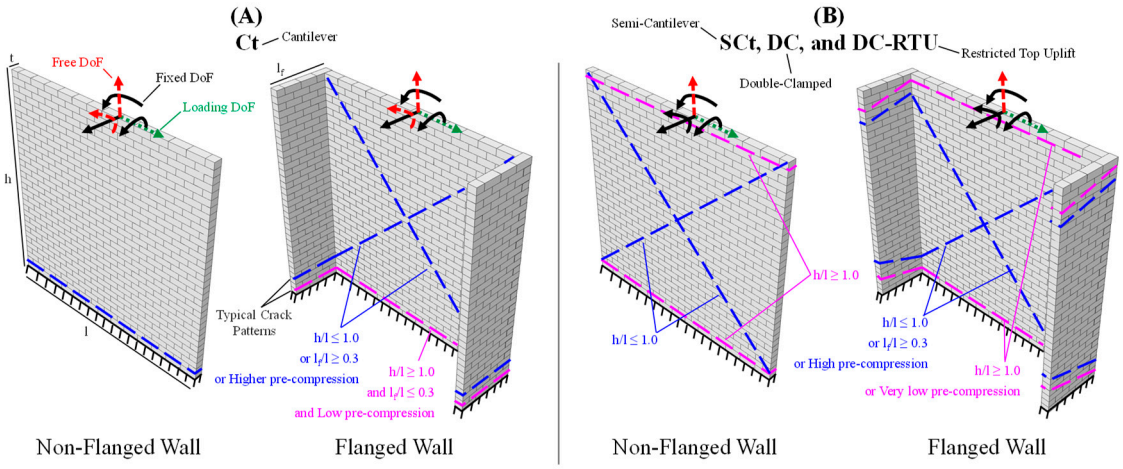

Figure 6. Visualization of the F/IP interaction effects on the IP failure mechanism of non-framed unreinforced masonry walls, based on the available data. The Ct (**A**) or SCt, DC, and DC-RTU (**B**) boundary conditions are used. Typical crack patterns associated with failure mode under each boundary condition are shown with dashed blue or pink lines. The abbreviation "DoF" stands for degree of freedom. Fixed, free, and loaded DoFs are shown with solid black, dashed red, and dotted green arrows, respectively. For the meaning of other abbreviations, please refer to the Nomenclature section.

Experimental findings also align with numerical simulations. Double-clamped tests in [77,79,81,83] confirm modest IP strength and stiffness increases of 20% and 6%, respectively, while cantilever specimens in ref. [78] exhibit strength gains of up to 33%. The relatively lower strength enhancement in experimental walls, despite the similar pre-compression levels to numerical studies (5.3% in double-clamped and 20% in cantilever), is attributed to the use of shorter flanges (10–30% of wall length) in testing.

Vertical Pre-Compression

The range of vertical load magnitudes adopted in each study, expressed as a percentage of f'_m, is shown in Figure 7B. Except for 12 instances (2%) in refs. [70,76], all studies apply at least a minimal vertical load (1.25% of f'_m) at the top of the walls. However, while 18% distribute the pre-compression to both the flanges and the main panel, the remaining 80% [88–91] apply it solely to the main panel. Experimental studies generally load both components, except for six tests in refs. [77,79], where only the main panel is pre-compressed. The influence of vertical pre-compression on F/IP interaction effects varies significantly depending on the boundary conditions, as shown by numerical sensitivity studies on ⌶ walls in refs. [76,88–90,93].

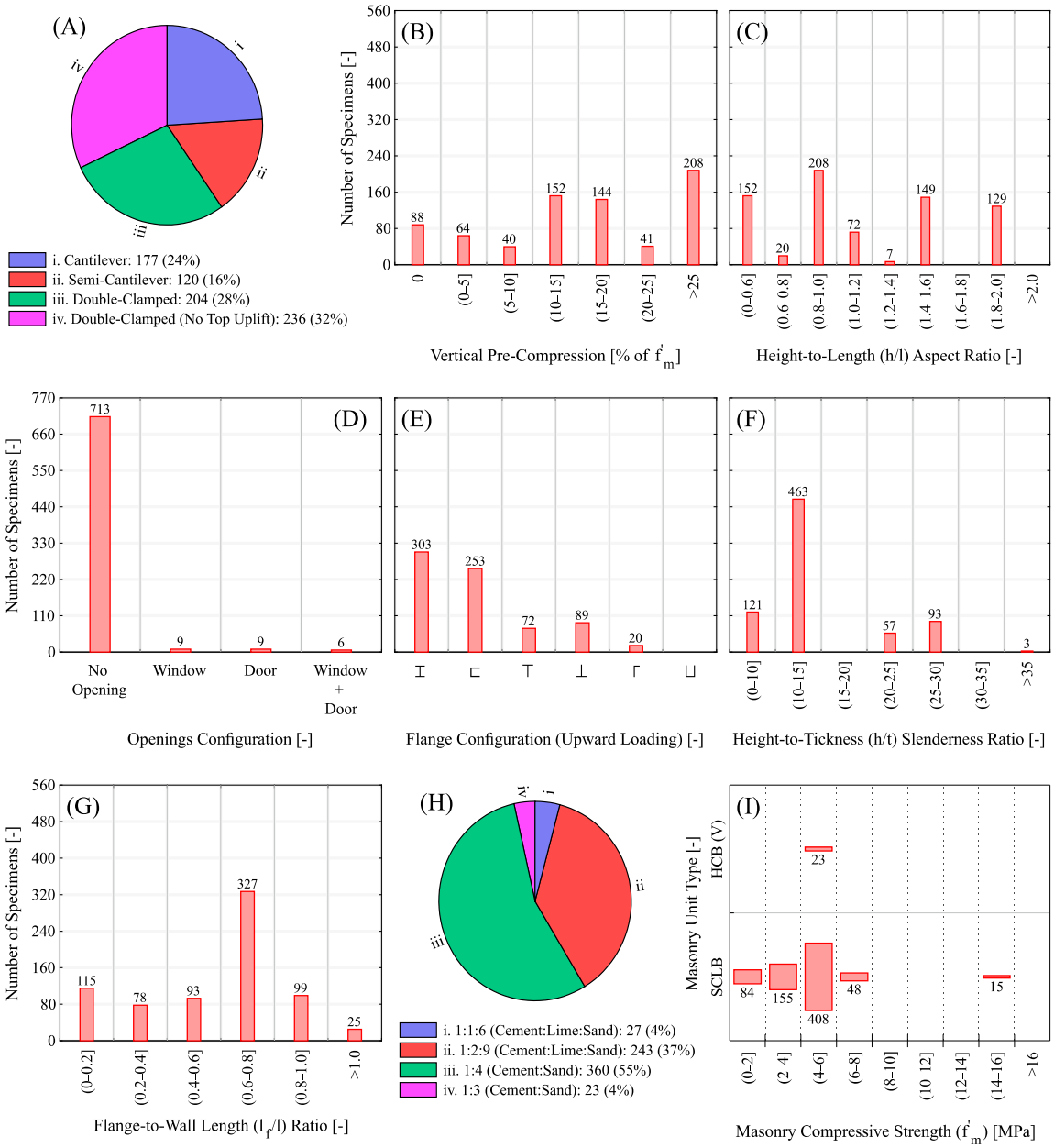

Figure 7. Overview of numerical studies focusing on the effects of flanges on the IP behavior (F/IP interaction) in non-framed unreinforced masonry walls: classification of the specimens based on IP boundary conditions (**A**), amount of vertical pre-compression (**B**), aspect ratio (**C**), type of openings (**D**), flange configuration planar view (**E**), slenderness ratio (**F**), flange size (**G**), mortar mixture (**H**), and compressive strength of masonry (**I**).

In double-clamped walls, the narrow range of low pre-compression levels (1.8–7.3% of f'_m) in ref. [93] shows no effect on F/IP interaction. However, refs. [88,89] suggest that a moderate increase in pre-compression (15–30% of f'_m) leads to a reduction in the strengthening effects of flanges. Walls under 15% pre-compression exhibit, on average, 30% higher IP strength and 50% greater IP stiffness gains compared to those under 30%, as they remain more susceptible to flexural deformation, which flanges effectively constrain.

For uplift-restrained double-clamped walls, ref. [90] presents an inverse trend in F/IP interaction across vertical load from 1.25% to 100% of f'_m. While squat (h/l = 0.5) and square ⌶ walls remain largely unaffected, tall walls (h/l = 2.0) under 100% (of f'_m) vertical load exhibits a 90% IP strength increase after the addition of flanges, whereas those pre-

compressed by 12.5% of f'_m experience no enhancement. It is likely that since ref. [90] applies pre-compression exclusively to the main panel, large vertical loads lead to excessive crushing at the toes of the walls. The addition of flanges, covering up to 66% of the panel length, mitigates this effect by increasing the effective cross-section and redistributing compressive stresses, although at low pre-compressions, such improvements are absent. However, the observed increase in IP response may not occur in the real world, as the magnitude of the vertical load used in ref. [90] is unrealistically high and not representative of real scenarios. It should be noted that tall flanged walls under very low vertical load (1.25% of f'_m) show a 30% lower IP strength than their non-flanged counterparts. According to ref. [90], the flanges in this case alter the failure mode from rocking to shear sliding at the bed joints, which exhibits lower resistance than rocking under low pre-compression.

In cantilever boundary conditions, only the sensitivity studies of refs. [76,88,89] are available and show considerable sensitivity to vertical pre-compression in ⌶ walls. The former, conducted on square walls under moderate pre-compression levels (15–30% of f'_m) shows that less-compressed (15% of f'_m) variants of all aspect ratios demonstrate almost 100% higher IP strength increase than higher-compressed (30% of f'_m) specimens when flanges are included. As the most affected specimens, the less-compressed tall wall (h/l = 2.0) shows as much as 200% IP strength increase due to the presence of flanges, because of the elimination of any rocking behaviors and lowering the susceptibility to crushing. The flanged walls of ref. [76] show lower sensitivity to the considered pre-compression levels (0–12.5% of f'_m). The two walls with vertical pre-compression show a similar 40% increase in IP strength with the inclusion of flanges, while the gain increases to 150% in the non-compressed wall. The lower sensitivity of these specimens can be attributed to the high slenderness of their flanges (27.3 compared to 13.9 in refs. [88,89]), which directly influences the extent of F/IP interaction effects.

Main Panel Configuration and Geometry

The classification of numerical specimens based on the aspect ratios of the main panel and the presence of openings is shown in Figure 7C,D, respectively. The studies encompass a wide range of geometries, from tall (h/l = 2.0) to squat (h/l = 0.5) walls. However, the majority of simulations are performed on solid walls (without opening), except for 24 specimens in ref. [70] (3% of all data), which serve as the flanged counterparts of walls described in Section 4.1.2. Experimental studies on openings are also scarcer, with only two walls tested in ref. [83], each containing a symmetrical window, but without direct comparison to variations without opening. All numerical walls and 6 of the 14 tested specimens are single-wythe, while the remaining eight tested specimens [79,83] are double-wythe. Since these double-wythe walls exhibit similar behaviors to the single-wythe counterparts, no further investigation of the influence of the number of wythes on F/IP interaction effects is conducted.

The effects of aspect ratio are implicitly discussed in relation to boundary conditions and vertical pre-compression in previous sections. A summary is reiterated here. Double-clamped ⌶ walls across all aspect ratios demonstrate similar F/IP interactions under moderate pre-compression (15–30% of f'_m) and almost no sensitivity to aspect ratio [88,89]. Only in the fixed-uplift scenario of ref. [90] do some variations appear. Square and tall (h/l = 1.43 and 2.0), low-compressed walls (1.25% of f'_m) experience a 35% reduction in IP strength due to flanges, as their failure mode shifts from rocking to a less-resistant bed-joint sliding. In contrast, high-compressed tall walls (50–100% of f'_m) show 190% higher increase in IP strength compared to square walls, as flanges eliminate crushing failures by increasing the effective cross-section. In cantilever walls, F/IP interaction effects increase considerably from squat (h/l = 0.5–0.6) to tall (h/l = 1.4–2.0) ⌶ walls, irrespective

of pre-compression levels (0–30% of f'_m). However, the influence of flanges diminishes with increasing pre-compression. For example, non-compressed squat (h/l = 0.6) and tall (h/l = 1.4) flanged walls show 50% and 150% higher IP strength than their non-flanged references. In contrast, their 30%-compressed counterparts exhibit only (and similar) 40% and 60% strength increases, respectively.

The walls with opening simulated in ref. [70] are analyzed both as non-flanged and as ⌶ flanged variants with flange lengths equal to 18% of the wall length on each side. When averaging results across different pre-compression levels, opening walls exhibit varying reductions in F/IP interaction, with no clear trend based solely on opening size. For instance, specimens with a combined window and door opening (24% of the wall area) show a 46% lower IP strength increase, while a larger single symmetric door opening (30% of the wall area) leads to only a 25% reduction in IP strength gain. Likewise, a small symmetric window (7.7% of the wall area) results in a 35% decrease in F/IP interaction, whereas a larger symmetric door (19% of the wall area) leads to just a 22% reduction. However, a clearer pattern emerges regarding the configuration of openings, with the addition of flanges to walls with the asymmetric door (19% of the wall area) or window (7.7% of the wall area) leading to 20% higher IP strength improvement than their symmetric counterparts. This difference may stem from the monotonic loading protocol adopted in the study, which subjects the walls to IP forces in only one direction. It is possible that loading in the opposite direction would yield different F/IP interactions, and cyclic loading would lead to similar F/IP interaction effects in symmetric and asymmetric walls.

Overall, the findings suggest that the configuration of openings has a greater impact on F/IP interaction effects than their size. Openings influence F/IP response by increasing susceptibility to flexural deformation and localized crushing at pier corners. Both effects depend not only on the opening size but also on its placement. For example, the small window (7.7% of the wall area) introduces four stress concentration points, decreasing F/IP interaction due to crushing, which is independent of the presence of flanges. In contrast, the larger door opening (19% of the wall area) primarily amplifies rocking behavior and introduces only two stress concentration points, resulting in less reduction of F/IP interaction effects. Walls with larger windows and doors do not exhibit additional decreases in F/IP interaction, as the stress concentrations remain comparable to those of smaller openings. However, in walls with combined window and door openings (25% of the wall area), a larger reduction in F/IP interaction is observed, particularly when the top edge of the window aligns with the top of the door. This alignment facilitates easier rocking of the pier between the openings, further diminishing the influence of flanges.

Flange Configuration and Geometry

The classification of numerical specimens based on different flange configurations, flange slenderness ratios, and flange lengths is shown in Figure 7E–G, respectively. The majority of numerical studies (41%) focus on ⌶ walls, where flanges are symmetrically attached at both ends and on both sides of the main panel. Another significant portion (34%) considers ⊏ walls, which are asymmetric relative to the main wall panel, with flanges positioned at both ends but only on one side. Additionally, 19% of the simulations examine walls asymmetric with respect to the length axis of the main wall, with flanges attached at both sides but at only one wall end. In these cases, simulated under unidirectional IP load, the flanges are either positioned at the end in compression (10%), forming a ⊤ configuration under upward loading, or at the end in tension (12%), creating a ⊥ configuration. Lastly, ⌈ walls, which exhibit asymmetry in both planar axes, are also investigated (3%), with one flange positioned at the compressed end on one side of the wall. Flange sizes range from

20% to 100% of the main wall length per side. Finally, the majority of studies focus on thick flanges (h/t < 15), with slender configurations explored in only 20% of the simulations.

The influence of flange configuration has been explored in studies across various wall geometries and pre-compression levels [70,76,88–90,93], with all studies agreeing that ⌶ walls exhibit the highest F/IP interaction effects. These configurations increase IP strength by 50% in double-clamped walls [88,89] and by as much as 220% in cantilever walls [70], as they effectively eliminate rocking at the tensile end of the walls and mitigate crushing at compressed ends. The ⊏ configuration is the second most effective, improving IP response by 20% [88,89] to 100% [76]. However, its asymmetric nature introduces torsional effects [79,90], which in some cases can reduce IP strength compared to non-flanged walls [81]. These torsional effects arise due to the application of IP load at the top of the main panel rather than at the geometric center of the flanged wall cross-section, reproducing the actual load application in real-world flanged walls. Among the ⊤ and ⊥ configurations, numerical studies [90,120] and experiments [79] show ⊥ to be more effective. This is because the ⊤ configuration primarily reduces the crushing of the compressed toe of the wall. The ⊥ configuration, on the other hand, prevents rocking, which is the primary failure mechanism in non-flanged walls, and, in return, also delays crushing as effectively as the ⊤ configuration. In most cases, ⊥ performs similarly to ⊏ [93] or slightly less effectively [90]. Finally, the ⌈ configuration is found to have almost no impact, showing behavior similar to non-flanged walls [93].

Regarding the effectiveness of different flange sizes, studies [87–89,91,92] confirm that larger flanges generally provide greater improvements in IP strength and stiffness. However, depending on boundary conditions, a threshold exists beyond which further increases in flange length yield minimal additional benefits. Under double-clamped conditions, ⌶ and ⊏ walls demonstrate most of their improvement due to F/IP interaction effects with flange lengths reaching 30% of the main wall length [88,89]. The longer-flange variations (60–100% of wall length), as well as the specimens analyzed in ref. [87] with flange lengths from 36% to 120%, show negligible additional improvements. The only exception is the ⊥ configuration, which remains sensitive to flange length, showing significant improvements in IP strength and failure mechanisms at lengths as high as 70% of the main wall length [91]. In cantilever walls, the threshold extends to higher flange lengths, with F/IP interaction benefits continuing up to 100% of the main wall length [87–89,92]. Although flanges as small as 10% of wall length can already shift failure mechanisms from rocking to shear and double the IP strength [88,89], longer flanges (90% of wall length) further increase strength by an additional 100% relative to non-flanged walls, beyond which F/IP interactions stabilize. Once again, ref. [87] finds that ⊥ configurations exhibit an even higher threshold, requiring a flange length of up to 90% of the main wall length before altering failure mechanisms from flexure to shear.

The slenderness ratio of flanges also affects their OOP strength, influencing the extent of F/IP interaction effects. Double-clamped walls exhibit low sensitivity to such variations [90,93]. However, in cantilever walls, greater sensitivity is observed when comparing results from refs. [88,89] and [76] on square and tall (h/l = 1.4) walls with similar flange lengths (l_f/l = 10%) and vertical pre-compression (15% of f'_m). The former study considers thick flanges (h/t = 13.9), while the latter models slender flanges (h/t = 27.3). Consequently, in refs. [88,89], the addition of thick flanges improves IP strength by 85% in square walls and 116% in tall walls, whereas in ref. [76], the flanges increase IP strength by only 47% and 83%, respectively.

4.2.2. Flange Effects on the OOP Response of Main Walls (F/OOP Interaction Effects)

This section reviews experimental and numerical studies investigating F/OOP interaction effects. The F/OOP interaction effects have received significantly less attention in research compared to F/IP interaction effects. Although 30 experimental tests exist, 28 of them [80,82] focus on dry-joint specimens subjected to QSM base rotation, where the flanges remain unrestrained and are free to rock during the flexural OOP deformation of the main panel (similar to the example in Figure 8A). These tests primarily investigate the effectiveness of various flange and geometric configurations in altering the OOP collapse mechanism and enhancing the OOP resistance of the main panel. Only two experiments, conducted in refs. [84–86], explore F/OOP interactions in regular masonry under dynamic shake table loading, simulating one-way bending cantilever motion. However, these tests do not provide data on the strength degradation or damage patterns of the specimens, limiting their contribution to understanding F/OOP effects. On the numerical side, 42 simulations [70,76] examine two-way bending walls with free lateral confinement and unrestricted top-edge rotation, wherein the OOP movement of the flanges is constrained and the panels are subjected to QSM OOP surface pressure mimicking airbags. In these cases, the flanges, while acting as boundary elements for the main panel rather than directly resisting the OOP load, provide horizontal confinement that enhances arching effects and increases OOP strength and stiffness. They also restrain the rotation of lateral edges of the main panel before their cracking, leading to more complex two-way bending failure mechanisms (as illustrated in Figure 8B). Although the number of studies is limited, they provide valuable insights into the influence of flange configuration, wall geometry, openings, and vertical pre-compression on F/OOP interactions. The following subsections discuss the impact of different wall properties on F/OOP interaction effects, with Figure 9 presenting the classification of both experimental and numerical specimens based on these parameters.

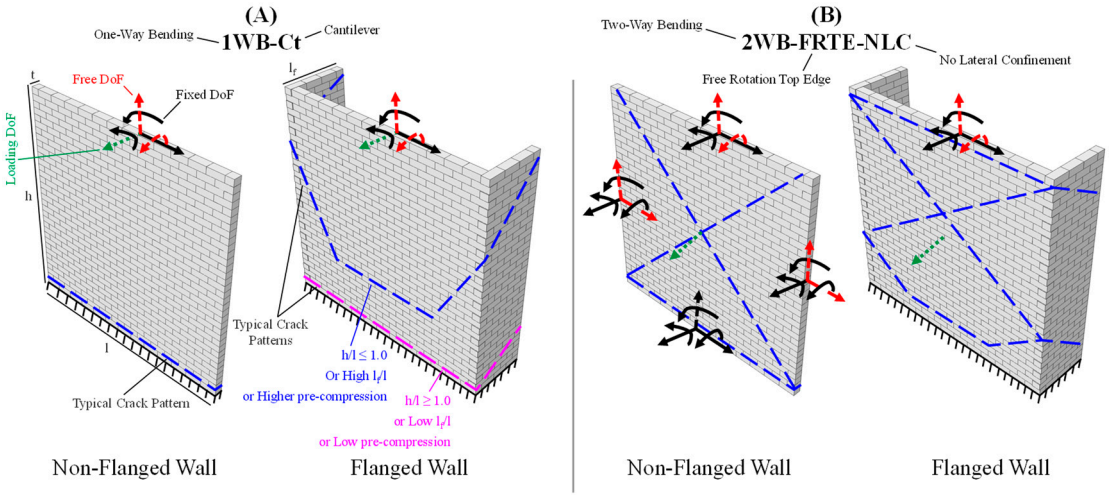

Figure 8. Visualization of the F/OOP interaction effects on the OOP failure mechanism of non-framed unreinforced masonry walls, based on the available data. The 1WB-Ct (**A**) or 2WB-FRTE-NLC (**B**) boundary conditions are used. Typical crack patterns associated with failure mode under each boundary condition are shown with dashed blue or pink lines. The abbreviation "DoF" stands for degree of freedom. Fixed, free, and loaded DoFs are shown with solid black, dashed red, and dotted green arrows, respectively. For the meaning of other abbreviations, please refer to the Nomenclature section.

Flange Configuration and Geometry

The distribution of flange configurations and flange-to-wall length ratios used in different numerical and experimental studies is shown in Figure 9F,G. The effects of flange length

on F/OOP interactions cannot be explicitly analyzed, as all numerical studies incorporate relatively short flanges (up to 18% of the wall length), and the experimental specimens with similar flange sizes vary significantly in geometry and aspect ratio, preventing direct comparisons. However, valuable insights can be derived regarding the influence of different flange configurations on OOP behavior.

Under one-way bending conditions, the 28 experiments in refs. [80,82] explore a diverse range of flange configurations. Among these, 10 specimens feature an ⌊⌋ arrangement, where the main panel is positioned at the tensile end under upward loading, while 6 adopt a ⊓ configuration with the panel at the compression end. Additionally, six specimens use the ⊤ setup, three employ the ⌈ layout, and another three investigate a ⌈⌉ configuration, which resembles ⊓ but incorporates an extra flange at the mid-length of the main panel. In terms of OOP resistance, the ⌈ walls demonstrate the weakest performance across all tested geometries, as their flanges fail to provide sufficient lateral restraint to the main panel. The ⊤ configuration shows notable improvements, particularly for squat (h/l = 0.63) and square walls, for which the OOP strength increases by 100% and 50%, respectively, compared to ⌈ walls. This increase arises because the central flange effectively divides the main panel into two smaller sub-panels, increasing their effective aspect ratio and providing additional OOP support. The ⊓ walls exhibit even greater improvements, with OOP strength increasing by an additional 40% on average compared to ⊤ walls, as the flange constraints alter the failure mode from one-way to two-way bending. Positioning the flanges on the tensile side of ⊓ walls appears less effective than those on the compressive side of ⌊⌋ walls. Notably, squat (h/l = 0.6) and square ⌊⌋ walls achieve similar or, in some cases, even 20% higher OOP resistance than their ⊓ counterparts, despite having half the flange length. The introduction of a third flange in the ⌈⌉ walls further increases OOP resistance, with the solid ⌈⌉ wall (total h/l = 0.53) demonstrating 37% greater strength than the squat ⌊⌋ wall (h/l = 0.6). However, this improvement is partially attributed to the ⌈⌉ configuration utilizing double the flange length compared to the ⌊⌋ wall (l_f/l of 0.7 vs. 0.3).

Under two-way bending boundary conditions, ref. [76] investigates ⊢⊣, ⌊⌋, and ⊢ walls under upward loading. The ⊢⊣ configuration demonstrates the highest F/OOP interaction effects, increasing OOP strength by an average of 63% across zero to moderate pre-compression levels (0–12.5% of f'_m). The ⌊⌋ walls show slightly lower strength improvements, averaging a 40% OOP strength increase. In contrast, the ⊢ configuration provides no significant enhancement in OOP resistance, as the single flange fails to adequately restrain the main panel and instead induces torsional effects, reducing its effectiveness.

Vertical Pre-Compression

The distribution of vertical pre-compression levels adopted in the numerical and experimental studies is shown in Figure 9B. Experimental works are primarily conducted with no pre-compression, preventing the study of the sensitivity of cantilever specimens to the variations of vertical load. On the other hand, the influence of vertical pre-compression on F/OOP interaction effects in two-way bending walls is examined in numerical studies [70,76], where ⊢⊣ specimens with [70] and without [76] openings are subjected to varying levels of pre-compression, ranging from zero to moderate values (up to 25% of f'_m). Both studies consistently demonstrate that increasing vertical load significantly reduces the enhancement in OOP capacity provided by flanges. For instance, in ref. [76], flanged solid walls under zero pre-compression exhibit up to 130% higher OOP strength than their non-flanged counterparts, whereas walls subjected to 12.5% pre-compression show only a 20% improvement. A similar trend is observed in ref. [70], where flanged walls with various opening configurations display an average 173% increase in OOP strength under zero pre-compression, which drops to just 33% under 25% pre-compression. Similar

trends are also noted for ⌊⌋ and ⊢ walls in ref. [76]. Although the complete deformation patterns of the specimens are not fully detailed in the publications, it is inferred that vertical pre-compression plays a more dominant role in enhancing OOP strength than the presence of flanges. In other words, even the lowest pre-compression levels considered in refs. [70,76] (6.25% of f'_m) appear to induce substantial vertical confinement effects, making the additional contribution of flanges secondary.

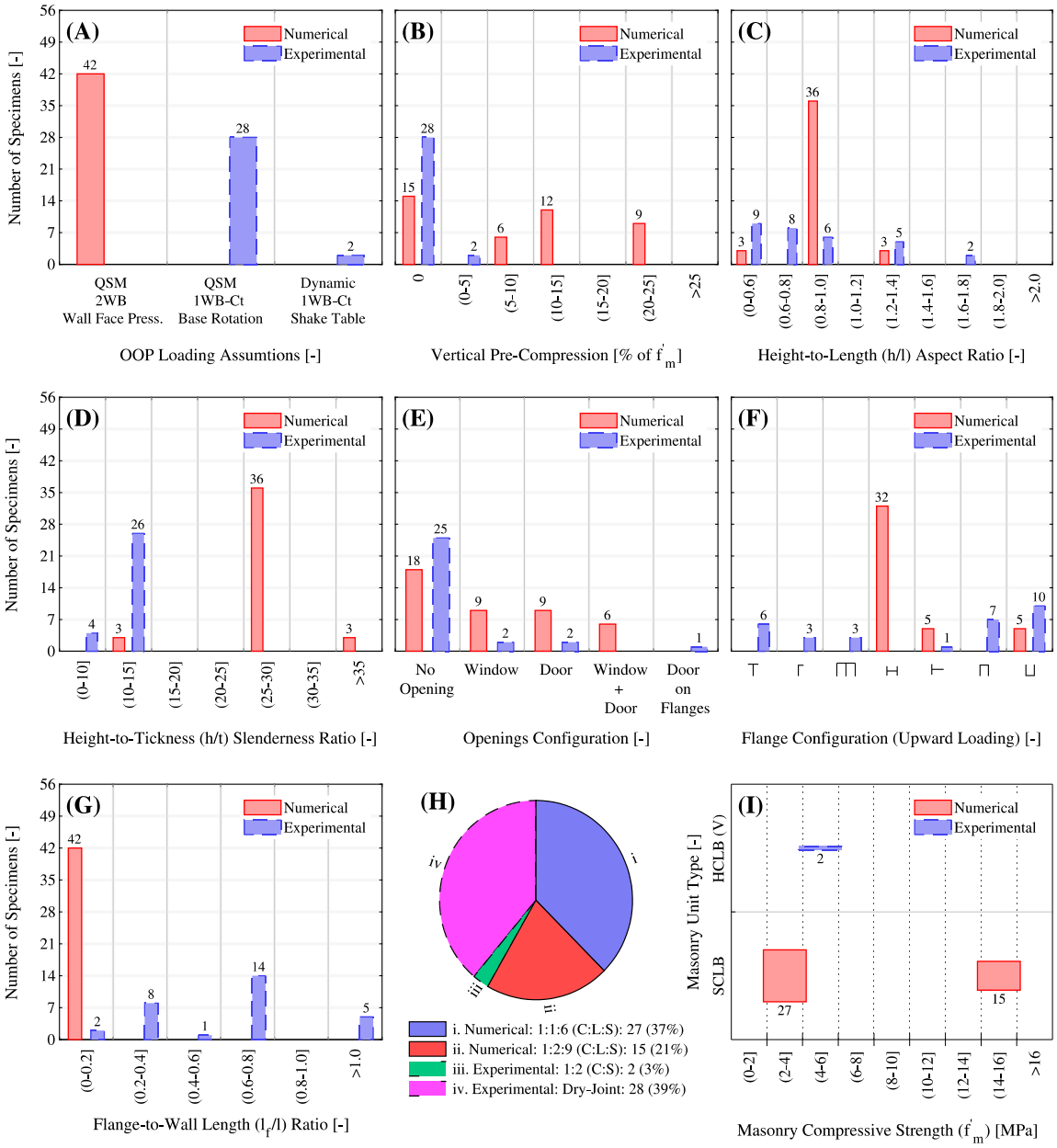

Figure 9. Overview of experimental and numerical studies focusing on the effects of flanges on the OOP behavior (F/OOP interaction) in non-framed unreinforced masonry walls: classification of the specimens based on OOP loading assumptions (**A**), amount of vertical pre-compression (**B**), aspect ratio (**C**), slenderness ratio (**D**), type of openings (**E**), flange configuration planar view (**F**) and size (**G**), mortar mixture (**H**), and compressive strength of masonry (**I**). For the meaning of abbreviations, please refer to the Nomenclature section.

Main Panel Geometry

The distribution of aspect ratios, slenderness ratios, and opening configurations adopted in numerical and experimental studies is shown in Figure 9C–E, respectively.

In the experiments reported in refs. [80,82], various aspect ratios (h/l) are considered for cantilever walls, ranging from 0.5 in squat walls to 1.25 in tall walls in [80], and from 0.3 to 1.0 in ref. [82]. Both studies consistently demonstrate that in higher aspect ratios, the increase of OOP strength due to F/OOP interaction is higher across different flange configurations compared to lower aspect ratios. For example, the semi-square ⊓ wall ($h/l = 0.9$, $l_f/l = 0.8$) in ref. [80] exhibits a 135% greater increase in OOP strength compared to a similarly sized squat wall ($h/l = 0.53$, $l_f/l = 0.7$). As expected, this is attributed to the larger length of the squat wall, which limits the ability of the flanges to constrain the main panel and provide horizontal confinement. As a result, the main panel freely overturns during OOP deformation without activating the two-way bending mechanism.

Numerical simulations in ref. [76] reveal a similar trend for two-way bending walls, albeit with two key differences compared to one-way bending cases. First, the distinction between square ($h/l = 1.0$) and squat ($h/l = 0.5$) walls is less pronounced, with square walls showing only a 60% greater OOP strength increase compared to squat walls when ⊢⊣ flanges are added. This reduced difference is likely due to the smaller flange size in the simulations compared to the experimental tests (14% vs. 70% of wall length). Second, while in one-way bending walls, higher aspect ratios continue to show bigger OOP strength increases, in two-way bending walls, the benefits of increasing aspect ratio plateau at square walls. Specifically, tall walls with $h/l = 1.4$ across various flange configurations show no additional OOP strength enhancement compared to square walls, likely because lateral IP motion of the side edges is allowed in the specimens of ref. [76]. Another reason for the higher effectiveness of flanges in one-way bending OOP responses could be their ability to alter the OOP collapse mechanism of these walls. In other words, the addition of flanges to 1WB walls, especially tall ones, significantly increases the OOP strength through changing the OOP deformation pattern to 2WB. Whereas the walls already with 2WB boundary conditions do not experience such a change, and hence, undergo lower changes after the addition of flanges compared to 1WB walls.

Regarding the effects of openings, the work reported in ref. [70] analyzes the same flanged walls introduced in Section 4.2.1 When the flanged walls are loaded in their OOP direction, it is found that opening size and configuration have no significant impact on F/OOP interactions, as the walls with opening exhibit nearly identical OOP strength improvements to solid walls after the addition of flanges.

4.2.3. Flange Influence on Response Under Direct IP-OOP Interaction Effects (F/IP-OOP Interaction)

The numerical studies [70,76,87] are reviewed in this section, as they examine the influence of flanges on direct IP-OOP interaction effects in non-framed URM walls. These studies apply the same loading scenarios used for investigating direct IP-OOP interactions to flanged walls and compare the results with their corresponding non-flanged counterparts. Specifically, ref. [76] analyzes the impact of flanges on the IP response when subjected to OOP pre-load, while ref. [70] evaluates the OOP response under IP pre-deformation (both using the CB loading scenario). Additionally, ref. [87] investigates the bidirectional behavior of flanged walls under simultaneous IP and OOP loading (SM loading scenario). All these studies are conducted via the application of QSM load in IP and OOP directions.

The CB simulations in ref. [76] show that the influence of flanges on the IP response of cantilever walls under varying levels of two-way bending OOP pre-load depends on flange configuration, wall geometry, and pre-compression level. For square walls, flanged and non-flanged specimens exhibit similar OOP/IP interaction effects, except when subjected to the highest pre-compression level (12.5% of f'_m), where flanged walls show a marginal (10%) larger reduction in IP strength at an OOP pre-load of 80% of capacity. In squat walls ($h/l = 0.5$), the ⊥ configuration has minimal impact, whereas ⊥ and ⊏ walls exhibit

significantly worse performance, with an average 30% higher decrease in IP strength at the 80% pre-load level compared to non-flanged walls. This is attributed to the flanges shifting the IP failure mechanism from rocking to diagonal cracking, which is more sensitive to the two-way bending OOP pre-load. The ⊥ configuration remains unaffected due to the small flange size ($l_f/l = 0.14$), which does not induce a failure mode shift. As pre-compression increases, the disparity between flanged and non-flanged walls diminishes, yet the ⊏ wall still shows a 20% reduction in IP strength at maximum pre-compression. Tall walls ($h/l = 1.3$) exhibit the highest sensitivity to flange presence. Without pre-compression, at an 80% OOP pre-load level, the ⊏ wall performs similarly to non-flanged specimens, while the ⌶ wall shows a 20% higher IP strength, and the ⊥ wall demonstrates 50% more strength. While all flanged tall walls develop diagonal cracking rather than rocking, the ⌶ and ⊏ configurations experience more extensive cracking at wall-flange intersections, hence leading to less improvement of the IP strength compared to the ⊥ wall. However, under the highest pre-compression (12.5% of f'_m), the enhancement in the ⊥ wall disappears, and all flanged walls revert to the performance levels of non-flanged walls due to increased vertical confinement limiting cracking during OOP pre-loading.

Under CB loading, the two-way bending OOP behavior of ⌶ walls with and without opening in ref. [70], previously introduced in Section 4.2.1 does not exhibit a consistent trend of variation compared to their non-flanged counterparts in terms of sensitivity to cantilever IP pre-deformation. In several cases, such as the solid wall, walls with a symmetric or asymmetric small window (7.7% of wall area), the wall with an asymmetric small door (19% of wall area), and one of the walls with combined window and door openings (25% of wall area), no discernible difference is observed between flanged and non-flanged variants. However, walls with a large symmetric window (21% of wall area) or a large door (30% of wall area) show a 30% lower reduction in OOP strength at the highest IP pre-damage levels (corresponding to 0.25% IP drift) compared to their non-flanged counterparts, though this behavior is only observed under the largest (25% of f'_m) and zero pre-compression conditions. At other pre-compression levels, no significant influence of flanges is detected. Conversely, the flanged variant of the wall with a combined window and door opening, where the top edge of the window aligns with the top of the door, experiences slightly higher ultimate OOP strength reduction across all pre-compression levels. A direct explanation for these variations is not provided in ref. [70], but it is noted that the presence of flanges introduces additional cracking paths at the wall-flange intersections, absent in non-flanged specimens. In cases where OOP strength reduction is mitigated, it is likely that the lateral confinement provided by flanges enhances the OOP stability of the main panels. In contrast, for the wall exhibiting greater OOP strength degradation, this lateral confinement may have intensified damage concentration at the pier between the openings, leading to a more rapid loss of strength.

Similar to the SM loading study of ref. [59] on non-flanged walls, ref. [87] investigates square ⌶ walls subjected to concurrent OOP and IP load, with varying OOP:IP intensity ratios ranging from exclusive IP loading to 2:1. The load is applied as imposed top displacements, and different flange sizes, ranging from 36% to 120% of the wall length, are examined under both double-clamped uplift-restrained and cantilever boundary conditions. Overall, the findings align with those of ref. [59]. In double-clamped walls, the SM loading does not alter strength or failure mechanisms, indicating that the IP response dominates the behavior. For cantilever walls, only a modest 20% reduction in strength is observed at the highest OOP:IP ratio (2:1) compared to the IP-loaded counterparts. This suggests that even under simultaneous bi-directional loading, the IP response primarily governs the overall structural behavior.

5. Available Extrapolations of Wall-Level Findings to the Building-Level Response

The studies reviewed in Section 4 demonstrate the importance of direct IP-OOP interaction and Flange effects on the response of non-flanged URM walls and provide key insights for the development of accurate methodologies for the seismic assessment of entire buildings. Nonetheless, current guidelines provide little to no recommendations on how to incorporate them into structural design and assessment. Specifically, existing standards [42–46] only include provisions to consider the presence of flanges when evaluating the IP wall response to lateral loads, leaving a substantial gap in addressing the broader interaction effects.

By analyzing the response of individual walls, researchers have attempted to extrapolate findings to predict the seismic behavior of entire buildings. Figure 10 presents the number of publications proposing methodologies to integrate direct IP-OOP interaction and Flange effects in building-level studies. Regarding direct IP-OOP interaction effects, nine regression-based formulations derived from numerical data are introduced in 10 publications [56–59,63,64,66,69,76,120], and three mechanics-based approaches appear in 4 papers [61,62,65,68]. Additionally, three macro-element models are proposed for building-level simulations that partially account for direct IP-OOP interaction effects [26,121,122]. For Flange effects, one regression-based equation [89], two mechanics-based equations [81,123], and one macro-element model [41] are developed. Furthermore, one regression-based equation [76] and one hybrid macro-element modeling approach [76] are introduced to capture the influence of Flange effects on the response under direct IP-OOP interaction effects. This section provides an overview of these developments and their potential application in improving seismic design and assessment methodologies.

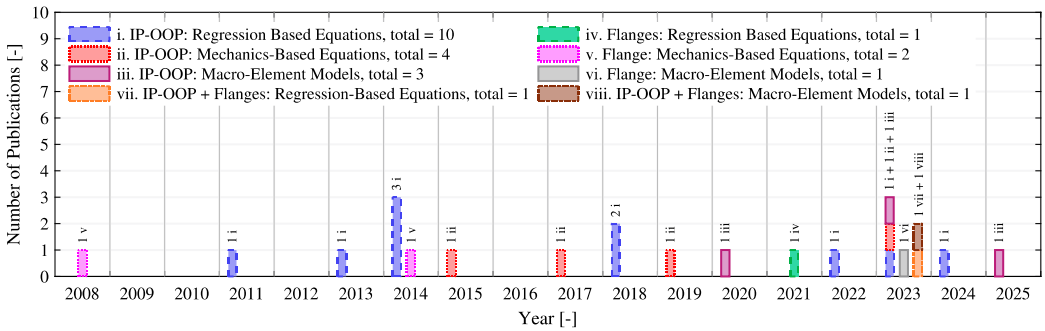

Figure 10. Overview of analytical developments for the assessment and simulation of non-framed unreinforced masonry buildings under the effects of different interactions between IP and OOP behaviors and Flange effects. For the meaning of abbreviations, please refer to the Nomenclature section.

5.1. Regression-Based Design and Assessment Formula

The research on OOP/IP interaction effects in non-flanged URM walls has led to the development of six regression-based formulations [56,57,63,64,66,69,76] for predicting the impact of OOP pre-load on IP strength, inspired by the 3/2-power curve introduced in [124], which is the only formulation incorporated in standards [125] to consider the effects of OOP/IP interaction in the response of framed URM walls. Although originally proposed for infill walls, the 3/2-power curve has aided the development of similar interaction curves for non-framed URM walls via the results of numerical simulations under the CB loading scenario. Najafgholipour et al. [56,57] formulate an interaction curve for double-clamped IP walls subjected to constant two-way bending OOP load, incorporating the influence of the variations in material properties and aspect ratio. Noor-E-Khuda and Dhanasekar [76] develop similar curves with a focus on different two-way bending OOP

boundary conditions. Specifically, the curves are produced for walls with four supported sides [63] and three supported sides with a lateral edge free for OOP movement [64], accounting for aspect ratio and pre-compression. Kesavan and Menon [66] introduce a curve for one-way bending beam-like OOP pre-loading on double-clamped IP walls, while Zeng and Li [69] extend the approach to cantilever IP walls, factoring in slenderness ratio, aspect ratio, and pre-compression. Patel and Dubey [76] apply their model to cantilever IP walls under two-way bending OOP pre-load.

Beyond interaction curves, two mechanics-based methodologies [62,65,68] offer predictions for IP strength under OOP/IP interaction effects. Kollerathu and Menon [62,65] modify the equations established in ref. [126] for IP double-clamped strength by introducing reductions in the peak resistance based on pre-applied or concurrent one-way bending beam-like OOP deformation. Their methodology distinguishes between CB loading, where OOP pre-deformation reduces the effective cross-section, and SM loading, where the reduction in IP strength can also occur due to localized crushing of one side of the cross-section of the wall because of excessive OOP deformation. Krishnachandran and Menon [68] extend a similar approach to IP cantilever walls under one-way bending cantilever OOP pre-deformation.

Additional regression-based interaction curves are introduced in three studies [58,59,120] for other direct IP-OOP interaction scenarios with different loading assumptions. Dolatshahi et al. [59] propose power curves for estimating resistance at yield, peak strength, and ultimate states under SM double-clamped IP and cantilever OOP deformation with different OOP:IP loading ratios. Bakhshi et al. [58] and Khanmohammadi and Behnam [120] present interaction curves for peak IP and OOP strengths under various loading conditions, though the data used for the development of their functions are not available. Furthermore, Dolatshahi et al. [61] develop a mechanics-based limit state analysis to determine failure location, type, and overall strength in walls under IP double-clamped and OOP one-way bending beam-like SM loading. Their approach identifies potential failure mechanisms by evaluating mechanical stress distributions and selecting the mode that activates at the lowest load.

For Flange effects, analytical works primarily address F/IP interactions. Yi et al. [123] propose mechanics-based equations for predicting the IP strength and stiffness of ⌊ walls, considering flange length and thickness, and assuming that the failure of walls starts with rocking, followed by toe crushing or shear sliding. Khanmohammadi et al. [81] refine these equations to distinguish between bed joint sliding and diagonal tension failure modes, as well as to incorporate ⌶ and ⊏ flange configurations. Alamdari et al. [88,89] introduce regression-based correction factors for ASCE 41 [125] equations, enabling the inclusion of Flange effects in the axial load contributing to the resistance for ⌶ and ⊏ walls. The only study extending F/IP-OOP interaction effects belongs to Patel and Dubey [76], who propose regression-based interaction curves for non-flanged and flanged walls with different configurations, aspect ratios, and pre-compression levels.

5.2. Macro-Element Numerical Models Capable of Simulating IP-OOP Interaction Effects in Buildings

Many well-developed numerical models capable of simulating direct IP-OOP interactions and Flange effects exist in the literature. One of the earliest and most influential models is the block-based model proposed by Lourenço et al. [127,128], which has served as the foundation for numerous subsequent developments, such as those, for example, utilizing micro-scale finite element [66,105,129–135], discrete element [82,136–140], applied element [141], and hybrid methodologies [142], as well as meso-scale block-based models [25,143–145]. While these models and other similar methodologies offer high-fidelity simulation of direct IP-OOP interaction and Flange effects, along with cap-

turing various local and global failure mechanisms, their high computational cost limits their efficiency for wall-level and larger-scale studies. Similar limitations apply to plasticity-based [55,146–150] and crack-based [150] continuum models, which can accurately capture IP and OOP responses but require robust calibration as well as remain computationally expensive for extensive structural analysis.

To address these challenges, five studies [26,41,76,121,122] have proposed more efficient macro-scale numerical modeling approaches, designed to be trained using wall-level studies and applied to building-level analyses while partially accounting for direct IP-OOP interactions or Flange effects. Vanin et al. [26] introduce a macro-element equivalent frame modeling methodology in which walls and piers are represented each as two beam-column elements interconnected at their end nodes. This model allows for the analysis of walls both as individual components and as integral parts of larger structures. The flexural and shear deformations of each wall are incorporated through mechanics-based formulations, with flexural behavior accounted for in both IP and OOP directions, and shear response and failure considered only in the IP direction. The coupling of IP and OOP flexural responses, along with their resultant crushing failure, is modeled using fiber-based or pre-integrated cross-sections assigned to the end and middle nodes between the beam-columns. The interconnection of building walls and floors is achieved through zero-length rigid or deformable springs, the latter implicitly incorporating Flange effects and capturing failure mechanisms at wall corners and wall-to-roof junctions. Salvatori et al. [122] propose a similar approach with the addition of accounting for shear response in both IP and OOP directions. However, the one-way bending OOP is not accounted for in ref. [122], as each pier or wall is simulated via a single beam-column element without a middle node to allow the simulation of mid-height cracks.

Kesavan and Menon [121] extend the methodology of ref. [26] by introducing regression-based OOP/IP interaction, derived from detailed numerical studies, for the model to include the impact of one-way bending beam-like OOP deformation on double-clamped IP stiffness and elastic behavior. Cattari et al. [41] refine the mechanics-based stiffness formulation for the zero-length wall-to-wall links to incorporate the influence of different connection qualities at wall intersections on the Flange effects. Lastly, Patel and Dubey [76] develop a simplified mass-and-spring building model, where each wall is represented by a spring characterized by mechanics-based IP and OOP stiffnesses. This model estimates the IP resistance of each wall within the building based on its OOP demands, while intersecting walls are accounted for, and the regression-based OOP/IP interaction curves developed in the study. It should be noted that, due to the specific geometric configuration (i.e., beam-column elements aligned with the centerline of the walls or piers), the methodologies presented here are generally suited for reproducing one-way bending OOP responses and are not applicable to components with two-way bending deformation.

6. Current Knowledge Gaps in the Study of Interaction Effects in Non-Framed URM Walls

The seismic response of non-framed URM walls subjected to combined IP and OOP actions presents a complex challenge that remains insufficiently addressed in current research and practice. Although recent earthquake events have highlighted the vulnerability of such structures, the existing literature lacks a cohesive understanding of the influence of IP-OOP interactions and Flange effects on both wall- and building-level behavior. This knowledge gap hinders the development of reliable design methodologies and predictive tools. Advancing the state of the art in this domain necessitates a multidisciplinary approach that integrates structural mechanics, material science, and computational modeling. A more systematic investigation of interaction effects, grounded in targeted experimental

programs and supported by refined numerical simulations, will be essential to translate wall-scale observations into building-scale applications. The following sections discuss the primary knowledge gaps found by the current review and outline research directions aimed at supporting safer and more resilient masonry construction.

6.1. Scientific Gaps in Understanding the Interaction Effects

The current body of research on IP-OOP interaction effects in non-framed URM walls reveals a notable imbalance in the depth of investigation across different interaction scenarios. The majority of existing studies focus on the influence of OOP pre-damage or deformation on IP behavior, while the reverse scenarios (IP-induced impacts on OOP response) remain significantly underexplored. This gap is particularly critical considering the intrinsic vulnerability of URM walls in the OOP direction and the potential for IP damage to induce failure planes that compromise OOP stability. The limited number of studies addressing IP/OOP interactions under realistic seismic conditions or settlement-induced damage constrains the development of predictive models and design strategies with comprehensive applicability. Furthermore, the role of flanges in influencing both IP and OOP responses remains insufficiently understood, especially in configurations where flange geometry and boundary conditions interact with multi-directional loading scenarios and IP-OOP interaction effects. The influence of variations in top uplift restriction, wall openings, and slenderness ratio on interaction effects is either insufficiently explored or shows no consistent trends. Similarly, the variation of Flange effects across specimens with differing slenderness or opening configurations requires further investigation. Current analytical formulations and macro-element models primarily address OOP/IP interaction and F/IP effects, leaving F/OOP and IP/OOP effects inadequately represented. The lack of a unified classification framework for interaction scenarios, along with the absence of standardized methodologies for extrapolating wall-level observations to building-scale behavior, further impedes progress in this area. Bridging these research gaps necessitates a more balanced investigative approach, integrating experimental and numerical studies that systematically examine the full spectrum of interaction effects across a range of structural configurations and loading conditions.

6.2. Limitations in Experimental and Numerical Methodologies

Despite the valuable insights provided by existing experimental and numerical studies on IP-OOP interaction and Flange effects in non-framed URM walls, several methodological limitations exist. Experimental investigations are often constrained by the high cost and complexity of full-scale testing, resulting in a reliance on small-scale wallet specimens and simplified loading protocols. Such experimental setups frequently fail to replicate realistic seismic conditions, particularly in terms of simultaneous multi-directional loading and the cumulative effects of repeated events. Moreover, inconsistencies in boundary conditions, wall geometries, and material properties across different studies limit the comparability of results and impede the development of generalized conclusions. The influence of critical parameters such as flange geometry, vertical overburden, and opening configurations remains insufficiently explored, while the absence of standardized testing protocols continues to restrict the reproducibility and scalability of experimental findings. Numerical modeling, although offering greater flexibility, is similarly constrained by idealized assumptions and a lack of thorough validation. Most existing models prioritize OOP/IP and F/IP interactions, with limited focus on IP/OOP and F/OOP effects. Continuum-based modeling approaches, while capable of capturing detailed responses, are computationally demanding and seldom employed at the building scale. Conversely, simplified block-based models often disregard complex boundary interactions and material heterogeneity. Macro-element models, which

hold promise for large-scale applications, remain in early development stages and typically do not capture the full range of interaction effects. Finally, the current numerical studies have primarily employed simplified monotonic loading procedures, leaving a critical gap in the understanding of interaction effects under more realistic quasi-static cyclic or dynamic loadings. Moving forward, experimental campaigns should prioritize full-scale, multi-directional testing under realistic boundary conditions, coupled with systematic variation of key parameters. Such efforts are essential for enabling robust model calibration and advancing the development of predictive tools tailored to design applications.

6.3. Practical Gaps in Design and Assessment Guidelines

Despite the growing recognition of IP-OOP interaction and Flange effects on non-framed URM walls, current design and assessment guidelines remain largely inadequate in addressing these complexities. Most existing provisions treat IP and OOP behaviors as independent phenomena, disregarding the compounded effects that emerge under realistic seismic loading. This simplification is particularly problematic in non-framed configurations, where the absence of confining structural frames heightens the significance of wall-to-wall interactions and geometric discontinuities. Consequently, critical failure mechanisms, such as those initiated by pre-existing damage or flange-induced stress redistribution, are frequently omitted from standard design checks. The limited incorporation of interaction effects into predictive models and assessment tools further exacerbates this shortcoming. Although some empirical relationships and macro-element formulations exist, these are typically calibrated for isolated loading scenarios and fail to capture the complete range of interaction mechanisms, particularly IP/OOP and F/OOP interaction effects. Moreover, many of these models rely on idealized assumptions and lack validation against full-scale experimental data, thereby limiting their reliability and applicability in practice. This disconnect between emerging research and engineering application leaves practitioners without robust methodologies for evaluating the seismic vulnerability of URM buildings, especially in regions prone to frequent low-to-moderate seismicity or induced seismic events. Another critical limitation lies in the extrapolation of wall-level insights to building-scale performance. Current approaches for scaling experimental or numerical findings to the structural level are either overly simplified or entirely absent, thereby restricting their utility in comprehensive seismic assessments. The lack of standardized procedures for integrating interaction-sensitive parameters, such as flange geometry, boundary conditions, and cumulative damage, into design workflows further impedes the practical adoption of research outcomes. Bridging this gap requires not only the advancement of analytical and numerical models, but also a concerted effort to embed these developments into design codes and regulatory frameworks, thereby ensuring that the complex seismic behavior of URM walls is appropriately addressed in future construction and retrofit strategies.

7. Conclusions

This paper presents a comprehensive review of existing studies on the interaction between in-plane (IP) and out-of-plane (OOP) behaviors in non-framed unreinforced masonry (URM) walls, i.e., walls not supported by a surrounding frame such as reinforced concrete or steel members, including both single-wall configurations (without flanges) and flanged walls. A large dataset is compiled from experimental and numerical research investigating two main interaction scenarios: the first involves direct IP-OOP interaction effects, where IP and OOP responses influence one another; the second concerns Flange effects, where the presence of flanges alters the IP or OOP behavior of walls. Key properties affecting these interactions are identified through cross-comparisons of studies conducted at the wall level. Additionally, a brief review is provided of current analytical design

and assessment formulas, as well as macro-element models incorporating direct IP-OOP interactions and Flange effects for building-level analyses. The main findings are as follows:

- A consistent framework for classifying interaction scenarios is lacking in the literature. This study introduces a unified terminology to support clearer communication and comparison across studies.
- Boundary conditions are a decisive factor in shaping interaction effects. The strongest interactions occur when IP and OOP failure mechanisms produce overlapping crack patterns.
- Flange effects significantly influence both IP and OOP responses, but their impact varies depending on wall geometry, vertical pre-compression, and loading configuration.
- Current predictive models and macro-element formulations only partially capture the complexity of interaction effects, and their applicability to building-level analysis remains limited.
- Existing design and assessment guidelines do not adequately incorporate IP–OOP interactions or Flange effects, leaving a gap between research findings and engineering practice.

Overall, the findings underscore the importance of accounting for interaction effects in the seismic assessment of URM walls and highlight the need for more integrated approaches in modeling and design. Future research should prioritize the following areas:

- Expanded experimental campaigns: development of testing facilities capable of simulating realistic seismic loading scenarios, including simultaneous IP and OOP actions, is essential. Full-scale tests on flanged and non-flanged walls with varied geometries and boundary conditions will provide critical data for model validation.
- Advanced numerical modeling: refinement of continuum-based and discrete element models to incorporate complex interaction mechanisms, including IP/OOP and F/OOP effects, is needed. These models should be calibrated against experimental data and capable of simulating building-level behavior.
- Analytical frameworks: mechanics-based approaches that account for multi-directional loading, flange configurations, and material heterogeneity should be developed. These frameworks must be adaptable to different wall typologies and loading histories.
- Integration into design codes: collaboration with regulatory bodies to translate research findings into practical design provisions is crucial. This includes the development of simplified assessment tools and design charts that incorporate interaction effects.
- Consideration of induced seismicity and cumulative damage: regions experiencing frequent low-magnitude earthquakes require tailored methodologies that account for cumulative damage and settlement effects on OOP stability.

Author Contributions: A.G.: Conceptualization, Methodology, Validation, Formal analysis, Investigation, Resources, Data Curation, Writing—Original Draft, Writing—Review and Editing, Visualization. J.G.R.: Conceptualization, Validation, Writing—Review and Editing, Supervision, Project administration, Funding acquisition. F.M.: Conceptualization, Methodology, Validation, Resources, Data Curation, Writing—Review and Editing, Supervision, Project administration, Funding acquisition. All authors have read and agreed to the published version of the manuscript.

Funding: This research was conducted as part of the scientific consolidation of projects funded by Nederlandse Aardolie Maatschappij (NAM) BV under contract number UI46268 "Physical testing and modeling–Masonry structures Groningen", which is gratefully acknowledged.

Data Availability Statement: All data and code that support the findings of this study are available from the author upon reasonable request.

Acknowledgments: The data used in this paper were gathered from the relevant studies published in the literature. References to the studies corresponding to each portion of the text have been made in the manuscript.

Conflicts of Interest: The authors declare no conflict of interest.

Nomenclature

***General Terms** **
URM: Unreinforced Masonry
IP: In-Plane
OOP: Out-of-Plane

Interaction Scenarios
IP-OOP: Influence of IP response on OOP behavior of walls and vice versa
IP/OOP: Effects of IP pre-damage, pre-deformation, pre-load, or concurrent load on OOP response of walls
OOP/IP: Effects of OOP pre-damage, pre-deformation, pre-load, or concurrent load on IP response of walls
F/IP: Effects of the presence of flanges on the IP response of the main walls
F/OOP: Effects of the presence of flanges on the OOP response of the main walls
F/IP-OOP: Effects of the presence of flanges on the response of the main walls to direct IP-OOP interaction effects

Numerical Modeling Approaches
SMSBB: Simplified Micro-Scale Block-Based
CoB: Continuum-Based

Specimen Type
Wt: Wallet
NFW: Non-Flanged Wall
FW: Flanged Wall

Masonry Unit Type
HCLB: Hollow Clay Block/Brick
HCB: Hollow Concrete Block/Brick
SFAB: Solid Fly Ash Block
SCLB: Solid Clay Brick
SCSBL: Solid Calcium Silicate Block
SMB: Solid Marble Brick
SSB: Solid Sugar Block

Masonry Unit Configuration1
H: Horizontal Holes
V: Vertical Holes
$\mathbf{f'_m}$: Masonry Prism Compressive Strength

Mortar Type and Configuration
C: Cement
L: Lime
S: Sand
DHJ: Dry Head Joints

Opening Type and Position
D: Door
W: Window
OF: Opening on Flanges

Geometrical Properties
h/l: Height/Length Aspect Ratio
h/t: Height/Thickness Slenderness Ratio
$\mathbf{l_f/l}$: Flange/Wall Length Ratio
t: Wall Thickness

Loading Scenarios
SQ: Sequential
SC: Successive
CB: Combined
SM: Simultaneous

Loading Sequences
IP, OOP: IP load, then OOP
OOP, IP: OOP load, then IP
IP, OOP, IP: Alternative loading starting from IP
OOP, IP, OOP: Alternative loading starting from OOP
IP + OOP: Concurrent IP and OOP loads

Loading Procedures
QSM: Quasi-Static Monotonic
QSC: Quasi-Static Cyclic
QSLUC: Quasi-Static Load-Unload Cycles
Dyn: Dynamic

Loading Apparatus
DiC: Diagonal Compression
WFMiPL: Wall Face Middle-Point Load
MHD: Mid-Height Displacement
ToD: Top Displacement
WF3PL: Wall Face Three-Point Load
BR: Base Rotation
ToL: Top Load
WFP: Wall Face Pressure
ST: Shake Table

Boundary Conditions
Ct: Cantilever
1WB: One-Way Bending
RTU: Restricted Top Uplift
FR3E: Free Rotation at Top and Side Edges
FTE: Free OOP Motion of Top Edge
SCt: Semi-Cantilever
2WB: Two-Way Bending
RTRU: Restricted Top Rotation and Uplift
FRSE: Free Rotation at Two Side Edges
F1SE: Free OOP Motion of One Side Edge
DC: Double-Clamped
B: Beam-like
FR4E: Free Rotation at All Four Edges
FRTE: Free Rotation at Top Edge
NLC: No IP Confinement at Two Side Edges

* The abbreviations are shown with bold text and are classified into several categories, shown with bold italic text, based on the information they provide.

References

1. Hendry, E.A.W. Masonry walls: Materials and construction. *Constr. Build. Mater.* **2001**, *15*, 323–330. [CrossRef]
2. Moon, L.; Dizhur, D.; Senaldi, I.; Derakhshan, H.; Griffith, M.; Magenes, G.; Ingham, J. The demise of the URM building stock in Christchurch during the 2010-2011 Canterbury earthquake sequence. *Earthq. Spectra* **2014**, *30*, 253–276. [CrossRef]
3. Page, A.W. The Newcastle Earthquake—Behaviour of Masonry Structures. *Mason. Int.* **1991**, *5*, 11–18.
4. Penna, A.; Morandi, P.; Rota, M.; Manzini, C.F.; da Porto, F.; Magenes, G. Performance of masonry buildings during the Emilia 2012 earthquake. *Bull. Earthq. Eng.* **2014**, *12*, 2255–2273. [CrossRef]
5. Oyarzo-Vera, C.; Griffith, M.C. The Mw 6.3 Abruzzo (Italy) earthquake of april 6th, 2009: On site observations. *Bull. N. Z. Soc. Earthq. Eng.* **2009**, *42*, 302–307.
6. D'Ayala, D.F.; Paganoni, S. Assessment and analysis of damage in L'Aquila historic city centre after 6th April 2009. *Bull. Earthq. Eng.* **2011**, *9*, 81–104. [CrossRef]

7. İzol, R.; Işık, E.; Avcil, F.; Arslan, M.H.; Arkan, E.; Büyüksaraç, A. Seismic performance of masonry structures after 06 February 2023 earthquakes; site survey and FE modelling approach. *Soil Dyn. Earthq. Eng.* **2024**, *186*, 108904. [CrossRef]
8. Işık, E.; Bilgin, H.; Avcil, F.; İzol Arkan, E.; Büyüksaraç, A.; Harirchian, E.; Hysenlliu, M. Seismic Performances of Masonry Educational Buildings during the 2023 Türkiye (Kahramanmaraş) Earthquakes. *GeoHazards* **2024**, *5*, 700–731. [CrossRef]
9. Frankie, T.M.; Gencturk, B.; Elnashai, A.S. Simulation-Based Fragility Relationships for Unreinforced Masonry Buildings. *J. Struct. Eng.* **2013**, *139*, 400–410. [CrossRef]
10. Aşıkoğlu, A. Performance-Based Approach on Masonry Buildings by Means of Experimental and Numerical Pushover Analysis. Ph.D. Thesis, Universidade do Minho, Guimarães, Portugal, 2024.
11. Graziotti, F.; Tomassetti, U.; Sharma, S.; Grottoli, L.; Magenes, G. Experimental response of URM single leaf and cavity walls in out-of-plane two-way bending generated by seismic excitation. *Constr. Build. Mater.* **2019**, *195*, 650–670. [CrossRef]
12. Tondelli, M.; Beyer, K.; DeJong, M. Influence of boundary conditions on the out-of-plane response of brick masonry walls in buildings with RC slabs. *Earthq. Eng. Struct. Dyn.* **2016**, *45*, 1337–1356. [CrossRef]
13. Sumerente, G.; Lovon, H.; Tarque, N.; Chácara, C. Assessment of combined in-plane and out-of-plane fragility functions for adobe masonry buildings in the peruvian andes. *Front. Built Environ.* **2020**, *6*, 52. [CrossRef]
14. Clough, R.W.; Gülkan, P.; Manos, G.C.; Mayes, R.L. Seismic Testing of Single-Story Masonry Houses: Part 2. *J. Struct. Eng.* **1990**, *116*, 235–256. [CrossRef]
15. Mojsilovic, N. Masonry walls with a multi-layer bed joint subjected to in-plane cyclic loading: An experimental investigation. *Eng. Struct.* **2017**, *143*, 189–203. [CrossRef]
16. Morandi, P.; Albanesi, L.; Graziotti, F.; Piani, T.L.; Penna, A.; Magenes, G. Development of a dataset on the in-plane experimental response of URM piers with bricks and blocks. *Constr. Build. Mater.* **2018**, *190*, 593–611. [CrossRef]
17. Messali, F.; Esposito, R.; Ravenshorst, G.J.P.; Rots, J.G. *Experimental Investigation of the In-Plane Cyclic Behaviour of Calcium Silicate Brick Masonry Walls*; Springer: Dordrecht, The Netherlands, 2020; Volume 18. [CrossRef]
18. Pereira, J.M.; Correia, A.A.; Lourenço, P.B. In-plane behaviour of rubble stone masonry walls: Experimental, numerical and analytical approach. *Constr. Build. Mater.* **2021**, *271*, 121548. [CrossRef]
19. Petry, S.; Beyer, K. Cyclic Test Data of Six Unreinforced Masonry Walls with Different Boundary Conditions. *Earthq. Spectra* **2015**, *31*, 2459–2484. [CrossRef]
20. Mojsilović, N. Strength of masonry subjected to in-plane loading: A contribution. *Int. J. Solids Struct.* **2011**, *48*, 865–873. [CrossRef]
21. Liu, Z.; Crewe, A. Effects of size and position of openings on in-plane capacity of unreinforced masonry walls. *Bull. Earthq. Eng.* **2020**, *18*, 4783–4812. [CrossRef]
22. Vaculik, J.; Griffith, M.C. Out-of-plane shaketable testing of unreinforced masonry walls in two-way bending. *Bull. Earthq. Eng.* **2018**, *16*, 2839–2876. [CrossRef]
23. Malomo, D.; DeJong, M.J. A Macro-Distinct Element Model (M-DEM) for simulating in-plane/out-of-plane interaction and combined failure mechanisms of unreinforced masonry structures. *Earthq. Eng. Struct. Dyn.* **2022**, *51*, 793–811. [CrossRef]
24. Vanin, F.; Penna, A.; Beyer, K. A three-dimensional macroelement for modelling the in-plane and out-of-plane response of masonry walls. *Earthq. Eng. Struct. Dyn.* **2020**, *49*, 1365–1387. [CrossRef]
25. Malomo, D.; Pinho, R.; Penna, A. Numerical modelling of the out-of-plane response of full-scale brick masonry prototypes subjected to incremental dynamic shake-table tests. *Eng. Struct.* **2020**, *209*, 110298. [CrossRef]
26. Nodargi, N.A.; Bisegna, P. A variational-based non-smooth contact dynamics approach for the seismic analysis of historical masonry structures. *Comput. Methods Appl. Mech. Eng.* **2024**, *432*, 117346. [CrossRef]
27. Nodargi, N.A.; Bisegna, P. A variational event-driven approach for the dynamic analysis of multi-block historical masonry structures under ground excitation. *Eng. Struct.* **2024**, *306*, 117804. [CrossRef]
28. Portioli, F.P.A. Rigid block modelling of historic masonry structures using mathematical programming: A unified formulation for non-linear time history, static pushover and limit equilibrium analysis. *Bull. Earthq. Eng.* **2020**, *18*, 211–239. [CrossRef]
29. Chong, V.L. The Behaviour of Laterally Loaded Masonry Panels with Openings. Ph.D. Thesis, University of Polymouth, Polymouth, UK, 1993.
30. Van der Pluijm, R. Out-Of-Plane Bending of Masonry: Behaviour and Strength. Ph.D. Thesis, Technische Universiteit Eindhoven, Eindhoven, The Netherlands, 1999.
31. Liang, C. Experimental and Theoretical Investigation of the Behaviour of Brickwork Cladding Panel Subjected to Lateral Loading. Ph.D. Thesis, University of Edinburgh, Edinburgh, UK, 1996.
32. Derakhshan, H.; Lucas, W.; Visintin, P.; Griffith, M.C. Out-of-plane Strength of Existing Two-way Spanning Solid and Cavity Unreinforced Masonry Walls. *Structures* **2018**, *13*, 88–101. [CrossRef]
33. Bui, T.T.; Limam, A. Out-of-plane behaviour of hollow concrete block masonry walls unstrengthened and strengthened with CFRP composite. *Compos. Part B Eng.* **2014**, *67*, 527–542. [CrossRef]
34. Messali, F.; Ravenshorst, G.; Esposito, R.; Rots, J.G. Large-Scale Testing Program for the Seismic Characterization of Dutch Masonry Walls. In Proceedings of the 16th World Conference on Earthquake, Santiago, Chile, 9–13 January 2017.

35. Griffith, M.C.; Vaculik, J.; Lam, N.T.K.; Wilson, J.; Lumantarna, E. Cyclic testing of unreinforced masonry walls in two-way bending. *Earthq. Eng. Struct. Dyn.* **2007**, *36*, 801–821. [CrossRef]
36. Padalu, P.K.V.R.; Singh, Y.; Das, S. Cyclic two-way out-of-plane testing of unreinforced masonry walls retrofitted using composite materials. *Constr. Build. Mater.* **2020**, *238*, 117784. [CrossRef]
37. Candeias, P.X.; Costa, A.C.; Mendes, N.; Costa, A.A.; Lourenço, P.B. Experimental Assessment of the Out-of-Plane Performance of Masonry Buildings Through Shaking Table Tests. *Int. J. Archit. Herit.* **2016**, *11*, 31–58. [CrossRef]
38. Bothara, J.K.; Dhakal, R.P.; Mander, J.B. Seismic performance of an unreinforced masonry building: An experimental investigation. *Earthq. Eng. Struct. Dyn.* **2009**, *39*, 45–68. [CrossRef]
39. Ghezelbash, A.; Beyer, K.; Dolatshahi, K.M.; Yekrangnia, M. Shake table test of a masonry building retrofitted with shotcrete. *Eng. Struct.* **2020**, *219*, 110912. [CrossRef]
40. Cattari, S.; Alfano, S.; Lagomarsino, S. A Practice-Oriented Proposal to Consider the Flange Effect in Equivalent Frame Modeling of Masonry Buildings. *Buildings* **2023**, *13*, 462. [CrossRef]
41. *IS 1905*; Code of Practise for Structural use of Unreinforced Masonry. Bureau of Indian Standards: New Delhi, India, 1987.
42. *AS 3700*; Australian Standard for Masonry Structures. Standards Australia Committee BD-004: Sydney, Australia, 2011.
43. *EN 1996-1-1*; Eurocode 6: Design of Masonry Structures—Part 1-1: General Rules for Reinforced and Unreinforced Masonry Structures. European Committee for Standardization: Brussels, Belgium, 2005.
44. *NPR 9998:2020*; Assessment of Structural Safety of Buildings in Case of Erection, Reconstruction and Disapproval—Induced Earthquakes—Basis of Design, Actions and Resistance. Netherlands Standardization Institute: Delft, The Netherlands, 2020.
45. *ACI 530-02/ASCE 5-02/TMS 402-02*; Building code Requirements for Masonry Structures. Masonry Standards Joint Committee (MSJC): Boulder, CO, USA; American Concrete Institute: Farmington Hills, MI, USA; Structural Engineering Institute of the American Society of Civil Engineers: Reston, Virginia; The Masonry Society: Fort Collins, Colorado, 2002.
46. Dauda, J.A.; Iuorio, O.; Muhit, I.B.; da Silva, L.C.M. Systematic review of experimental testing of masonry walls' failure: Comparative analysis and future directions. *Eng. Fail. Anal.* **2024**, *163*, 108571. [CrossRef]
47. Celano, T.; Argiento, L.U.; Ceroni, F.; Casapulla, C. Literature Review of the In-Plane Behavior of Masonry Walls: Theoretical vs. Experimental Results. *Materials* **2021**, *14*, 3063. [CrossRef]
48. Chang, L.; Messali, F.; Esposito, R. Capacity of unreinforced masonry walls in out-of-plane two-way bending: A review of analytical formulations. *Structures* **2020**, *28*, 2431–2447. [CrossRef]
49. Bozyigit, B.; Ozdemir, A.; Donmez, K.; Dalgic, K.D.; Durgut, E.; Yesilyurt, C.; Dizgin, Y.; Yıldeniz, C.; İspir Arslan, M.; Bedirhanoglu, I.; et al. Damage to monumental masonry buildings in Hatay and Osmaniye following the 2023 Turkey earthquake sequence: The role of wall geometry, construction quality, and material properties. *Earthq. Spectra* **2024**, *40*, 1870–1904. [CrossRef]
50. Cheng, Q.; Wang, Y.; Dai, D.; Xi, N.; Tian, Y.; Lu, X. Post-event seismic damage assessment of 2023 M6.2 Gansu Jishishan earthquake based on RED-ACT system. *Earthq. Eng. Resil.* **2024**, *3*, 475–489. [CrossRef]
51. Imtiaz, A.; Saloustros, S.; Beqiraj, M.; Cortés, G.; Devaux, M.; Lattion, E.; Zhu, Y.; Sehaqui, H. Understanding building damage through the lens of the Swiss post-seismic reconnaissance mission of 2023 Al Haouz, Morocco, earthquake. *Sci. Rep.* **2025**, *15*, 16587. [CrossRef]
52. Royal Netherlands Meteorological Institute (KNMI). Aardbevingen Door Gaswinning. Available online: https://www.knmi.nl/kennis-en-datacentrum/uitleg/aardbevingen-door-gaswinning (accessed on 12 August 2025).
53. Dolatshahi, K.M.; Aref, A.J. *Computational, Analytical and Experimental Modeling of Masonry Structures*; Buffalo: New York, NY, USA, 2015.
54. Yi, T.; Moon, F.; Leon, R.; Kahn, L. Flange effects on the nonlinear behavior of URM pier. *Mason. Soc. J.* **2008**, *26*, 31–42. [CrossRef]
55. Najafgholipour, M.A.; Maheri, M.R.; Lourenço, P.B. Capacity interaction in brick masonry under simultaneous in-plane and out-of-plane loads. *Constr. Build. Mater.* **2013**, *38*, 619–626. [CrossRef]
56. Najafgholipour, M.A.; Maheri, M.R.; Lourenço, P.B. Definition of interaction curves for the in-plane and out-of-plane capacity in brick masonry walls. *Constr. Build. Mater.* **2014**, *55*, 168–182. [CrossRef]
57. Bakhshi, A.; Soleymanzadeh, A.; Yekrangnia, M. Interaction of In-plane and Out-of-plane Behavior of Masonry Walls. In Proceedings of the 9th International Masonry Conference (IMC), Guimarães, Portugal, 7–9 July 2014.
58. Dolatshahi, K.M.; Aref, A.J.; Yekrangnia, M. Bidirectional behavior of unreinforced masonry walls. *Earthq. Eng. Struct. Dyn.* **2014**, *43*, 2377–2397. [CrossRef]
59. Dolatshahi, K.M.; Yekrangnia, M. Out-of-plane strength reduction of unreinforced masonry walls because of in-plane damages. *Earthq. Eng. Struct. Dyn.* **2015**, *44*, 2157–2176. [CrossRef]
60. Dolatshahi, K.M.; Aref, A.J.; Whittaker, A.S. Interaction Curves for In-Plane and Out-of-Plane Behaviors of Unreinforced Masonry Walls. *J. Earthq. Eng.* **2015**, *19*, 60–84. [CrossRef]
61. Kollerathu, J.A.; Menon, A. Interaction of In-Plane and Out-of-Plane Responses in Unreinforced Masonry Walls under Seismic Loads. *J. Struct. Eng.* **2017**, *44*, 422–441.

62. Noor-E-Khuda, S.; Dhanasekar, M. Masonry Walls under Combined In-Plane and Out-of-Plane Loadings. *J. Struct. Eng.* **2018**, *144*, 04017186. [CrossRef]
63. Noor-E-Khuda, S.; Dhanasekar, M. Three sides supported unreinforced masonry walls under multi-directional loading. *Constr. Build. Mater.* **2018**, *188*, 1207–1220. [CrossRef]
64. Kollerathu, J.A.; Menon, A. Biaxial Effects in Unreinforced Masonry (URM) Load-Bearing Walls. In *Recent Advances in Structural Engineering*; Rao, A.R.M., Ramanjaneyulu, K., Eds.; Springer: Singapore, 2019; Volume 11. [CrossRef]
65. Kesavan, P.; Menon, A. Investigation of in-plane and out-of-plane interaction in unreinforced masonry piers by block-based micro-modeling. *Structures* **2022**, *46*, 1327–1344. [CrossRef]
66. Sharma, S. Numerical Study of the Effect of Seismic In-Plane Damage on Out-Of-Plane Performance of Unreinforced Masonry Walls. M.Sc. Thesis, Delft University of Technology, Delft, The Netherlands, 2023.
67. Krishnachandran, S.; Menon, A. Effect of out-of-plane displacements on the in-plane capacity of lightly precompressed rocking unreinforced masonry piers. *Eng. Struct.* **2023**, *281*, 115756. [CrossRef]
68. Zeng, B.; Li, Y. In-plane and out-of-plane one-way vertical bending behavior interaction analysis of unreinforced masonry walls with newly developed load capacity interaction curve. *Eng. Struct.* **2024**, *305*, 117729. [CrossRef]
69. Patel, K.P.; Dubey, R.N. Effect of in-plane damage on the out-of-plane strength of masonry walls with openings. *Structures* **2024**, *65*, 106708. [CrossRef]
70. Maheri, M.R.; Najafgholipour, M.A. In-Plane Shear and Out-of-Plane Bending Capacity Interaction In Brick Masonry Walls. In Proceedings of the 15th World Conference on Earthquake Engineering (12WCEE), Lisbon, Portugal, 24–28 September 2012.
71. Gkournelos, P.D.; Triantafillou, T. Integrated Structural and Energy Retrofitting of Masonry Walls: The Effect of In-Plane Damage on the Out-Of-Plane Response. In Proceedings of the 10th International Conference on FRP Composites in Civil Engineering (CICE), Istanbul, Turkey, 8–10 December 2021; Springer International Publishing: Cham, Germany, 2022. [CrossRef]
72. Gkournelos, P.D.; Triantafillou, T.C.; Bournas, D.A. Integrated Structural and Energy Retrofitting of Masonry Walls: Effect of In-Plane Damage on the Out-of-Plane Response. *J. Compos. Constr.* **2020**, *24*, 04020049. [CrossRef]
73. Dolatshahi, K.M.; Aref, A.J. Multi-directional response of unreinforced masonry walls: Experimental and computational investigations. *Earthq. Eng. Struct. Dyn.* **2016**, *45*, 1427–1449. [CrossRef]
74. Sudhakar, M.; Raj, M.P.; Natarajan, C. Interaction study on interlocking masonry wall under simultaneous in-plane and out-of-plane loading. In *Advances in Structural Engineering: Materials*; Springer: New Delhi, India, 2015; Volume 3. [CrossRef]
75. Patel, K.P.; Dubey, R.N. Effect of cross walls on the interaction curves of the unreinforced masonry walls. *Earthq. Eng. Struct. Dyn.* **2023**, *52*, 4518–4545. [CrossRef]
76. Russel, A.P.; Ingham, J. *The Influence of Flanges on the In-Plane Seismic Performance of URM Walls in New Zealand Buildings*; New Zealand Society of Earthquake Engineering: Wellington, New Zealand, 2010.
77. van der Meer, L.J.; Martens, D.R.W.; Vermeltfoort, A.T. UPT rectangular and flanged shear walls of high-strength CASIEL-TLM masonry: Experimental and numerical push-over analysis. *Eng. Struct.* **2013**, *49*, 628–642. [CrossRef]
78. Russell, A.P.; Elwood, K.J.; Ingham, J.M. Lateral Force–Displacement Response of Unreinforced Masonry Walls with Flanges. *J. Struct. Eng.* **2014**, *140*, 04013087. [CrossRef]
79. Vélez, L.F.R.; Magenes, G.; Griffith, M.C. Dry Stone Masonry Walls in Bending—Part I: Static Tests. *Int. J. Archit. Herit.* **2014**, *8*, 1–28. [CrossRef]
80. Khanmohammadi, M.; Behnam, H.; Marefat, M.S. Seismic Behavior Prediction of Flanged Unreinforced Masonry (FURM) Walls. *J. Earthq. Eng.* **2014**, *18*, 759–784. [CrossRef]
81. Bui, T.T.; Limam, A.; Sarhosis, V.; Hjiaj, M. Discrete element modelling of the in-plane and out-of-plane behaviour of dry-joint masonry wall constructions. *Eng. Struct.* **2017**, *136*, 277–294. [CrossRef]
82. Sajid, H.U.; Ashraf, M.; Ali, Q.; Sajid, S.H. Effects of vertical stresses and flanges on seismic behavior of unreinforced brick masonry. *Eng. Struct.* **2018**, *155*, 394–409. [CrossRef]
83. Mordant, C.; Dietz, M.; Degée, H. Experimental tests on the seismic behaviour of unreinforced load-bearing masonry structures. In Proceedings of the Earthquake Engineering and Structural Dynamics 2013 (VEESD 2013), Vienna, Austria, 28–30 August 2013.
84. Mordant, C.; Dietz, M.; Taylor, C.; Degée, H. Seismic Behaviour of Thin-Bed Layered Unreinforced Clay Masonry Frames with T- or L-Shaped Piers. In *Experimental Research in Earthquake Engineering*; Springer: Cham, Germany, 2015. [CrossRef]
85. Mordant, C.; Taylor, C.; Dietz, M.; Vasseur, L.; Degée, H. Shaking table tests on unreinforced load bearing masonry structures. In Proceedings of the 9th International Masonry Conference (IMS), Guimarães, Portugal, 7–9 July 2014.
86. Haach, V.G.; Ramalho, M.A.; Corrêa, M.R.S. Parametrical study of unreinforced flanged masonry walls subjected to horizontal loading through numerical modeling. *Eng. Struct.* **2013**, *56*, 207–217. [CrossRef]
87. Alamdari, B.E. Evaluation of the Effects of the Flanges on Strength and Failure Modes of Masonry Walls. Master's Thesis, Sharif University of Technology, Tehran, Iran, 2020.
88. Alamdari, B.E.; Ghezelbash, A.; Dolatshahi, K.M. Evaluation of the effects of the flanges on strength and failure modes of masonry walls. In Proceedings of the 12th International Congress on Civil Engineering, Mashhad, Iran, 25–27 October 2024.

89. Patel, K.P.; Dubey, R.N. Effect of flanges on the in-plane behavior of the masonry walls. *Eng. Struct.* **2022**, *273*, 115059. [CrossRef]
90. Yao, N.N.; Zhang, W.F.; Wei, J.W. The Flange Effect of Brick Masonry Wall Subjected to Seismic Effect. *Appl. Mech. Mater.* **2012**, *193–194*, 1444–1448. [CrossRef]
91. Mortezaei, A.; Kalantari, M. Seismic evaluation and FRP strengthening of unreinforced flanged masonry walls. *Asian J. Civ. Eng. (BHRC)* **2015**, *16*, 1155–1173.
92. Ghamari, M.; Karimi, M.S.; Lourenço, P.B.; Sousa, H.S. Flanges' Impact on Persian Historical Masonry Walls: Modeling Safety Factors. *Int. J. Eng.* **2024**, *37*, 1136–1145. [CrossRef]
93. Zeng, B. Computational Modeling and Multi-Fidelity Uncertainty Analysis for Masonry Walls Under In-Plane and/or Out-of-Plane Loading: Development and Applications. Ph.D. Thesis, University of Alberta, Edmonton, Canada, 2024.
94. Pradhan, B.; Zizzo, M.; Sarhosis, V.; Cavaleri, L. Out-of-plane behaviour of unreinforced masonry infill walls: Review of the experimental studies and analysis of the influencing parameters. *Structures* **2021**, *33*, 4387–4406. [CrossRef]
95. Zhang, P.; Chen, L.; Wei, T.; Huang, P.; Wang, H.; Chen, X. Multi-Hazard Assessment of Masonry Buildings: A State-of-the-Art Review. *Buildings* **2024**, *14*, 3711. [CrossRef]
96. Chourasia, A.; Bhattacharyya, S.K.; Bhandari, N.M.; Bhargava, P. Seismic Performance of Different Masonry Buildings: Full-Scale Experimental Study. *J. Perform. Constr. Facil.* **2016**, *30*, 04016006. [CrossRef]
97. Robazza, B.R.; Brzev, S.; Yang, T.Y.; Elwood, K.J.; Anderson, D.L.; Mcewen, B. Out-of-Plane Behavior of Slender Reinforced Masonry Shear Walls under In-Plane Loading: Experimental Investigation. *J. Struct. Eng.* **2018**, *144*, 04018008. [CrossRef]
98. Hosseinzadeh, S.; Galal, K. Seismic Fragility Assessment and Resilience of Reinforced Masonry Flanged Wall Systems. *J. Perform. Constr. Facil.* **2020**, *34*, 04019109. [CrossRef]
99. de Medeiros, G.F.; Mohamad, G.; Eduardo Kosteski, L.; Quispe Rodriguez, R.; Simonetti Milani, A. Strength capacity of hollow clay blocks structural masonry—Flange, Chases, and slenderness effects. *Eng. Struct.* **2022**, *272*, 114943. [CrossRef]
100. Cheng, J.; Shing, P.B. A beam-column element for modeling nonlinear flexural and shear behaviors of reinforced masonry walls. *Earthq. Eng. Struct. Dyn.* **2022**, *51*, 1918–1942. [CrossRef]
101. Kallioras, S.; Graziotti, F. Experimental insights into the seismic behaviour of flanged URM walls. *Eng. Struct.* **2025**, *322*, 119057. [CrossRef]
102. Sharma, S.; Tomassetti, U.; Grottoli, L.; Graziotti, F. Two-way bending experimental response of URM walls subjected to combined horizontal and vertical seismic excitation. *Eng. Struct.* **2020**, *219*, 110537. [CrossRef]
103. Chang, L.; Rots, J.G.; Esposito, R. Influence of aspect ratio and pre-compression on force capacity of unreinforced masonry walls in out-of-plane two-way bending. *Eng. Struct.* **2021**, *249*, 113350. [CrossRef]
104. Chang, L.; Rots, J.G.; Esposito, R. Influence of openings on two-way bending capacity of unreinforced masonry walls. *J. Build. Eng.* **2022**, *51*, 104222. [CrossRef]
105. Li, Y.; Zeng, B. Modeling of masonry structures using a new 3D cohesive interface material model considering dilatancy softening. *Eng. Struct.* **2023**, *277*, 115466. [CrossRef]
106. Acconcia, E.; Buonocunto, V.; Parisi, F. Numerical investigation on the flange effect in unreinforced masonry wall system through nonlinear finite element modelling. In Proceedings of the 9th International Conference on Computational Methods in Structural Dynamics and Earthquake Engineering (COMPDYN), Athens, Greece, 12–14 June 2023.
107. Vafa, N. Seismic Retrofitting of Masonry Structures with Post-Installed Systems. Ph.D. Thesis, Politecnico di Milano, Milan, Italy, 2023.
108. Scamardo, M.; Cattaneo, S.; Crespi, P.; Vafa, N. Cyclic behavior of C-shaped masonry wall retrofitted with twisted bars or bonded rebars. *Constr. Build. Mater.* **2024**, *443*, 137703. [CrossRef]
109. Cattaneo, S.; Crespi, P.; Scamardo, M.; Vafa, N. Cyclic behavior of masonry walls retrofitted with post-installed twisted bars or bonded rebars. *Constr. Build. Mater.* **2023**, *409*, 134026. [CrossRef]
110. Cattaneo, S.; Genesio, G.; Piccinin, R. Seismic Design of Anchorages Using Post-installed Reinforcing Bars. In *Building for the Future: Durable, Sustainable, Resilient*; Springer: Cham, Germany, 2023. [CrossRef]
111. Chang, L. Parametric Numerical Study on Two-Way Bending Capacity of Unreinforced Masonry Walls. Ph.D. Thesis, Delft University of Technology, Delft, The Netherlands, 2022. [CrossRef]
112. Russell, A.P. Characterisation and Seismic Assessment of Unreinforced Masonry Buildings. Ph.D. Thesis, The University of Auckland, Auckland, New Zealand, 2010.
113. Ahmed, H.A.; Shahzada, K. Numerical modeling of confined brick masonry structures with parametric analysis and energy absorption calculation. *Int. J. Prot. Struct.* **2021**, *12*, 129–152. [CrossRef]
114. Lourenço, P.B.; Rots, J.G.; Blaauwendraad, J. Continuum Model for Masonry: Parameter Estimation and Validation. *J. Struct. Eng.* **1998**, *124*, 642–652. [CrossRef]
115. D'Altri, A.M.; Sarhosis, V.; Milani, G.; Rots, J.; Cattari, S.; Lagomarsino, S.; Sacco, E.; Tralli, A.; Castellazzi, G.; de Miranda, S. Modeling Strategies for the Computational Analysis of Unreinforced Masonry Structures: Review and Classification. *Arch. Comput. Methods Eng.* **2020**, *27*, 1153–1185. [CrossRef]

116. Sudhakar, M.; Raj, M.P.; Natarajan, C. *Advances in Structural Engineering*; Springer: New Delhi, India, 2015. [CrossRef]
117. Drysdale, R.G.; Hamid, A.A.; Baker, L.R. *Masonry Structures: Behavior and Design*; Prentice Hall: Upper Saddle River, NJ, USA, 1999.
118. Korswagen, P.A.; Longo, M.; Prosperi, A.; Rots, J.G.; Terwel, K.C. Modelling of Damage in Historical Masonry Façades Subjected to a Combination of Ground Settlement and Vibrations. In *Structural Analysis of Historical Constructions*; Springer: Cham, Germany, 2024. [CrossRef]
119. Khanmohammadi, M.; Behnam, H. A Review on Innovative methods in Silmulation of IO-OP Interaction of Brick Walls. In Proceedings of the 5th Congress of Civil Engineering, Mashhad, Iran, 4 May 2011.
120. Kesavan, P.; Menon, A. A macro-element with bidirectional interaction for seismic analysis of unreinforced masonry walls. *Earthq. Eng. Struct. Dyn.* **2023**, *52*, 1740–1761. [CrossRef]
121. Salvatori, C.; Guerrini, G.; Galasco, A.; Penna, A. A Macroelement Formulation for Modeling Strengthened and Reinforced Masonry Elements. In Proceedings of the 18th International Brick and Block Masonry Conference, Cham, Germany, 21–24 July 2024. [CrossRef]
122. Kadysiewski, S.; Mosalam, K.M. Modelling of Unreinforced Masonry Infill Walls Considering In-Plane and Out-of-Plane Interaction. In Proceedings of the 11th Canadian Masonry Symposium, Toronto, ON, Canada, 31 May–3 June 2009.
123. Agnihotri, P.; Singhal, V.; Rai, D.C. Effect of in-plane damage on out-of-plane strength of unreinforced masonry walls. *Eng. Struct.* **2013**, *57*, 1–11. [CrossRef]
124. *ASCE 41-17*; Seismic Evaluation and Retrofit of Existing Buildings. American Society of Civil Engineers (ASCE): Reston, VA, USA, 2017.
125. Magenes, G.; Calvi, G.M. In-plane seismic response of brick masonry walls. *Earthq. Eng. Struct. Dyn.* **1997**, *26*, 1091–1112. [CrossRef]
126. Lourenço, P.B.; Rots, J.G. Multisurface Interface Model for Analysis of Masonry Structures. *J. Eng. Mech.* **1997**, *123*, 660–668. [CrossRef]
127. van Zijl, G.P.A.G. *Computational Modelling of Masonry Creep and Shrinkage*; Delft University of Technology: Delft, The Netherlands, 2000.
128. Macorini, L.; Izzuddin, B.A. A non-linear interface element for 3D mesoscale analysis of brick-masonry structures. *Int. J. Numer. Methods Eng.* **2011**, *85*, 1584–1608. [CrossRef]
129. Aref, A.J.; Dolatshahi, K.M. A three-dimensional cyclic meso-scale numerical procedure for simulation of unreinforced masonry structures. *Comput. Struct.* **2013**, *120*, 9–23. [CrossRef]
130. D'Altri, A.M.; de Miranda, S.; Castellazzi, G.; Sarhosis, V. A 3D detailed micro-model for the in-plane and out-of-plane numerical analysis of masonry panels. *Comput. Struct.* **2018**, *206*, 18–30. [CrossRef]
131. D'Altri, A.M. Advances in Computational Analysis of Masonry Structures. Ph.D. Thesis, University of Bologna, Bologna, Italy, 2019.
132. Zeng, B.; Li, Y.; Noguez, C.C. Modeling and parameter importance investigation for simulating in-plane and out-of-plane behaviors of un-reinforced masonry walls. *Eng. Struct.* **2021**, *248*, 113233. [CrossRef]
133. Nie, Y.; Sheikh, A.; Visintin, P.; Griffith, M. A robust computational strategy for failure prediction of masonry structures using an improved multi-surface damage-plastic based interface model. *Int. J. Numer. Methods Eng.* **2023**, *124*, 2498–2528. [CrossRef]
134. Nie, Y.; Sheikh, A.; Griffith, M.; Visintin, P. A damage-plasticity based interface model for simulating in-plane/out-of-plane response of masonry structural panels. *Comput. Struct.* **2022**, *260*, 106721. [CrossRef]
135. Bui, T.T.; Limam, A.; Sarhosis, V. Failure analysis of masonry wall panels subjected to in-plane and out-of-plane loading using the discrete element method. *Eur. J. Environ. Civ. Eng.* **2021**, *25*, 876–892. [CrossRef]
136. Baraldi, D.; Cecchi, A. A full 3D rigid block model for the collapse behaviour of masonry walls. *Eur. J. Mech.-A/Solids* **2017**, *64*, 11–28. [CrossRef]
137. Milani, G. 3D upper bound limit analysis of multi-leaf masonry walls. *Int. J. Mech. Sci.* **2008**, *50*, 817–836. [CrossRef]
138. Tiberti, S.; Milani, G. 3D homogenized limit analysis of non-periodic multi-leaf masonry walls. *Comput. Struct.* **2020**, *234*, 106253. [CrossRef]
139. Oktiovan, Y.P.; Messali, F.; Pulatsu, B.; Lemos, J.V.; Rots, J.G. A contact-based constitutive model for the numerical analysis of masonry structures using the distinct element method. *Comput. Struct.* **2024**, *303*, 107499. [CrossRef]
140. Khattak, N.; Derakhshan, H.; Thambiratnam, D.P.; Malomo, D.; Perera, N.J. Modelling the in-plane/out-of-plane interaction of brick and stone masonry structures using Applied Element Method. *J. Build. Eng.* **2023**, *76*, 107175. [CrossRef]
141. Smoljanović, H.; Živaljić, N.; Nikolić, Ž.; Munjiza, A. Numerical analysis of 3D dry-stone masonry structures by combined finite-discrete element method. *Int. J. Solids Struct.* **2018**, *136–137*, 150–167. [CrossRef]
142. Pantò, B.; Cannizzaro, F.; Caliò, I.; Lourenço, P.B. Numerical and Experimental Validation of a 3D Macro-Model for the In-Plane and Out-Of-Plane Behavior of Unreinforced Masonry Walls. *Int. J. Archit. Herit.* **2017**, *11*, 946–964.

143. Caliò, I.; Marletta, M.; Pantò, B. A new discrete element model for the evaluation of the seismic behaviour of unreinforced masonry buildings. *Eng. Struct.* **2012**, *40*, 327–338. [CrossRef]
144. Minga, E.; Macorini, L.; Izzuddin, B.A.; Caliò, I. 3D macroelement approach for nonlinear FE analysis of URM components subjected to in-plane and out-of-plane cyclic loading. *Eng. Struct.* **2020**, *220*, 110951. [CrossRef]
145. Lourenço, P.B.; De Borst, R.; Rots, J.G. A plane stress softening plasticity model for orthotropic materials. *Int. J. Numer. Methods Eng.* **1997**, *40*, 4033–4057. [CrossRef]
146. Lourenço, P.B. Anisotropic Softening Model for Masonry Plates and Shells. *J. Struct. Eng.* **2000**, *126*, 1008–1016. [CrossRef]
147. Noor-E-Khuda, S.; Dhanasekar, M.; Thambiratnam, D.P. An explicit finite element modelling method for masonry walls under out-of-plane loading. *Eng. Struct.* **2016**, *113*, 103–120. [CrossRef]
148. Noor-E-Khuda, S. An Explicit Finite-Element Modeling Method for Masonry Walls Using Continuum Shell Element. *J. Archit. Eng.* **2021**, *27*, 04021040. [CrossRef]
149. Vecchio, F.J.; Collins, M.P. The modified compression field theory for reinforced concrete elements subjected to shear. *ACI J.* **1986**, *83*, 219–231.
150. Rots, J.G.; Messali, F.; Esposito, R.; Jafari, S.; Mariani, V. Thematic Keynote Computational modelling of masonry with a view to Groningen induced seismicity. In Proceedings of the 10th International Conference on Structural Analysis of Historical Constructions, Leuven, Belgium, 13–15 September 2016.